UNIVERSIDADE FEDERAL DE SÃO CARLOS
CENTRO DE CIÊNCIAS EXATAS E DE TECNOLOGIA
DEPARTAMENTO DE QUÍMICA
PROGRAMA DE PÓS-GRADUAÇÃO EM QUÍMICA

PHOTOCATALYTIC CONTROLLED OXIDATION REACTION OF METHANE

Jean Castro da Cruz*

Thesis presented as part of the requirements to obtain the title of DOCTOR IN SCIENCES, concentration area: PHYSICAL-CHEMISTRY.

Advisor: Caue Ribeiro de Oliveira
Co-advisor: Elaine Cristina Paris

*** bolsista CAPES/PROEX**

São Carlos - SP
2023

UNIVERSIDADE FEDERAL DE SÃO CARLOS

Centro de Ciências Exatas e de Tecnologia
Programa de Pós-Graduação em Química

Folha de Aprovação

Defesa de Tese de Doutorado do candidato Jean Castro da Cruz, realizada em 28/06/2023.

Comissão Julgadora:

Prof. Dr. Cauê Ribeiro de Oliveira (EMBRAPA)

Prof. Dr. Elton Fabiano Sitta (UFSCar)

Prof. Dr. Ivo Freitas Teixeira (UFSCar)

Profa. Dra. Renata Pereira Lopes Moreira (UFV)

Profa. Dra. Ana Paula de Carvalho Teixeira (UFMG)

O Relatório de Defesa assinado pelos membros da Comissão Julgadora encontra-se arquivado junto ao Programa dePós-Graduação em Química.

DEDICATÓRIA

Dedico este trabalho ao meu afilhado e sobrinho, Joaquim Bento, para que possa servir como um exemplo concreto de que você é capaz de conquistar tudo que desejar. Que você sempre siga seus sonhos com coragem e determinação, sabendo que não há limites para suas conquistas.

AGRADECIMENTOS

A Deus por ter me ajudado a superar os meus desafios ao longo da minha trajetória.

Ao Dr. Caue Ribeiro, por sua orientação que me inspiraram e me encorajaram a enfrentar os desafios e a buscar a excelência em minha pesquisa.

Aos doutores Elton Sitta, Ivo F. Teixeira, Renata P. L. Moreira e Ana Paula de Carvalho Teixeira pelas contribuições durante as avaliações do meu doutorado.

Ao programa de Pós-Graduação em Química da Universidade Federal de São Carlos (PPGQ-UFSCar), pela oportunidade de realizar o doutorado. À CAPES que concedeu a bolsa de estudos para o desenvolvimento desse trabalho.

À Embrapa Instrumentação pela estrutura fornecida para a realização deste trabalho. Em especial ao pessoal de suporte à pesquisa, Joana e Viviane.

A todos do grupo de pesquisa do qual faço parte, em especial ao Eduardo, Gustavo, Stella, e Amanda pelo apoio constante e momentos de café que tornaram o ambiente agradável.

Aos doutores Juliana e Gelson por todo o incentivo, discussões valiosas, parceria e principalmente pela amizade. Em especial, a Dra. Jéssica pelo apoio incondicional, momentos valiosos de aprendizagem e por ter acreditado nos meus insights. Sua paixão pela ciência, sua disposição em compartilhar seu conhecimento, e acima de tudo sua amizade foram fundamentais para minha jornada de crescimento pessoal e profissional.

Ao Laboratório de Caracterização Estrutural LCE/DEMa pelas análises de HRTEM. Ao Instituto de Física da Universidade de São Paulo (IFSC/USP) pela análise de XPS. Em especial ao Dr. Otaciro pelo auxílio na análise de EPR.

A minha família de São Carlos, Joyce, Daniela, Natália e Giovana, pessoas incríveis que tive a oportunidade de compartilhar o dia a dia e evoluir como ser humano. Ao Henrique por todos os conselhos e momentos de alegria que foram fundamentais para que as últimas etapas do meu doutorado fossem mais agradáveis.

Aos meus amigos de Araraquara, Luiz, Nando, Gustavo, Minghini, e em especial, à Bianca e ao Malara, pelos momentos inesquecíveis e inspiradores.

Em especial à minha família, Almir, Roseli, Leonardo, Ana Carolina e Joaquim por todo o amor incondicional, paciência, por entenderem os meus momentos de ausência e sempre me incentivarem a realizar os meus sonhos. Sem vocês essa conquista não seria possível

TABLE LIST

FIGURE LIST

RESUMO

REAÇÃO DE OXIDAÇÃO FOTOCATALÍTICA CONTROLADA DO METANO. A oxidação parcial do CH_4 em produtos químicos de valor agregado por meios solares tem sido discutida como alternativa para a redução de emissões, um tópico fundamental para a produção sustentável e com menor emissão de gases causadores do aquecimento global no futuro. Até o momento, vários fotocatalisadores semicondutores foram desenvolvidos. Entretanto, a compreensão dos principais fatores que influenciam as atividades dos fotocatalisadores na oxidação controlada do metano em metanol ainda é um problema, especialmente devido à superoxidação do metano em CO_2. Assim, propomos que o semicondutor deve ter uma banda de valência (VB) favorável à produção de radicais hidroxila (•OH) e uma banda de condução (CB) não vantajosa para o radical superóxido ($O_2^{\bullet-}$). Além disso, a concentração dos radicais hidroxila é fundamental e deve ser ajustada para oxidar seletivamente o metano. O O_2 também é o principal oxidante para o controle do processo, uma vez que o O_2 pode capturar os radicais metil (•CH_3) que reagem posteriormente com •OH para formar metanol. Nossos resultados mostraram que as posições de banda necessárias para os fotocatalisadores (por exemplo, Bi_2O_3) parecem corretas para obter quantidades significativas de produtos químicos desejáveis, tendo como principais produtos o metanol (3700 μmol g^{-1} h^{-1}) e o ácido acético (2036 μmol g^{-1} h^{-1}) a partir do CH_4 puro em temperatura ambiente e pressão atmosférica. Além disso, hidrocarbonetos mais longos (por exemplo, etanol e acetona) podem ser produzidos dependendo da condição reacional. Os experimentos de EPR comprovaram a formação de •CH_3 e •OH, e também foi realizado um experimento isotópico com $^{13}CH_4$ como reagente, confirmando que o CH_3OH é proveniente da foto-oxidação do CH_4. Foi investigada outra rota sustentável para controlar a oxidação de CH_4 impulsionada por intermediários de cloro em solução, usando semicondutores a base de bismuto excitados em luz visível. O BiOCl, um material em camadas de perovskita, apresentou um desempenho fotocatalítico promissor para a conversão de metano a metanol (1300 μmol g^{-1}), ácido acético (435 μmol g^{-1}), e etanol (57 μmol g^{-1}) sem a adição de radicais externos para controlar a reação. Nossas descobertas são significativas para um novo nível de compreensão da eficiente foto-oxidação parcial do metano, o que abre um caminho para o controle de reações competitivas por meio de posições de banda apropriadas em fotocatalisadores para maior seletividade e para evitar sua superoxidação em CO_2.

ABSTRACT

PHOTOCATALYTIC CONTROLLED OXIDATION REACTION OF METHANE. The CH_4 partial oxidation into value-added chemicals by solar means has been discussed as alternative for emission abatement, a fundamental topic for sustainable production with lower global warming gas emissions in future. So far, various semiconductor photocatalysts have been developed. However, the understanding of the main factors influencing photocatalysts' activities on controlled oxidation of methane to methanol is still an issue, especially due to methane overoxidation to CO_2. Thus, we propose that the semiconductor must have a valence band (VB) favorable to produce hydroxyl radicals (•OH) and a conduction band (CB) not advantageous to superoxide radical ($O_2^{\bullet-}$). Furthermore, the concentration of the hydroxyl radicals is fundamental and should be fine-tuned for selectively oxidize methane. O_2 also is the key oxidant for process control, since O_2 may scavenging methyl radicals (•CH_3) that further react with •OH to form methanol. Our results showed that the required band edge positions for photocatalysts (e.g., Bi_2O_3) seems correct to obtain significant amounts of desirable chemical products, taking as main products methanol (3700 μmol g^{-1}) and acetic acid acetic acid (~2036 μmol g^{-1} h^{-1}) from pure CH_4 at room temperature and atmospheric pressure. Moreover, longer hydrocarbons (e.g., ethanol and acetone) could be produced depending on the reaction condition. ESR experiments proved the formation of •CH_3 and •OH, and isotope labeling experiment with $^{13}CH_4$ as the reactant also was conducted, confirming that CH_3OH comes from CH_4 photooxidation. Another sustainable route to control the CH_4 oxidation driven by chloride intermediates in solution using Bismuth-based semiconductors excited in visible light was investigated. BiOCl, a perovskite layered material, exhibited promising photocatalytic performance for methane conversion to methanol (1300 μmol g^{-1}), acetic acid (435 μmol g^{-1}), and ethanol (57 μmol g^{-1}) without foreign radicals to control the reaction. Our findings are significant to new level of understanding in methane's efficient partial photooxidation, which opens a way to control competitive reactions by appropriate band edge positions in photocatalysts to greater selectivity and avoid its overoxidation to CO_2.

SUMMARY

1. CHAPTER I: INTRODUCTION

1.1. Background

The combustion of fossil fuels and the subsequent emission of greenhouse gases increasingly harm the climate. Methane is a greenhouse gas with a global warming potential (GWP) that is 25 times higher than carbon dioxide. It can be found as the primary component of natural gas and biogas, reaching c.a. 75-90% of its composition. Several world reserves of shale gas, fire ice, and coalbed constitute an important primary source for global energy generation. However, the transportation of gas over long distances, from the natural reserve to the distribution centers, is inconvenient, mainly due to possible gas leakage. Thus, some conditions require methane to be burned instead of released directly into the atmosphere due to its high GWP. Consequently, every day, approximately 150 billion cubic meters of natural gas are burned as waste, resulting in an annual energy loss of 30 EJ. As an alternative to fuel application, CH_4 can also be a feedstock to produce chemicals of commercial interest. The industrial transformation of CH_4 into syngas (Eq. 1.1) is performed at high temperatures (400-800 K) and pressures (20-40 bar). Methane conversion on-site into liquid chemicals is further desirable, and methanol (Eq. 1.2) is the preferred product since CH_3OH and CH_4 possess similar calorific power. Additionally, methanol is a storable and transportable liquid fuel at ambient conditions, serving as chemical feedstock for even higher-value products such as formaldehyde, formic acid, acetic acid, and methyl *t*-butyl ether [1–5].

$$CH_{4(g)} + H_2O_{(g)} \xrightarrow{Ni} CO_{(g)} + H_{2(g)} \quad (1.1)$$

$$CO_{(g)} + 2H_{2(g)} \xrightarrow{Cu/ZnO/Al_2O_3} CH_3OH_{(g)} \quad (1.2)$$

The thermodynamic stability of the C-H bonds (434 kJ mol^{-1}), insignificant electron affinity, and poor polarizability (2.84 x 10^{-40} C^2 m^2 J^{-1}) of the CH_4 molecule are the main drawbacks for the conventional methane reform since the described shortcomings are primarily responsible for the high energy consumption, cost, and CO_2 emissions of the process. Additionally, the use of precious metal catalysts is required, catalyst deactivation is observed, and extremely low conversion efficiencies are obtained. Therefore, direct conversion of CH_4 into CH_3OH under mild conditions stands out to

reduce capital expenses and address environmental issues. Photo(electro)catalysis (PEC) can utilize sunlight and power source instead of high temperature and pressure to perform the non-spontaneous reaction. Even though the extremely low solubility of methane in water (< 22.7 mg L^{-1}), CH_4 dissolution in electrolytes is still appealing because the system often is easier to manipulate and to be scaled up. Nonetheless, very few studies in the literature regarding PEC systems for controlled CH_4 reform demonstrate the uniqueness of the recent research field. From this perspective, ZnO, WO_3, and TiO_2 have been evaluated as photo(electro)catalysts due to their well-known photoactivities while having adequate conductivity for electrochemical proposals.

Li *et al*. [6] used TiO_2 as a photoanode to produce CO from CH_4. The photogenerated charges first become self-trapped on Ti, reducing the metal to become Ti^{3+} and generating $^{-}$•O–Ti^{3+}. The presence of Ti^{3+} promotes the creation of a Ti^{3+}-C bond which results in the selective synthesis of CO. Alternatively, Ti^{4+} sites favor the carbonate production, leading to a total oxidation of CH_4, Fig. 1.1 Kadosh *et al.* [7] detected CO_2 as the main product and O_2, CO, C_2H_6, and HCOOH as byproducts of CH_4 oxidation using TiO_2 as photoanode in 0.05 M H_2SO_4 and at 0.3 V *vs.* RHE. Liu *et al.* [8] used pure $BiVO_4$ and obtained methanol at 0.5 V *vs.* RHE with a Faradaic efficiency of 16%. Liu *et al.* [9] performed the PEC oxidation of CH_4 into methanol over ZnO, reaching ca. 12% of Faradaic efficiency. Amano *et al*. [10] selected WO_3 to convert CH_4 into C_2H_6, CO_2, and H_2 at 1.2 V *vs.* SHE on a proton exchange membrane-containing membrane electrode assembly (MEA/PEM). The MEA/PEM-based PEC cell promoted an efficient product separation in a flow system, obtaining an incident photon-to-current conversion efficiency (IPCE) of 11%, a Faradaic efficiency for CO_2 of 75%, a CH_4 conversion of 0.1%, and a C_2H_6 selectivity of 54%. Surprisingly, Ma *et al.* [11] also evaluated WO_3 as the photoanode but could produce a higher carbon-chair of ethylene glycol at a rate of 0.47 μmol cm^{-2} h^{-1} and 66% selectivity at 1.3 V *vs.* RHE. The PEC oxidation was performed at 0.1 M Na_2SO_4 with pH adjustment to 2 with sulfuric acid to inhibit the competing oxygen reaction evolution. The system showed high stability for 12 h.

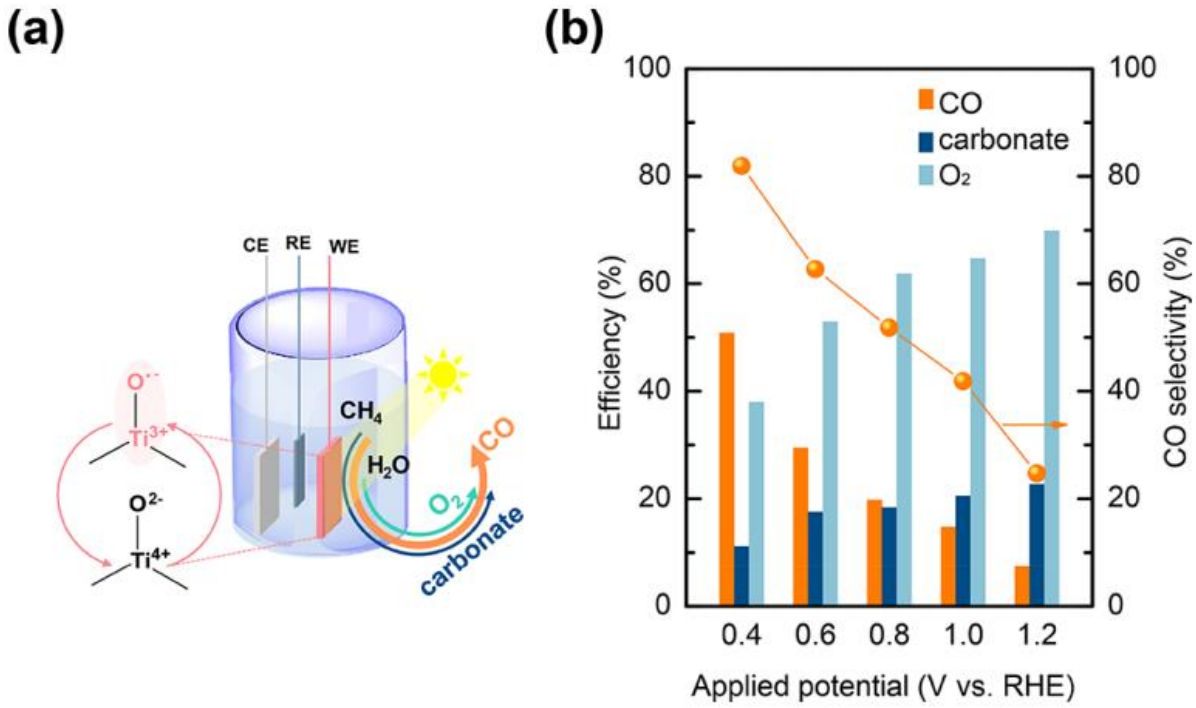

FIGURE 1.1 - (a) Schematic mechanism of TiO_2 for PEC CH_4 oxidation to CO. (b) CH_4 photoelectrochemical oxidation at different applied potentials. Reproduced with permission. [6]

As one can see, challenges remain for the PEC approach of CH_4 reform to methanol, such as the enhancement of selectivity and the prevention of overoxidation to the more kinetically and thermodynamically favorable CO_2. The hydroxyl radicals (•OH) are the predominant oxidative species to activate the C–H bonds of methane. Firstly, •OH abstracts a hydrogen atom to generate methyl radicals (•CH_3) (Eq. 1.3) which finally react with •OH to form methanol (Eq. 1.4). The concentration of the hydroxyl radical is crucial for controlling the rate of methane conversion and the CH_3OH selectivity. The lower •OH concentration leads to the lower formation of methyl radicals, while the higher •OH concentration leads to higher overoxidation of CH_4 and byproducts to form CO_2. Thus, an ideal concentration of hydroxyl radicals and moderate oxidation conditions are required to oxidize CH_4 into CH_3OH selectively [2,12].

$$CH_{4(aq)} + \bullet OH_{(aq)} \rightarrow \bullet CH_{3(aq)} + H_2O_{(l)} \quad (1.3)$$

$$\bullet CH_{3(aq)} + \bullet OH_{(aq)} \rightarrow CH_3OH_{(aq)} \quad (1.4)$$

Recent advances have used different sacrificial reagents to control the extent of the oxidation process. Nitrite ions (Eq. 1.5) and hydrogen peroxide (Eq. 1.6) can be used to induce or inhibit the •OH consumption. Nonetheless, the substantial costs associated with adding these chemicals into the system make the process on a large scale uneconomical. Another practical barrier is that CH_4 conversion often fails to maintain high conversion yield and selectivity since the overoxidation of methanol is hard to inhibit. Recent mechanism evaluations have pointed out that $O_2•^-$ are the key species for the uncontrolled oxidation of methane since the generated methyl radicals may be attacked by superoxide radicals, leading to full oxidation to produce CO_2. In this regard, for an efficient methane partial oxidation, it was demonstrated elsewhere that the semiconductor must present an appropriate band edge position to have a valence band favorable to hydroxyl radicals and a conduction band not advantageous to superoxide radicals [1,2,13,14].

$$NO_2^-{}_{(aq)} + •OH_{(aq)} \rightarrow NO_2•_{(aq)} + OH^-{}_{(aq)} \quad (1.5)$$

$$H_2O_{2(aq)} \rightarrow •OH_{(aq)} + OH^-{}_{(aq)} \quad (1.6)$$

Further studies also have demonstrated that molecular oxygen is the critical component for methane transformation. Experiments with isotope oxygen proved that there is another radical mechanism route for methanol production. In the disclosed scheme, the dissolved O_2 promotes oxygen incorporation through the generation of methyl hydroperoxide radicals (Eq. 1.7), making O_2 act as $•CH_3$ scavenger, thus, improving the methanol production that can come either from the coupling of $CH_3OO•$ and •OH (Eq. 1.8) or from the reduction process of the CH_3OOH intermediate through a photoreduction process (Eq. 1.9-1.10). Density functional theory (DFT) calculations suggested that the energy barrier for CH_3OOH formation (0.52 eV) is lower than for the direct CH_3OH generation (0.72 eV), thus favoring the chemical route of the intermediate CH_3OOH. In excess of H_2O_2, a competitive reaction pathway to form O_2 can be induced (Eq. 1.11), and H_2O_2 can also impact the methane conversion by increasing the availability of O_2 in the medium reaction [12,15–17].

$$\bullet CH_{3(aq)} + O_{2(g)} \rightarrow CH_3OO\bullet_{(aq)} \quad (1.7)$$

$$CH_3OO\bullet_{(aq)} + \bullet OH_{(aq)} \rightarrow CH_3OH_{(aq)} + O_{2(aq)} \quad (1.8)$$

$$CH_3OO\bullet_{(aq)} + H^+_{(aq)} + e^- \rightarrow CH_3OOH_{(aq)} \quad (1.9)$$

$$CH_3OOH_{(aq)} + 2e^- + 2H^+_{(aq)} \rightarrow CH_3OH_{(aq)} + H_2O_{(l)} \quad (1.10)$$

$$H_2O_{2(aq)} \rightarrow H_2O_{(l)} + 1/2\, O_{2(g)} \quad (1.11)$$

Oxygen species seem to be the bottleneck for methane conversion since oxygen vacancies play a different role in the efficiency of this oxidation reaction. Removing an oxygen atom with six valence electrons leaves two electrons behind in the semiconductor surface. Then, through the hydrogen atom, methane can adsorb onto the surface, and fragments of the methyl radical can effectively transfer an electron to the surface. Experiments point out that the C−H bond cleavage proceeds at these oxygen vacancies sites since they attract electrons and alter the bonding energy of adsorbates, consequently lowering the energy barrier. The oxygen vacancies affect the electronic distribution of the surface since the excess of electrons resultant of the lack of oxygen can be reallocated on nearby metal sites that may donate more electrons for the adsorbed CH_4 and activate the methane due to new defect levels appearing at the active Fermi level position. The generation of methyl radicals via oxygen vacancies was reported even without photo- or electro-activation. *Ab initio* DFT+*U* calculations of methane adsorption on iron oxide have shown that the bond angle of the CH_4 molecule indeed changed along the adsorption on oxygen vacancies, increasing from 109.50° to 114.83° and tilting slightly to the left. As methane dissociates, CH_3 moves to the oxygen vacancy site while H lasts at the metal top site, lowering barrier activation by 14.4 kJ mol^{-1} compared to that on the stoichiometric surface [12,18–20].

On the other hand, the oxygen vacancies create new band states between the conduction and valence bands, narrowing the bandgap. At the same time, the oxygen vacancies also act as photogenerated carrier traps, reducing the recombination, which is beneficial for the PEC activity. Another significant change includes the electron density around the oxygen vacancies that can react with metal sites in their neighborhood, promoting a metal redox cycle. Jin *et al.* [21] have discussed that after the oxygen vacancies are created, the remaining electrons reduce the nearby Zn^{2+} to Zn^+ sites to obtain a balance neutral of the charges. Furthermore, the other electron is trapped by

oxygen vacancy, transforming it into an active site for reacting with other molecules. In particular, it creates a new donor level below the conduction band. Yang *et al.* [22] also demonstrated that the presence of oxygen defects in the 2D WO_{3-x} nanosheet results in unpaired electrons in the lattice, reducing the W^{6+} to W^{5+} through the process represented by Eq. 12, where O^{2-} is the lattice oxygen, O is the oxygen removed, and OV is the oxygen vacancy.

$$2W^{6+} + O^{2-} \rightarrow 2W^{5+} + O + OV \quad (12)$$

Many works have used some strategies to induce the creation of oxygen vacancies. In this context, Zhang *et al.* [23] reported the use of cobalt ion doping to replace the W^{6+} atoms and, consequently, induce disorder formation in the lattice. After the W^{6+} substitution, the cobalt showed two oxidation states (i.e., Co^{3+} and Co^{2+}), and the presence of the lower Co valence was due to the excess vacancy, as described above. Zhao *et al.* [24] selected Cu ions to tune the oxygen vacancies concentration in TiO_2 nanosheets, resulting in significantly improved photocatalytic gas interaction. Surprisingly, besides facilitating photoinduced charge transport, the oxygen vacancies induce Jahn-Teller distortions. As shown in Fig. 1.2, introducing defects cause substantial compressive strain, which increases the electron density around the oxygen atoms, enhancing the gas adsorption and allowing a lower energy pathway to the product.

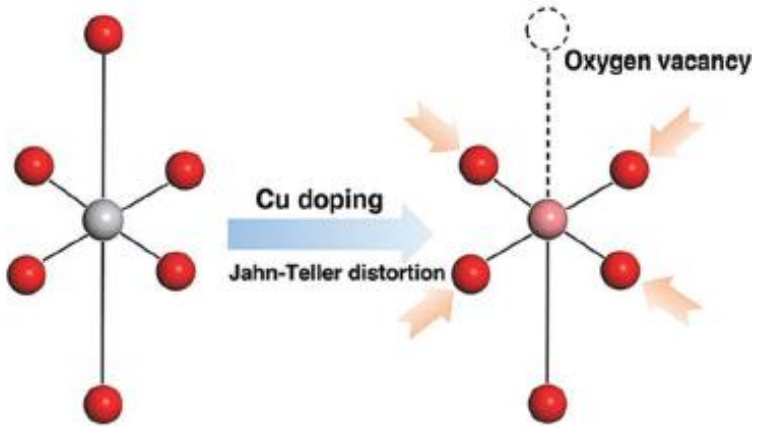

FIGURE 1.2 - Schematic illustration of a TiO_6 octahedron with defects induced by copper doping and oxygen vacancy. Reproduced with permission. [24]

In principle, the ability of the metal to change the oxidation states has been demonstrated as one of the critical properties for efficient thermal catalysis. This ability may also be vital for PEC methane reform since the metal site can be reduced in the initial stages to assist the proton extraction from methane. Then, the metal is re-oxidized to its initial state, desorbing the products formed and reconstituting the catalyst. Yu *et al.* [25] used *in-situ* FTIR spectroscopy to investigate the mechanism of methane oxidation to carbon monoxide on zinc distributed in tungstophosphoric acid/titania (Zn-HPW/TiO_2). The process (Fig. 1.3) follows the zinc oxidation-reduction pathway under irradiation and involves the production of methyl carbonate as a chemical intermediate. In parallel, oxygen plays an essential role in assisting the oxy-reduction cycle of the metal in regenerating the catalyst. Interestingly, oxygen vacancies may also offer an appealing alternative to avoid complete methane overoxidation to CO_2. In this case, the electrons on the oxygen vacancy change the potential of O 2p orbitals, shifting up the valence band maximum to a position that is no longer suitable for methanol oxidation [26].

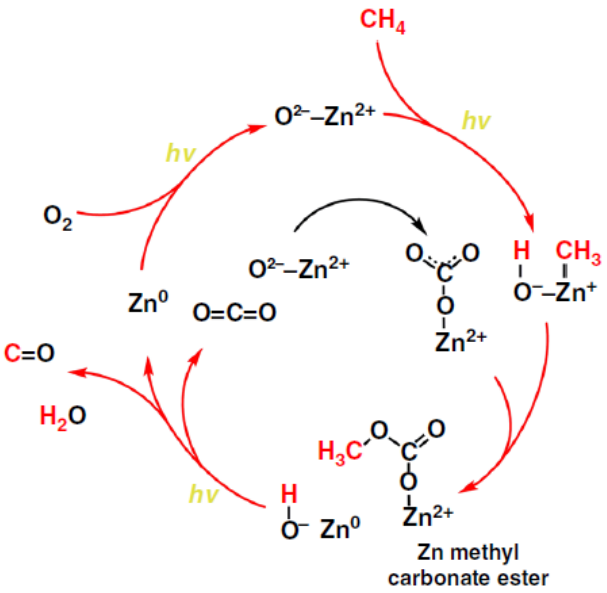

FIGURE 1.3 - Reaction pathway for the partial oxidation of CH_4 to CO over Zn-HPW/TiO_2. Reproduced with permission.[25]

Converting solar energy to chemical energy is the aim of PEC methane oxidation, but to facilitate future scalable production and useful application, the above-described features must be considered to improve the CH_4 conversion and associate the reaction with economic viability. For that, the production rate of the resultant product as well as other parameters, represented by Eqs. 1.13-1.17, usually are considered, where n_P

is the moles of the target produced chemical, n_T is the moles of total products, n_{TC} is the moles of carbon from the total products, n_{CH_4} is the moles of methane in the starting reaction, J is the current density, t is the reaction time, z is the number of electrons transferred in the target half-reaction of the product, F is the Faradaic constant (F = 96485 C mol^{-1}), $\sum E^0_{chemical}$ is the standard potential of the methane oxidation reaction, P is the power density of the incident light, N_{TE} is the number of transferred electrons, and N_{IP} is the number of incident photons [14,27].

Faradaic efficiency (η_{FE}):

$$\eta_{FE}\ (\%) = \left(\frac{z\ F\ n_P}{J\ t}\right) 100 \quad (1.13)$$

Solar-to-chemical conversion efficiency (STC):

$$STC\ (\%) = \left(\frac{\sum E^0_{chemical}\ J\ \eta_{FE}}{P}\right) 100 \quad (1.14)$$

Apparent quantum yield (AQY)

$$AQY\ (\%) = \left(\frac{N_{TE}}{N_{IP}}\right) 100 \quad (1.15)$$

Selectivity (SE):

$$SE\ (\%) = \left(\frac{n_P}{n_T}\right) 100 \quad (1.16)$$

CH_4 conversion (CC):

$$CC\ (\%) = \left(\frac{n_{TC}}{n_{CH_4}}\right) 100 \quad (1.17)$$

In conclusion, the photoelectrochemical conversion of methane to methanol is advantageous over the catalytic path because it uses mild oxidation conditions while maintaining high catalytic efficiency. This would result in significant capital investment and operating cost savings. At the same time, PEC CH_4 reform mitigates the concentration of harmful greenhouse gas in the atmosphere using the energy acquired from the external circuit and the solar spectrum, a freely available energy source, to activate the molecule bonds.

2. CHAPTER II: GOALS AND OVERVIEW

The main goal of this thesis was the understanding of the key factors influencing photocatalysts' activities on controlled oxidation of methane to methanol.

2.1. Specific goals:

- To investigate the appropriate band edge positions in photocatalysts to efficient CH_4 partial photooxidation to methanol;
- To investigate the efficiency of the bismuth oxide in the CH_4 conversion to methanol under visible-light and ambient conditions;
- To study the influence of molecular oxygen and oxidative radicals for selectively oxidize methane;
- To investigate how chloride ions act during photooxidation of methane using Bi-based semiconductors;
- To understand how a structural chloride could participate in the CH_4 conversion.

2.2. Summary of each chapter

This thesis focuses on studying a sustainable alternative for the controlled oxidation of methane to methanol, avoiding its complete oxidation to CO_2. In this scenario, photocatalytic systems for the production of oxidative radicals are reported to be suitable activators for the controlled oxidation of methane.

In the Chapter III, different ways of controlling the extent of the oxidation process were investigated, as well as the appropriate band edge position that the semiconductor should have a valence band (VB) favorable for producing hydroxyl radicals (•OH) and a conduction band (CB) that is not advantageous for superoxide radicals ($O_2^{\bullet -}$). Additionally, different sacrificial reagents and the influence of molecular oxygen on selectively oxidizing methane to methanol were studied.

After understanding the role of oxidative radicals and the presence of molecular oxygen for the selective oxidation of methane in methanol, an alternative route from the formation of chloromethane was proposed. Thus, the oxidation of methane in the presence of chloride ions in solution and within the crystal structure of the semiconductor were evaluated. The main results of this part are shown in Chapter IV.

3. CHAPTER III: Bismuth oxide activity for CH_4 photooxidation

The content of this chapter is an adaptation of the article entitled "**Selective CH_4 reform to methanol through partial oxidation over Bi_2O_3 at room temperature and pressure**" by Jéssica A. de Oliveira[1], Jean C. da Cruz[1], Otaciro R. Nascimento, and Caue Ribeiro, published for Applied Catalysis B: Environmental.

[1] These authors contributed equally to this paper.

Reference: Applied Catalysis B: Environmental 318 (2022) 121827 [14].

Applied Catalysis B: Environmental 318 (2022) 121827

Contents lists available at ScienceDirect

Applied Catalysis B: Environmental

journal homepage: www.elsevier.com/locate/apcatb

Selective CH_4 reform to methanol through partial oxidation over Bi_2O_3 at room temperature and pressure

Jéssica A. de Oliveira [a,1], Jean C. da Cruz [a,b,1], Otaciro R. Nascimento [c], Caue Ribeiro [a,*]

[a] Embrapa Instrumentation, Rua XV de Novembro 1452, 13560–970 São Carlos, São Paulo, Brazil
[b] Departament of Chemistry, Federal University of São Carlos (UFSCar), Rodovia Washington Luiz, Monjolinho, 13565–905 São Carlos, São Paulo, Brazil
[c] Physics Institue of São Carlos, University of São Paulo (USP), Avenida João Dagnone 1100, 13563–120 São Carlos, São Paulo, Brazil

3.1. Abstract

Herein, we propose that an efficient CH_4 partial photooxidation to methanol depends on appropriate band edge positions in photocatalysts. We demonstrated our hypothesis using Bi_2O_3 since this semiconductor have a valence band favorable to produce •OH and a conduction band not advantageous to O_2•$^-$ which is crucial to keep O_2 available for •CH_3 capture and CH_3OH formation. A notably and selective partial photooxidation of methane to methanol was observed under visible light at room temperature and pressure. As a result, the productivity of methanol over Bi_2O_3 can reach approximately 3,771 μmol g^{-1} h^{-1} with c.a. 65 % selectivity avoiding overoxidation to CO_2. Isotope labeling experiment ($^{13}CH_4$) confirmed that methane acts as the carbon source of methanol and ESR measurements proved the •CH_3 and •OH generation. Besides, Bi_2O_3 exhibited good stability after 5 cycles maintaining a high and selective methanol production. These results provide insight into critical photocatalyst properties for the partial photooxidation of methane to methanol.

3.2. Introduction

Methane is a versatile feedstock for value-added chemicals production, such as oxygenated derivatives or higher hydrocarbons [28,29]. However, the intrinsic properties of methane explain its high stability and low activation for conversion to the products of interest. So far, the currently industrial route for converting methane into chemicals is through synthesis gas (H_2/CO) at high temperatures and pressures, which is an expensive and energy-consuming process [30,31]. Moreover, these reaction conditions often promote the total oxidation of methane to CO_2 and catalyst deactivation. Thus, the partial oxidation of CH_4 to methanol under mild conditions is still a challenge for methane reforming.

Photocatalytic materials can produce oxidative radicals at room temperature and pressure, using water as electron source (leading to hydroxyl radical, •OH), reducing O_2 to produce O_2•$^-$, and generating hydroperoxide radical (•OOH) in water [32]. The activation of CH_4 is reported as arising from the abstraction of a hydrogen atom from methane by holes (h^+) and reactive oxygen species to generate methyl radical (•CH_3) [33–35]. Subsequently, further transformations of methyl radicals lead to the formation of CH_3OH. It is well known that the nature and concentration of the oxidant species are fundamental to selectively oxidize methane to •CH_3 and avoid its overoxidation to CO_2. Molecular oxygen is known as

a scavenger of •CH_3 [15], which further promote the methanol selectivity through methyl hydroperoxide generation (Eq. 3.1):

$$\bullet CH_{3(aq)} + O_{2(g)} \rightarrow CH_3O_2\bullet_{(aq)} \xrightarrow{H^+_{(aq)} + e^-} CH_3OOH_{(aq)} \xrightarrow{e^-} CH_3OH_{(l)} \quad (3.1)$$

From a careful analysis of the literature, the critical step for efficient photocatalytic conversion of methane to methanol is suppressing O_2 reduction to superoxide radical to prevent overoxidation to CO_2 [1,2]. Thus, the semiconductor must have a valence band (VB) favorable to produce hydroxyl radicals and a conduction band (CB) not advantageous to $O_2\bullet^-$. Furthermore, the hydroxyl radicals' production should be fine-tuned for efficient photocatalytic conversion of CH_4, which leads those oxides frequently reported as poor oxidants as candidates for that specific case.

Bismuth oxide (Bi_2O_3) fits these premises for partial photocatalytic oxidation of CH_4 under visible illumination due to its appropriate band edge position (CB and VB at +0.3 and +3.2 V *vs.* NHE, respectively). The use of this semiconductor for CH_4 reforming arises as one of the novelty points in this work since there is a lack of information about bismuth oxide for that application. Herein, we demonstrate that Bi_2O_3 nanoparticles are efficient catalysts for CH_4 conversion to methanol under visible light at ambient conditions and that O_2 is the key oxidant for process control. The catalyst achieved high methanol yields (>1,000 μmol g^{-1} h^{-1}), selectivity over 90%, and apparent quantum yield efficiency of 24%, depending on the reaction condition. Encouraged by these results, we show that our proposal about the required band edge positions for photocatalysts seems correct to obtain significant amounts of desirable chemical products under mild conditions.

3.3. Experimental

3.3.1. Synthesis of Bi_2O_3

Bi_2O_3 was synthesized by a methodology previously described in the literature [36]. Briefly, $Bi(NO_3)_3.5H_2O$ (0.243 g) and NH_4VO_3 (0.001 g) were added in 5 mL HNO_3 (4 M) to ensure their complete dissolution. After that, 20 mL Milli-Q water was inserted, and the solution was maintained under continuous stirring for 10 min. Finally, NaOH (1 M) was used to adjust the solution pH to 12, immediately forming

yellow precipitates. The suspension was maintained at 60 °C without stirring over 24 h, and the final powder was centrifuged, cleaned with Milli-Q water until neutral pH, washed with isopropanol, and then dried at 60 °C for 10 h in air.

3.3.2. Characterization

The crystalline structure of Bi_2O_3 was analyzed by X-ray diffraction (XRD Shimadzu XRD-600 diffractometer at 30 kV and 30 mA using Cu Kα radiation (λ = 1.5418 Å) and 2 ° min^{-1}). The X-ray photoelectron spectroscopy (XPS) was performed using the Phi5000 Versa ProbeII instrument, with an incident radiation Al Kα. Surveys and high-resolution spectra were recorded using a pass energy of 0.8 eV and 0.1 eV, respectively, and for data analysis, the Casa XPS software was used. The C 1s peak was used as a calibration reference. The Tauc method [37] was utilized to calculate the indirect bandgap energy of Bi_2O_3 using the diffuse reflection spectrum (DRS, Shimadzu UV-2600 spectrophotometer). High-resolution transmission electron microscopy images (HRTEM) and scanning transmission electron microscopy (STEM) were used to identify crystalline plans and morphologies. At the same time, energy-dispersive X-ray (EDX) measurements were performed to evaluate the chemical composition of the as-synthesized sample. The colloidal alcoholic suspension of Bi_2O_3 was dripped on a carbon-coated copper grid and dried in air. The sample was then analyzed on a FEI-TECNAI G2 F20 microscope operated at 200 kV.

A Bi_2O_3 film was prepared for the electrochemical measurements to determine the experimental band edge positions. The synthesized powder was deposited over a fluorine-doped tin oxide (FTO) cleaned substrate (effective film area c.a. 1 cm^2) by spray coating using a suspension containing 1 mg mL^{-1} of Bi_2O_3 in isopropanol and 0.1 mL of Nafion® [38]. Platinum foil and Ag/AgCl was employed as counter- and reference electrode, respectively, in 0.1 M Na_2SO_4 (pH 7.0). The potential against Ag/AgCl reference ($E_{Ag/AgCl}$) was converted to NHE potential (E_{NHE}) using Eq. (2) [39]. The Mott-Schottky plot [40] was obtained from Eq. 3 where C is the space charge capacitance (F), e is the elementary charge (1.60 x 10^{-19} C), A is the Bi_2O_3 film area (1 cm^2), ε is the dielectric constant (46 for Bi_2O_3) [41], ε_0 is the permittivity of free space (8.85 x 10^{-14} F cm^{-1}), N_D is the donor density (cm^{-3}), k is the relative dielectric constant, T is the absolute temperature, q is the electronic charge (kT/q is 26 mV at room temperature [42]), E is the applied potential (V), and E_{fb} corresponds to the flat band potential (V).

$$E_{NHE} = E_{Ag/AgCl} + 0.197 \quad (3.2)$$

$$\frac{1}{C^2} = \frac{2}{e\, A^2\, \varepsilon\, \varepsilon_0\, N_D}\left(E - E_{fb} - \frac{kT}{q}\right) \quad (3.3)$$

3.3.3. Partial photooxidation of CH_4

The partial photooxidation of CH_4 to CH_3OH was performed in a 150 mL homemade-quartz reactor (Fig. 3.1). Briefly, 100 mg Bi_2O_3 was added to 100 mL deionized water, and the suspension was purged with a methane mixture containing 20%mol CH_4 in argon. After 30 min, the mixture flow was interrupted, and the reactor was sealed with Teflon-lined caps. The photoreactions were performed over 4 h, under visible illumination, atmospheric pressure, and continuous stirring. Six Philips 18 W lamps were used to provide visible light, with a total power of 108 W and light intensity of c.a. 5 mW cm^{-2} (or 2.54 x 10^{-5} Einstein min^{-1}). The reaction system was maintained at ambient conditions (25 °C and atmospheric pressure). The chemicals were added previously to the CH_4 purging for the experiments carried out with sacrificial reagents. The reaction in the presence of H_2O_2 was accomplished using a mixture of 60 mL deionized water and 40 mL of a 2.0 mM H_2O_2 solution [10]. The 1.0 mM $AgNO_3$ [43] and O_2 were also evaluated for the photooxidation experiments. But for the analysis with molecular oxygen, 1 mL pure O_2 was added into the quartz reactor only after the CH_4 purging and subsequent sealing.

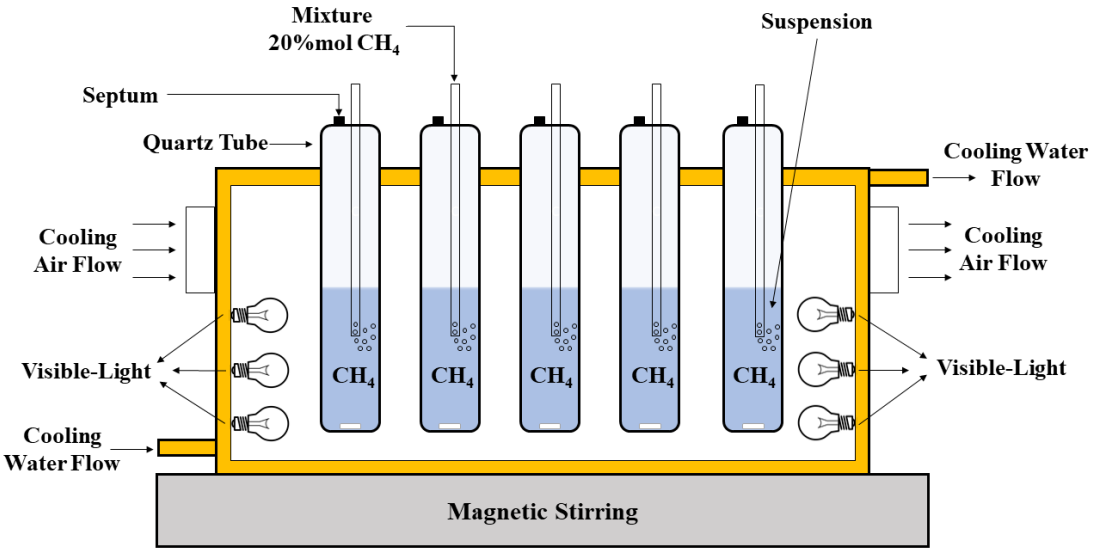

FIGURE 3.1 - Schematic illustration of the experimental setup for the partial photooxidation of CH_4 to CH_3OH.

Gas chromatography (GC Thermo CP-3800) was employed to identify and quantify the products in the gaseous aliquots (400 µL). The equipment contained a flame ionization detector (FID) at 150 °C, a thermal conductivity detector (TCD) at 200 °C, and a methanizer at 350 °C. The carrier gas was argon; a molecular sieve 13X and a Porapak Q column were also used. The detection of the liquid products was performed at 25 °C using ^{1}H nuclear magnetic resonance (NMR) (600 MHz, Ascend™ 600 Bruker). Sample aliquots (540 µL) were mixed with 60 µL of D_2O solution containing 50 mM of the standard dimethyl sulfoxide (DMSO) and 0.21 mM of the reference 3-(trimethylsilyl)propionic-2,2,3,3-d_4 acid sodium salt (TSPd_4). The water peak was suppressed through a WET procedure, and the NMR data were analyzed using MestReNova software.

The selectivity of methanol was defined as the ratio of the moles of produced methanol (n_{CH_3OH}) to the total moles of all the carbonaceous products (n_{total}), Eq. (3.4).

$$\text{Selectivity (\%)} = \left(\frac{n_{CH_3OH}}{n_{total}}\right) \text{x } 100 \tag{3.4}$$

The turnover number (TON) can be described as the quantity in moles of all the carbonaceous products per active catalytic site. Considering that the total amount

of active sites is complicated to estimate, the photocatalyst moles, $n_{photocatalyst}$, were approximated as the moles of active sites [17], according to Eq. (3.5).

$$TON = \frac{n_{total}}{n_{photocatalyst}} \quad (3.5)$$

Eq. (3.6) allows the determination of the apparent quantum yield (AQY) for methanol production, where λ is the wavelength of the incident visible light. The number of incident photons, $n_{photons}$, was estimated by the chemical actinometry methodology using a Hatchard-Parker actinometer [44]. The stoichiometric coefficients in Eq. (3.6) were determined according to the procedure described in Supplementary Information.

$$AQY(\lambda) = \frac{\text{number of transferred electrons}}{\text{number of incident photons}} \text{ x } 100$$

$$AQY(\lambda) = \frac{\left(3n_{CH_3OH} + 1n_{CH_3OOH}\right)}{n_{photons}} \text{ x } 100 \quad (3.6)$$

A Perkin Elmer luminescence spectrometer (model LS-50b) was used to probe the presence of hydroxyl radicals (•OH) by photoluminescence spectra (PL). Hydroxyl radicals react with terephthalic acid (TPA), forming 2-hydroxyterephthalic acid, Fig. A1, which can be detected by fluorescence analysis. 0.50 mM TPA was prepared in 2.0 mM NaOH [45]. Different conditions of CH_4 photooxidation were repeated with the TPA solution instead of deionized water. After 4 h of reaction under visible light, the fluorescence measurements of the liquid phase were obtained with 315 nm excitation since, at this wavelength, 2-hydroxyterephthalic acid has a peak at c.a. 425 nm. As observed from Fig. A1, the concentration of 2-hydroxyterephthalic acid is directly proportional to the concentration of •OH radicals.

Electron spin resonance (ESR) measurements was performed on a Varian E109 Model operating at X-band (9.5 GHz) and room temperature. The analyzed aqueous solutions were enclosed in a quartz cell and 5,5-dimethyl-1-pyrroline N-oxide (DMPO, c.a. 177 mM in deionized water) was used as spin trap. The as-synthesized Bi_2O_3 (5 mg) was added to 1 mL DMPO solution and subsequently 1 mL of the standard gas containing

20%mol CH_4 in argon was purged into the system. Experiments with the addition of 10 μL H_2O_2 (30%v/v) was also performed. The light-irradiation was achieved employing a 100 W halogen lamp with an incident light intensity of ~100 mW cm^{-2}. The spectral simulation was performed using the chili function of EasySpin package [46] and supported the experimental data.

Spectrophotometric method previously described in the literature was used to determine hydrogen peroxide (H_2O_2) generated *in situ* [47]. Then, 0.5 mL of the liquid aliquots of the photoreactions were mixed with 20.75 mL deionized water containing 2.5 mL of phosphate buffer (0.5 M, pH 6.0), 1 mL of KI solution (1 M), and 0.25 mL of peroxidase (POD) (100 units mL^{-1}). After 15 s, 2.5 mL of the sample was transferred into 1 cm quartz cell and analyzed by UV–Vis spectrophotometer (Shimadzu UV-1601 PC) at 350 nm.

3.4. Results and discussion

3.4.1. Characterization

We characterized the sample structure to understand the catalyst features intrinsically associated with the conversion yields. The crystallographic pattern of the as-synthesized semiconductor (Fig. 3.2a) shows pure Bi_2O_3 mainly in the δ-phase. The cubic γ-Bi_2O_3 is metastable, while δ-Bi_2O_3 is formed from the monoclinic α-Bi_2O_3 [48]. Thus, the γ- and α- polymorphous structures are observed as secondary phases of the as-synthesized Bi_2O_3. Bismuth oxide with multiple phases can be easily synthesized in practice, usually forming homojunctions [49,50] that can positively affect the photoactivity [51]. The chemical states and the composition of Bi_2O_3 sample were also examined by XPS. The XPS survey spectrum (Fig. A2a) confirmed the presence of only Bi, O, and C elements in the as-synthesized Bi_2O_3. No V 2p signal was observed (Fig. A2b), confirming the successful synthesis of Bi_2O_3 without impurities. In the high-resolution Bi 4f spectrum (Fig. 3.2b), two fitted peaks at 157.9 and 163.2 eV can be ascribed to Bi $4f_{7/2}$ and Bi $4f_{5/2}$ of Bi^{3+}, respectively [52]. The O 1s high-resolution spectrum (Fig. 3.2c) can be deconvoluted into three peaks at 528.6, 529.9, and 531.7 eV, which can be assigned to the lattice oxygen, oxygen vacancies, and surface adsorbed oxygen species, respectively [53,54]. Furthermore, the oxygen vacancies in the Bi_2O_3-surface facilitates the adsorption and activation of the adsorbed oxygen to form reactive species [55].

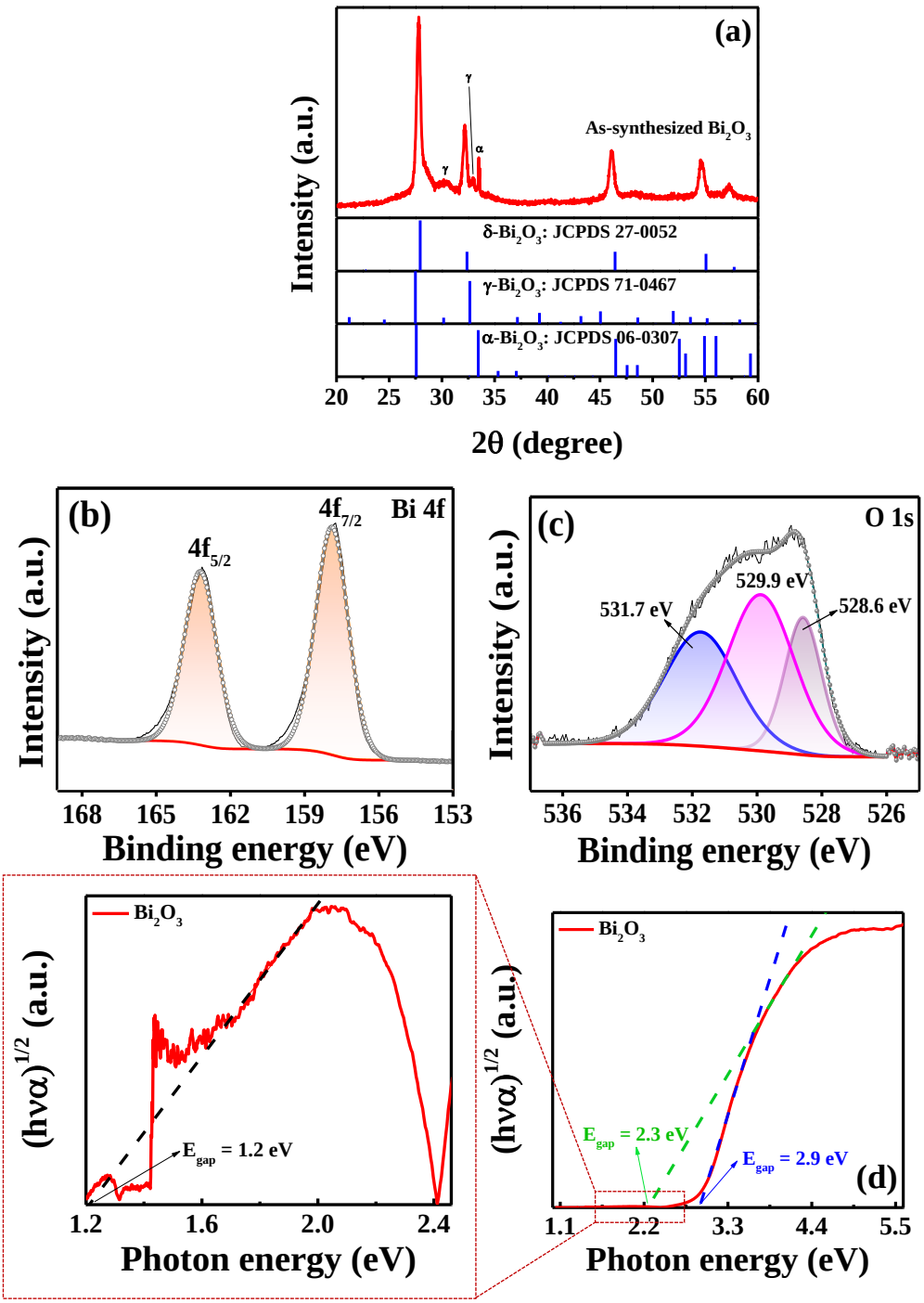

FIGURE 3.2 - (a) XRD patterns, high-resolution XPS spectra of (b) Bi 4f and (c) O 1s, and (d) Tauc plot of the as-synthesized Bi_2O_3.

Regarding the optical properties, the spectrum in Fig. 3.2(d) shows that our Bi_2O_3 sample presents narrow indirect bandgap values of c.a. 2.9 eV (δ-Bi_2O_3) [36], 2.3 eV (α-Bi_2O_3) [56] and an extra photon energy shoulder at about 1.2 eV (γ-Bi_2O_3) [57] attributed to the existence of multiple phases. According to Fig. A3, the photon absorption

occurs between 520 and 340 nm in the blue/violet region of the visible-light spectrum, demonstrating that the visible bandgap could provide light-harvesting for favoring the photoactivity under sunlight conditions. STEM images showed that the as-synthesized Bi_2O_3 presents a cubic morphology (Fig. 3.3a) between 50-200 nm containing nanoparticles of ~3 nm attached to the cube surface in an organized fashion (inset of Fig. 3.3b). A *d*-spacing of 3.8 Å was observed in Fig. 3.3c, corresponding to the (110) plane of δ-Bi_2O_3. Furthermore, the EDX analysis (Fig. 3.3d) confirms a homogeneous distribution of Bi and O elements without impurities, which is consistent with XPS analysis (Fig A3).

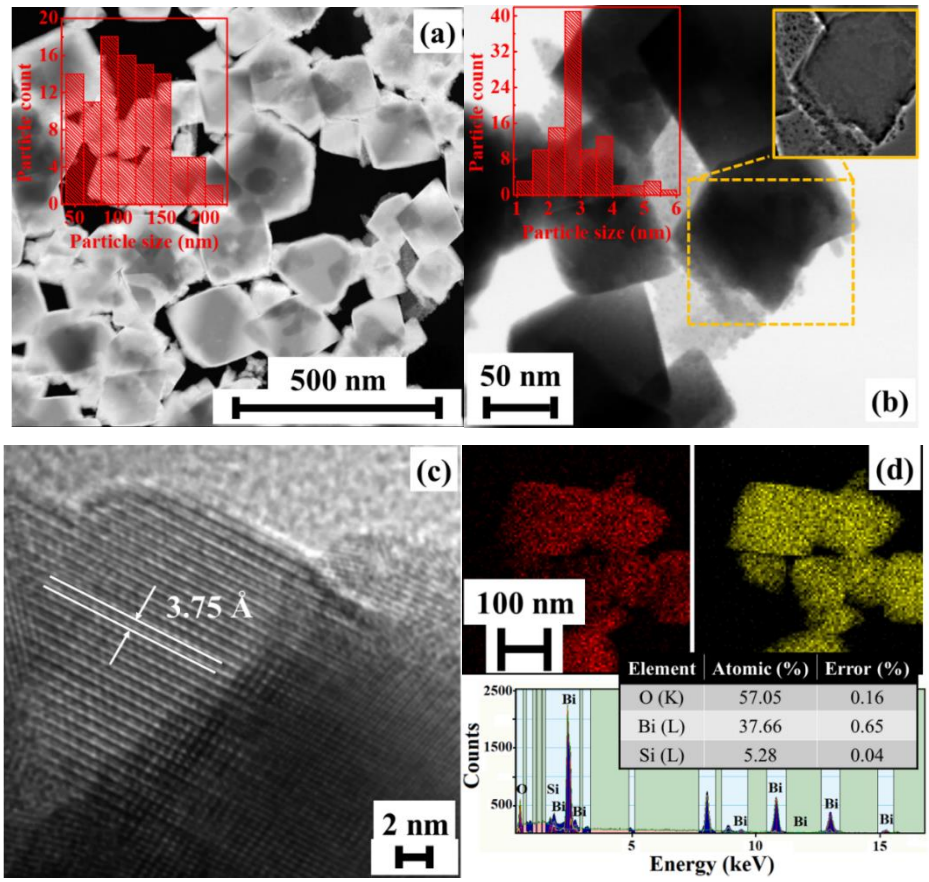

FIGURE 3.3 - (a-b) STEM dark- and bright-field images, (c) HRTEM micrography, and (d) EDX of the as-synthesized Bi_2O_3.

Fig. 3.4a shows the Mott-Schottky plot for the as-synthesized Bi_2O_3 in which the positive slope is characteristic of an *n*-type semiconductor [42]. The flat-band potential (φ_{fb}) was determined at +0.51 V *vs.* NHE from the *x*-axis intercepts. For *n*-type semiconductors, this φ_{fb} value can be approximated to the conduction band minimum

(CB) [58,59]. Since the as-synthesized sample exhibited only one positive slope, all the Bi_2O_3 crystalline phases present the same CB. Considering the bandgaps determined from DRS (Fig. 3.2b), the CB of Bi_2O_3-homojunction was estimated at +0.5 V *vs.* NHE while the valence band (VB) of δ-,α-, and γ-Bi_2O_3 were approximated at +3.4 V, +2.8, and +1.7 V *vs.* NHE, respectively. The slopes in Fig. 3.4a provide the average donor density (1.21 x 10^{17} cm^{-3}) that suggested a carrier density appropriate for photocatalytic applications [42,60].

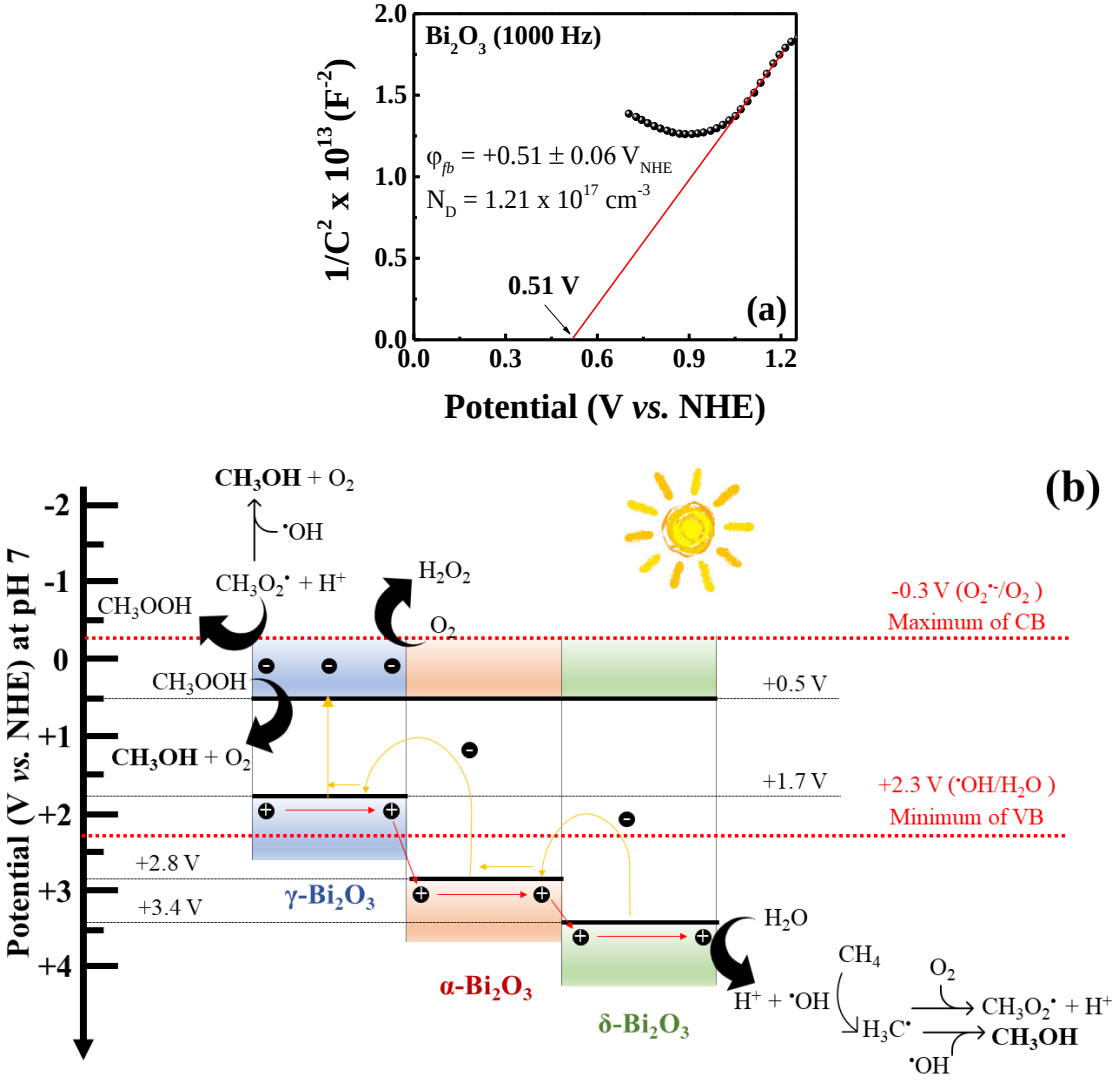

FIGURE 3.4 - (a) Mott-Schottky plot for the as-synthesized Bi_2O_3/FTO. The experiment was achieved in 0.1 M Na_2SO_4 (pH 7.0). (b) Bi_2O_3-homojunction Z-scheme: required band edge positions for semiconductors being adequate photocatalysts for the partial oxidation of methane to methanol.

PL experiments (Fig. A4) using terephthalic acid as fluorescent probe showed the formation of hydroxyl radicals. Terephthalic acid traps •OH species to produce 2-hydroxyterephthalic acid that emits a fluorescence sign at c.a. 425 nm with 315 nm excitation. Consequently, the hydroxyl radicals can be detected indirectly since the emission peak attributed to 2-hydroxyterephthalic acid is proportional to the concentration of •OH species [45]. As our homojunction system produces •OH, the photocatalytic mechanism may follow a Z-scheme pathway for electron-hole separation whereas γ-Bi_2O_3 does not present the require potential to form •OH. Thus, the photoinduced holes migrated to the δ-Bi_2O_3 phase. As reported in the literature, the presence of more than one valence state in a Z-scheme suggests that the photogenerated electrons are hopped to the neighboring intermediate state, actively transporting the electron from the high valence state to the low valence one until the excitation to the conduction band of γ-Bi_2O_3 [61,62]. Therefore, the CB/VB positions of the as-synthesized Bi_2O_3 can be schematically represented according to Fig. 3.4b, which emphasizes the required band edge positions for a semiconductor being a promising photocatalyst in partial photooxidation of CH_4 to CH_3OH. In other words, the CB edge position is more positive than the reduction potential of O_2 to $O_2^{\bullet -}$ and the VB edge position is above the •OH generation potential. All the reduction potentials are listed as reported in the literature [63,64].

3.4.2. Partial photooxidation of CH_4

According to Fig. 3.4b, the photooxidation of CH_4 to CH_3OH is a radical mechanism. To confirm this hypothesis, ESR measurements (Fig. 3.5) were performed in conditions similar to those used to accomplish the partial methane photooxidation. Methyl and hydroxyl radicals were detected as expected from the proposed reaction mechanism. The presence of the stable radical adducts DMPO-$(OH)_2$ can be observed only in high concentrations of •OH, further indicating the ability of our Bi_2O_3-homojunction Z-scheme in generating hydroxyl radicals. However, Fig. 3.5a showed that the simultaneous addition of H_2O_2 and CH_4 led to the inhibition of $\bullet CH_3$ generation since the H_2O_2 increases the •OH concentration and that could be a competitive reaction with the methyl radical formation. Thus, as previously proposed, there is an optimal •OH concentration for the partial photooxidation of CH_4. Hydroperoxyl radicals (•OOH) were also identified in the presence of CH_4 and light, agreeing with the route of CH_3OOH formation.

Unsurprisingly, superoxide radical was not observed, confirming the Motty-Schottky results that our system does not present the required band edge position to reduce oxygen molecules to $O_2^{\bullet -}$.

A remarkable finding is that even before the light-irradiation the generation of $\bullet CH_3$ is observed (Fig. 3.5b), increasing its signal intensity with time (Fig. A5a). It suggests high interaction of methane and Bi_2O_3-surfaces. A simulation of the presence of these different radicals (Fig. A5c) in the reaction medium was performed (Fig. A5b) and a coherence was revealed between the experimental and simulated ESR data. The Cr(III):MgO signal (g = 1.9797) (Fig. A5d) was used to calibrate magnetic field and relative signal intensities.

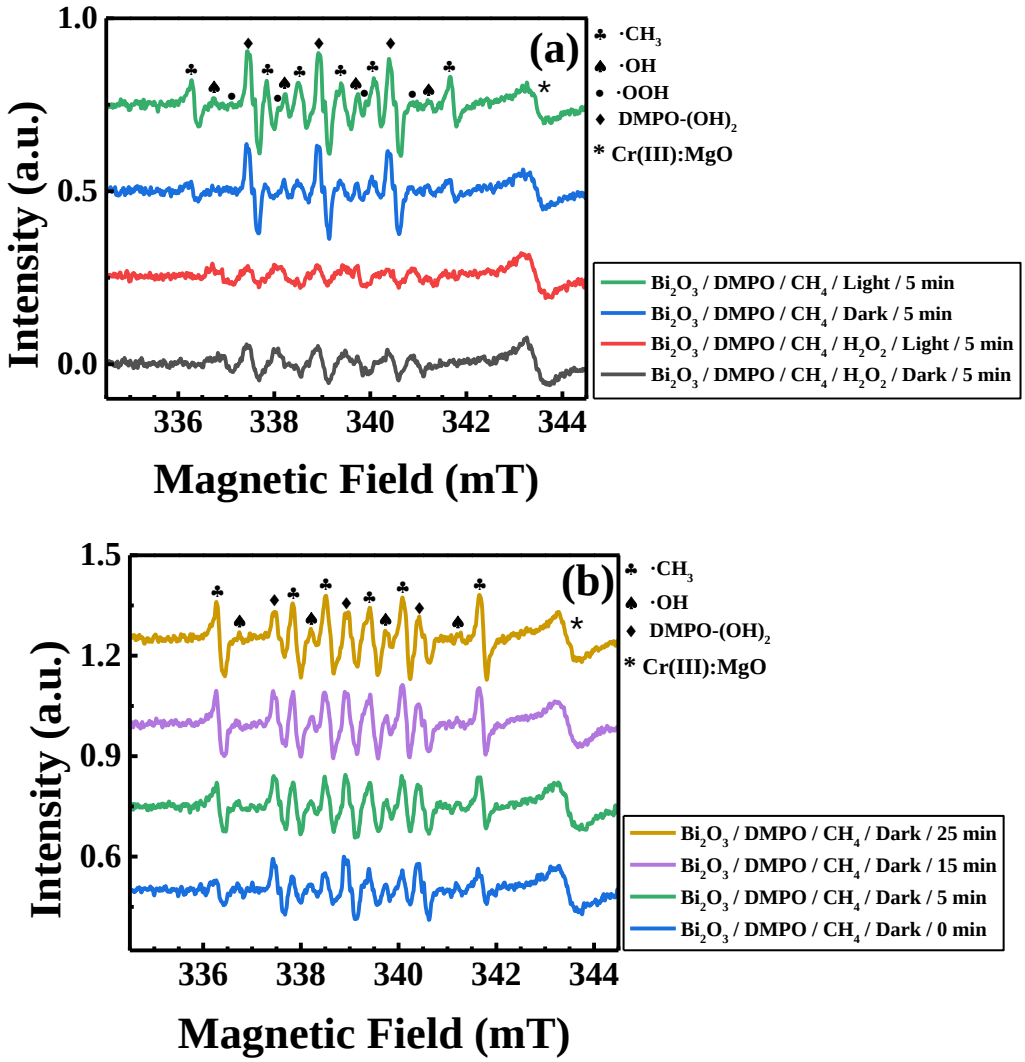

FIGURE 3.5 - Experimental ESR spectra of the DMPO solution containing the as-synthesized Bi_2O_3 and the methane standard gas under (a) light-irradiation and (b) dark. Cr(III):MgO signal (g = 1.9797) used to calibrate magnetic field and relative signal intensities.

A comprehensive view of our photocatalytic results is depicted in Table 3.1, which shows the CH_4 conversion yields for all the studied conditions with Bi_2O_3 as the photocatalyst. Notably, this material presented good photoactivity for the CH_4 conversion into valuable organic compounds, producing around 208 μmol g^{-1} h^{-1} of methanol (Table 3.1). As demonstrated by the ESR analysis (Fig. 3.5), the Bi_2O_3 surface actives the methane even without illumination. Analysis of liquid aliquot was performed after 30 min purge of the CH_4 standard gas to investigate the possible products formed by the dark-generated methyl radical. Methanol, ethanol, acetic acid, dissolved methane, and glycerol were detected, probably due to the reactivity of oxygen vacancies, observed by XPS (Fig. 3.2c), with adsorbed CH_4. Oxygen vacancies can enhance the adsorption and fixation of CH_4 on the photocatalyst surface [65,66].

TABLE 3.1 - Production rate of liquid chemicals from the partial photooxidation of CH_4 by Bi_2O_3*.

Sample	Production rate (μmol g^{-1} h^{-1})			
	Methanol	**Acetone**	**Acetic acid**	**Ethanol**
**Bi_2O_3 after 30 min purge	1.00 μmol	0.00	0.20 μmol	0.60 μmol
Bi_2O_3	207.75	4.27	76.50	10.09
$Bi_2O_3/AgNO_3$	135.51	4.42	1.17	5.41
Bi_2O_3/H_2O_2	726.15	165.03	492.16	22.01
Bi_2O_3/O_2	**1,199.61**	**221.88**	**540.82**	**8.03**
***Bi_2O_3/Dark	25.76	0.00	0.00	0.00
H_2O	53.88	11.00	0.00	0.00

* Reaction conditions: 1 g L^{-1} Bi_2O_3 in 100 mL under visible-light illumination (108 W and ~5 mW cm^{-2}). The production rates were determined after 4 h of reaction using a mixture of CH_4 in argon (20%mol CH_4).

** This condition represents the liquid chemicals produced by the as-synthesized Bi_2O_3 after 30 min CH_4 purge i.e. before the beginning of the photocatalytic process. Dissolved methane (7.4 μmol) and glycerol (23.7 μmol) were also detected. The products are presented only as moles (μmol) because in this experimental setup there are no photoreactions performed over 4 h.

*** This condition represents the liquid chemicals produced by the as-synthesized Bi_2O_3 under dark over 4 h. Glycerol was also detected in a production rate of c.a. 44 μmol g^{-1} h^{-1}.

One can see that the methanol yields are much higher than the other products for all conditions, though significantly high C_{2+} products (e.g., acetone and acetic acid) are seen in some situations. Indeed, the significant amounts of higher carbon species in the Bi_2O_3/H_2O_2 and Bi_2O_3/O_2 conditions are a further indicative of the importance of hydrogen peroxide and molecular oxygen to improve the methanol formation since these byproducts are originated from methanol [67,68]. Please, see in the Appendix the reaction steps that we propose to produce the different chemicals from the CH_4 photooxidation.

The •OH is expected to oxidize methane and generate methyl radicals ($•CH_3$) that finally react with •OH to form methanol, Eqs. (3.7-3.10) [2,35]. On the other hand, experiments of CH_4 oxidation with isotopically labeled oxygen ($^{18}O_2$) proved that O_2 provides the oxygen for the CH_3OH [15,17]. Thus, it has been proposed that molecular oxygen acts as a scavenger of $•CH_3$, consequently enhancing the production of methanol, Eqs. (3.11-3.12). In this sense, the semiconductor should have a conduction band below the O_2 potential to $O_2•^-$ for O_2 only scavenging $•CH_3$ and not the photogenerated electrons.

$$Bi_2O_{3(s)} \xrightarrow{h\nu \text{ (visible-light)}} h^+ + e^- \quad (3.7)$$

$$H_2O_{(l)} + h^+ \rightarrow •OH_{(aq)} + H^+_{(aq)} \quad (3.8)$$

$$CH_{4(aq)} + •OH_{(aq)} \rightarrow •CH_{3(aq)} + H_2O_{(l)} \quad (3.9)$$

$$•CH_{3(aq)} + •OH_{(aq)} \rightarrow CH_3OH_{(aq)} \quad (3.10)$$

$$•CH_{3(aq)} + O_{2(g)} \rightarrow CH_3O_2•_{(aq)} \quad (3.11)$$

$$CH_3O_2•_{(aq)} + •OH_{(aq)} \rightarrow CH_3OH_{(aq)} + O_{2(aq)} \quad (3.12)$$

Studies have attempted to further improve the formation and selectivity of methanol by adding counter reagents into the reaction medium to modify the concentration of hydroxyl radicals or improve the $•CH_3$ scavenging, such as molecular oxygen [15], hydrogen peroxide [1], and $AgNO_3$. For each component, we expect a different behavior: O_2 inclusion increases its availability in the medium, in which H_2O_2 may be produced from O_2 reduction (O_2/H_2O_2: 0.695 V *vs.* NHE) (Eq. 3.13) [69]; H_2O_2

oxidation increases the dissolved O_2 (Eq. 3.14) while H_2O_2 reduction leads to OH^- and •OH (H_2O_2/•OH: 1.14 V *vs.* NHE) (Eq. 3.15); nitrate ions reduce the •OH concentration (Eq. 3.16) [13] while silver improves the separation of the photogenerated charges (Eq. 3.17) [43]. To assess the formation of hydrogen peroxide from O_2 reduction, spectrophotometric method was performed (Fig. A6) [47] and the H_2O_2 generation was confirmed. Along with these observations, all the mentioned chemicals were evaluated for methane oxidation to methanol using the Bi_2O_3 as photocatalysts (Fig. 3.6).

$$O_{2(g)} + 2H^+_{(aq)} + 2e^- \rightarrow H_2O_{2(aq)} \quad (3.13)$$

$$H_2O_{2(aq)} \rightarrow H_2O_{(l)} + 1/2\, O_{2(g)} \quad (3.14)$$

$$H_2O_{2(aq)} \rightarrow \bullet OH_{(aq)} + OH^-_{(aq)} \quad (3.15)$$

$$NO_3^-{}_{(aq)} + \bullet OH_{(aq)} + H^+_{(aq)} \rightarrow NO_3\bullet_{(aq)} + H_2O_{(l)} \quad (3.16)$$

$$Ag^+_{(aq)} + e^- \rightarrow Ag^0_{(s)} \quad (3.17)$$

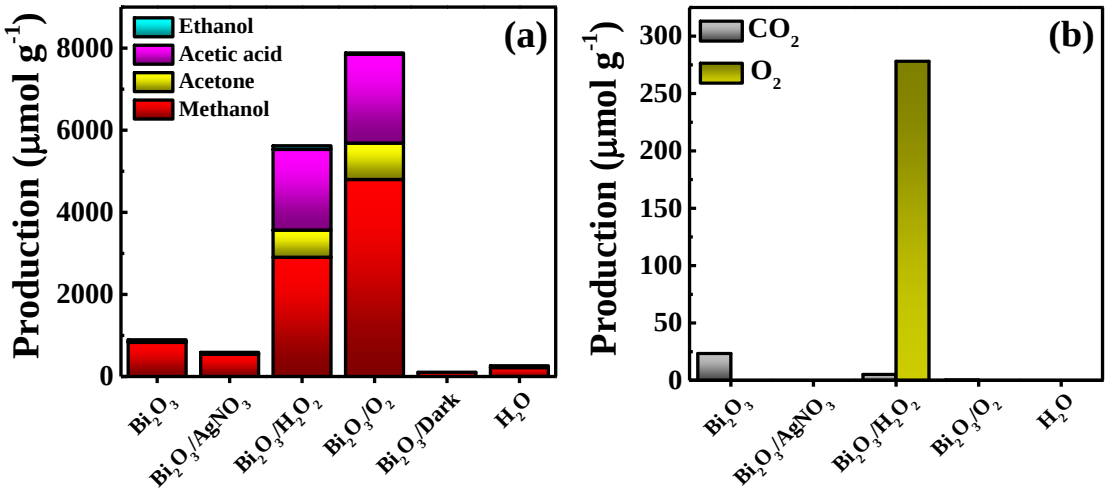

FIGURE 3.6 - Production of chemicals from the partial photooxidation of CH_4 after 4 h: (a) liquid compounds and (b) gaseous compounds. The experiments were carried out using visible-light illumination and 1 g L^{-1} Bi_2O_3 in 100 mL solution at ambient conditions.

$AgNO_3$ negatively affected the photoactivity of Bi_2O_3 since nitrate ions decrease the methanol production by the decrease of •OH concentration and the formation of metallic silver that blocks the active sites of the semiconductor. Unsurprisingly, H_2O_2 and O_2 considerably enhance the methanol production (Fig. 3.6a), mainly the molecular oxygen that seems to play a critical role in the partial oxidation of methane to methanol by the output of ~1,200 μmol g^{-1} h^{-1}. Regarding O_2 production, the reaction carried out with H_2O_2 produced high amounts of O_2 (~280 μmol g^{-1} h^{-1}) due to the competitive reaction of H_2O_2 decomposition as shown in Eq. (3.14).

It has been proposed that methanol can also be formed from methyl hydroperoxide (CH_3OOH), Eq. 3.18 [17]. For the routes of methanol production represented by Eqs. 3.12 and 3.19, the O_2 plays an essential role through the •CH_3 scavenging. Trace amounts of CH_3OOH (<5 μmol g^{-1} h^{-1}) were observed only in the reactions with H_2O_2 and O_2, probably due to the difficulty of detecting this compound. These results were consistent with ESR measurements (Fig 3.5a). Despite being no consensus about the primary mechanism of CH_3OH production, the overall photoactivity is more sensitive to the presence of O_2 than H_2O_2. All the ^1H NMR are presented in the Supplementary Information (Fig. A7-A8). GC analyses were also used as complementary analytical technique to confirm the product concentration and estimate the amount of dissolved CH_4 (Fig. A9-A13).

$$CH_3O_2\bullet_{(aq)} + H^+_{(aq)} + e^- \rightarrow CH_3OOH_{(aq)} \quad (3.18)$$

$$CH_3OOH_{(aq)} + 2e^- + 2H^+_{(aq)} \rightarrow CH_3OH_{(aq)} + H_2O_{(l)} \quad (3.19)$$

XRD analyses on the photocatalyst were performed after the photoreactions to identify a possible explanation for this trend, and no significant changes of the crystalline phases were observed (Fig. A15). Comparing our best result (Bi_2O_3/O_2) with the production rates reported in the literature (Fig. 3.7), it is noticeable that our work obtained comparable yields of methanol. The highest methanol formation using photocatalysis found in the literature (>10,000 μmol g^{-1} h^{-1}) was achieved under high pressure of 4 MPa (Table A3.1), while we performed all the photoreactions at atmospheric pressure. It is also indicative that selecting a semiconductor with suitable band edge positions is crucial for improving methanol formation. Furthermore, it is outstanding that

no carbon dioxide or small quantities of CO_2 was produced over Bi_2O_3 in our experiments (Fig. 3.6b). The reaction without a semiconductor and under dark also showed that the photocatalyst and visible illumination is essential to convert CH_4 into CH_3OH (Fig. 3.6a).

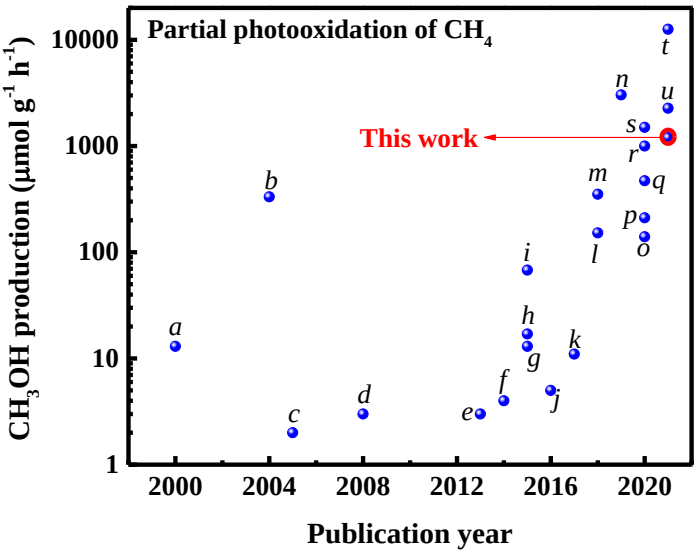

FIGURE 3.7 - Production rates of methanol from the partial photooxidation of CH_4: comparison between the best result obtained in this work and the values reported in the literature in the last 20 years. The alphabetic entries are related to the reaction conditions presented in Table A3.1.

Although pure Bi_2O_3 and Bi_2O_3 in the presence of $AgNO_3$ exhibited poor methanol production rates, the highest methanol selectivity was obtained in these conditions (Fig. 3.8a). The turnover number (TON) for Bi_2O_3/O_2, calculated as 3.7, suggests that the CH_4 oxidation is an authentic photocatalytic reaction (TON > 1) [17]. The apparent quantum yield (AQY), Fig. 3.8b, demonstrated that the photonic efficiency of our process reached approximately 24% of efficiency in absorbing photons to form methanol. The stability of the photocatalyst was examined over five consecutive cycle tests with each run of 4 h and without any activation processes between cyclic tests (Fig. 3.8c). Even after the 5th cycle, the production and selectivity for methanol still maintain at c.a. 704 μmol g^{-1} and 73%, respectively, exhibiting the outstanding stability of Bi_2O_3.

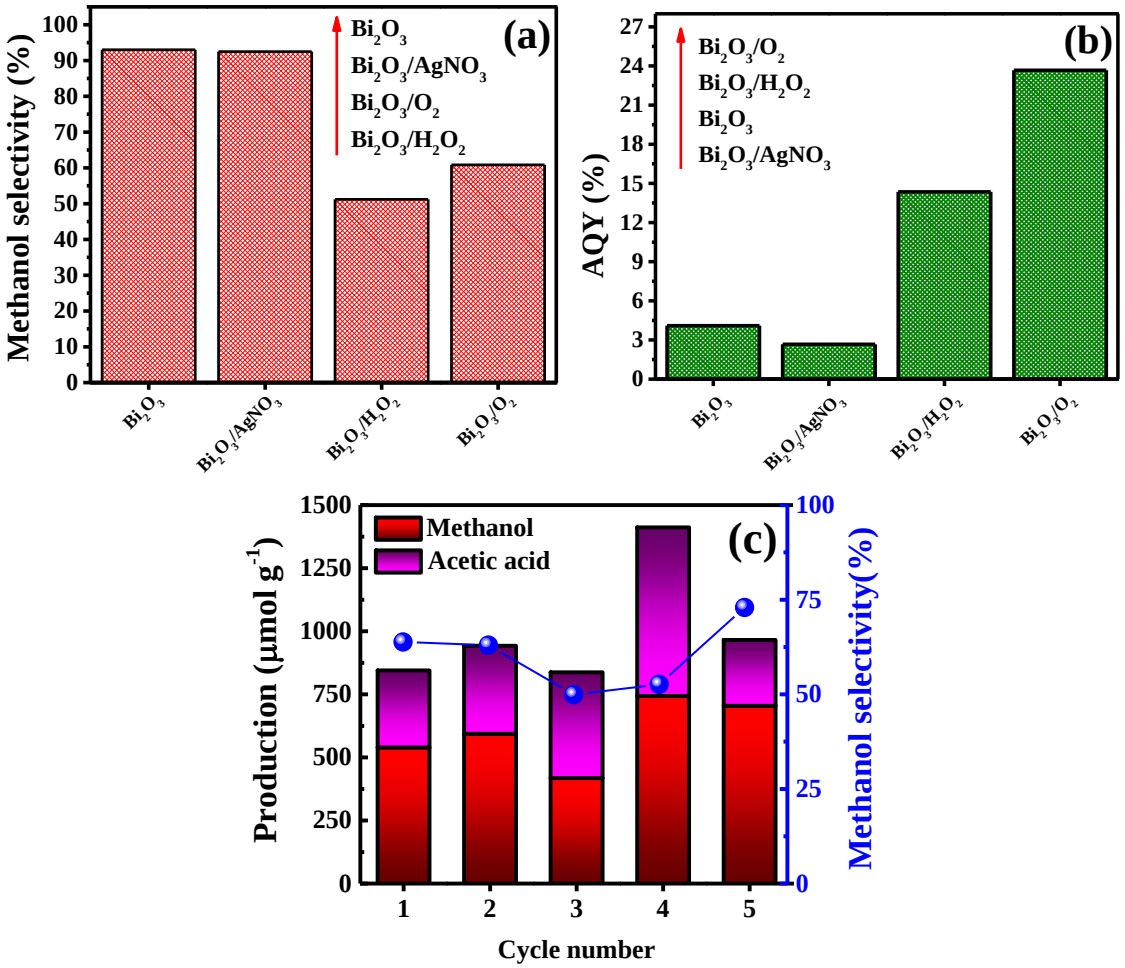

FIGURE 3.8 - (a) Selectivity of the photoreaction for the methanol formation; (b) apparent quantum yield for the methanol production; and (c) recycle reactions of the partial photooxidation of CH_4 using 1 g L^{-1} Bi_2O_3 in 100 mL deionized water. Each cycle lasts 4 h under visible-light illumination.

The methane concentration is also influent in the kinetics. We performed the reaction with pure CH_4 (99%), 5 times the original CH_4 concentration, using Bi_2O_3 with no counter reactant. As shown in Fig. 3.9a, the catalyst led to high production rates of methanol (~3,771 μmol g^{-1} h^{-1}) and acetic acid (~2,036 μmol g^{-1} h^{-1}) after 4 h of reaction under visible-light illumination, i.e., a significantly higher TON. It shows that the reaction can be optimized to even better yields. The selectivity of methanol was around 65%. In addition, Bi_2O_3 exhibited no activity to CO and CO_2 in this condition, as expected since the acetic acid pathway involves the coupling of methyl radicals and *CO [70].

Further to prove that CH_4 is the carbon source for methanol generation, we conducted an isotope labeling experiment with $^{13}CH_4$ as the reactant. As displayed in Fig. 3.9b, the ^{13}C NMR spectrum shows one peak at 48.6 ppm attributed to the methanol, confirming that CH_3OH comes from CH_4 photooxidation.

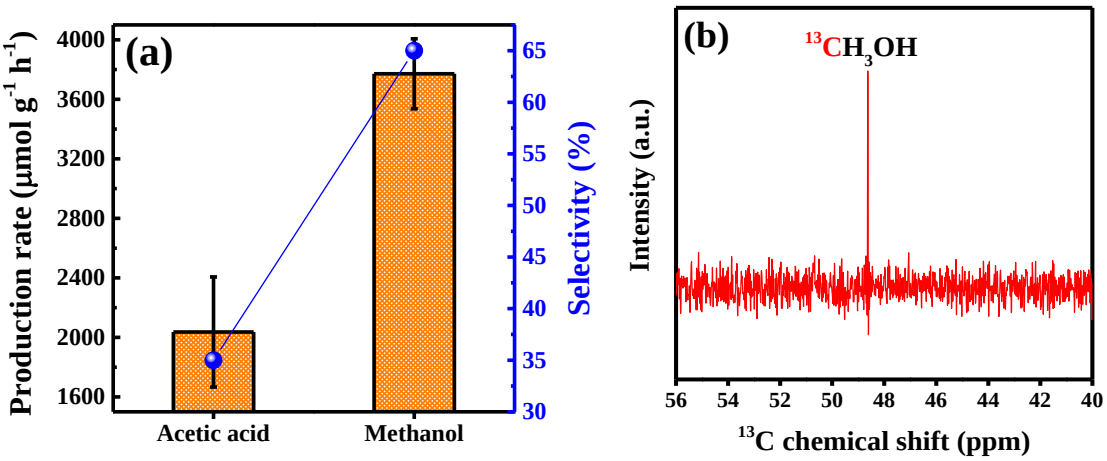

FIGURE 3.9 - (a) Production rates of chemicals from the partial photooxidation of pure CH_4 after 4 h. The experiments were carried out using visible-light illumination and 1 g L^{-1} Bi_2O_3 in 100 mL solution at ambient conditions. (b) ^{13}C NMR spectrum for the reaction solution.

3.5. Conclusion

We propose that the partial oxidation of CH_4 to CH_3OH is favored catalyzed by semiconductors with a conduction band edge position below the reduction potential of $O_2{\bullet}^-/O_2$ (-0.3 V *vs.* NHE at pH 7), allowing the O_2 coupling with $\bullet CH_3$. Bi_2O_3 is an active photocatalyst for the partial oxidation of methane to methanol under visible-light and ambient conditions since, having the required band edge positions, yielded 3,700 μmol g^{-1} CH_3OH from pure CH_4 at room temperature and atmospheric pressure. ESR experiments proved the formation of $\bullet CH_3$ and $\bullet OH$ while no superoxide radical was detected, as expected by the Mott-Schottky measurements. O_2 has a dominant role by capturing $\bullet CH_3$ to form methanol and the H_2O_2 oxidation can be used to positively affects the local production of O_2.

4. CHAPTER IV: CH_4 reforming driven by BiOCl as photocatalyst

The content of this chapter is an adaptation of the article entitled **"Unveiling the selective CH_4 photocatalytic reform to oxygenates under visible light driven by intermediate radicals formation"** by Jean C. da Cruz, Jéssica A. de Oliveira, Otaciro R. Nascimento, Sanjay Mathur, and Caue Ribeiro that is under production.

4.1. Abstract

We demonstrated that chlorine-intermediates are a suitable pathway for a controlled methane photooxidation to methanol *via* chloromethane formation. Beyond that we showed that structural chloride in a perovskite-type crystalline structure can be used in a cycle-system in which the interlayer Cl^- is easily removed from the unity cell and the excess of Cl^- in solution is readily added back to the interlayer to regenerate the photocatalyst. Chlorine species in solution react quickly with CH_4 to form CH_3Cl that, by a simple substitution reaction with hydroxyl ion, lately produces methanol. Our best CH_3OH production was around 1300 μmol g^{-1} without the need of foreign chemicals, demonstrating the feasibility of our proposed close-system for continuous methanol generation.

4.2. Introduction

Methane is an inert molecule mainly due to the stability of the C–H bonds (434 KJ mol^{-1}) [2], poor polarizability (2.84 x 10^{-40} C^2 m^2 J^{-1}) [12], and low proton affinity (544 KJ mol^{-1}) [71]. The methane conversion to oxygenates, especially methanol, is of great interest since in addition to minimizing the emission of one of the most harmful greenhouse gases [3], CH_3OH can be used as a building block for many chemicals. However, the harsher temperature/pressure conditions (400-800 K and 20-40 bar) [1] for current CH_4 to methanol makes the process cost- and energy- intensive, limiting its potential uses. The photochemical CH_4 oxidation by solar light could provide a sustainable alternative, but it lacks on an adequate way to activate this molecule in a very selective manner, avoiding its complete oxidation to CO_2 [72]. H_2O_2 is reported as an adequate activator for methane-controlled oxidation [1] but the molecular mechanism is still disputed since in photocatalytical systems, H_2O_2 can be either oxidized, leading to O_2, or reduced, leading to OH^- + •OH. Thus, the control of the reaction is still deficient.

Recently we demonstrated that semiconductors with low conduction band energies can increase the methane conversion to methanol. We showed that Bi_2O_3, as a model material for a proof-of-concept, produces •OH by holes in valence band that can abstract one hydrogen from methane. However, the controlled oxidation (i.e., methanol formation) only occurs if O_2 is still present – in other words, the catalyst should have appropriate band edge positions to avoid the reaction O_2 => O_2•$^-$. We showed that the role

of H_2O_2 is to increase the O_2 concentration by its oxidation, showing that the hydrogen peroxide is not the methane activator. Indeed, we also demonstrated that the increase of O_2 concentration by bubbling can be more efficient than H_2O_2 addition [14,16].

Based in these findings, we propose that the reaction control requires intermediates that can be adequately converted to CH_3OH, avoiding the overoxidation. CH_4 chlorination is the oldest substitution reaction [73,74] and chloromethane (CH_3Cl) is recognized as an appealing intermediate to produce methanol and ethers by simple mixture in water [75,76]. The reaction of CH_4 against Cl radicals easily leads to CH_3Cl, being these radicals formed by Cl_2 irradiation under UV light, with high selectivity for CH_3Cl under a CH_4:Cl_2 molar ratio > 10 [75]. Although the literature reports methane oxidation in the presence of chloride salts [43], the role of Cl^- was interpreted by them as only affecting the photogenerated charges' separation. Indeed, some reports explore the electrochemical Cl_2 production followed by radical formation by UV irradiation, or by modification of electrochemical conditions [76,77], and CH_4 halogenation induced by photocatalysts [78–80]. Nevertheless, the solar light utilization in these setups is still limited since the reaction is not activated by visible light. To that, materials that can perform the Cl^- reduction are the best candidates.

Thus, we propose to control the CH_4 oxidation by an indirect route, driven by the formation of Cl radicals in solution using Bi-based semiconductors excited in visible light. Bi_2O_3 is again a promising candidate, but we propose that BiOCl is more adequate to promote methanol formation *via* CH_3Cl as intermediate. The chloride ion into its crystalline structure could be continuously used to enhance the photoactivity while the photocatalyst can be regenerated by the Cl^- in solution coming from the substitution reaction between chloromethane and hydroxyl ion. BiOCl is composed by $[Bi_2O_2]^{2+}$ layers intercalated by double layers of Cl^- organized in a perovskite structure. As the chloride ions are bonded to the adjacent layers by weak Van der Waals interactions, Cl^- can be easily removed from the crystal structure and the excess of Cl^- in solution can be readily added back to the crystalline structure [81,82]. This cycle-based system is represented in Fig. 4.1. Therefore, we hypothesize that the surface Cl can be reduced to form the methyl radical, with no need of further chloride addition. Our results show that BiOCl, a nontoxic, affordable, and eco-friendly semiconductor [74], promotes the reaction with no need of O_2 to control the reaction, i.e., the reaction was done directly in water, showing a new way for selective oxygenates formation in a sustainable manner.

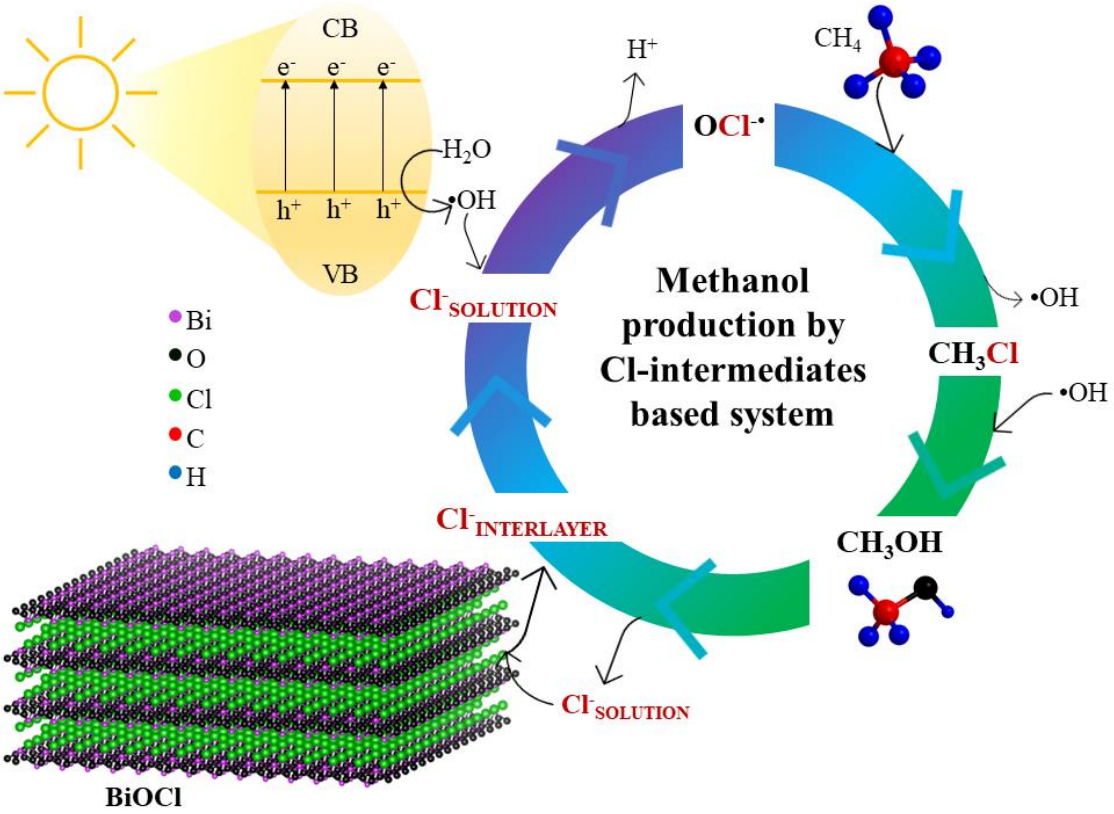

FIGURE 4.1 - Schematic illustration of the proposed mechanism for methanol production by chlorine-intermediates cycle-based system.

4.3. Experimental

4.3.1. Synthesis of Bi_2O_3 and BiOCl

Bismuth oxide (Bi_2O_3) was synthesized by the method described elsewhere [14,36]. BiOCl was synthesized by a precipitation method described elsewhere [14,36]. Briefly, 100 mM $Bi(NO_3)_3.5H_2O$ (0.243 g, Vetec) and 2 mM NH_4VO_3 (0.001 g, Vetec) were dissolved in 4 M HCl (5 mL, Synth). Afterwards, 20 ml deionized water was added, and the final solution was continuously stirred for 10 min. Then, the solution pH was adjusted to 12 by the addition of 1 M NaOH (Synth) and yellow powders were immediately precipitated. The suspension was heated at 60 °C for 24 h without stirring and the final products were centrifugated and washed with deionized water for several times until neutral pH. Finally, the samples were washed one more time with isopropanol and dried at 80 °C for 10 h in air. All the chemicals were used as received without further purification.

4.3.2. Characterization

X-ray diffraction (XRD) was carried out at a Shimadzu XRD-600 diffractometer using Cu Kα radiation (λ = 1.5418 Å), 30 kV, 30 mA, and 2° min^{-1}. The Phi5000 Versa ProbeII equipment and an incident radiation of Al Kα were used to perform the X-ray photoelectron spectroscopy (XPS). The Casa XPS software was used to analyze the data. Surveys and high-resolution spectra were obtained using pass energies of 0.8 eV and 0.1 eV, respectively. The C 1s peak was utilized as a calibration reference. Colloidal alcoholic suspension of BiOCl was prepared, dripped on a carbon-coated copper grid, and allowed to dry in the open air. A FEI-TECNAI G2 F20 and Thermo Fisher Scientific Talos F200C microscopes running at 200 kV were then used to evaluate the sample by high-resolution transmission electron microscopy (HRTEM) and scanning transmission electron microscopy (STEM).

4.3.3. Photocatalysis: CH_4 reforming

The CH_4 reforming was performed in a 150 mL homemade-quartz reactor (Fig. 3.1). In brief, 100 mg of catalyst was mixed into 100 mL of deionized water. The suspension was continuously purged with a mixture of methane (20%mol) in argon for 30 min. Then, the gas flow had been interrupted, and Teflon-lined caps were used to seal the system. Experiments containing appropriate amounts of sacrificial reagents were also conducted to assess the role of these chemicals in the photoactivity: (i) 2 mM $NaClO_2$ (0.018 g, Aldrich); (ii) 1 mL O_2 (99.999%); and (iii) 2 mM $NaClO_2$ (0.018 g, Aldrich) and 2 mM HCl (16 μL, 38%, Neon). $NaClO_2$ and HCl were added to the BiOCl suspension prior to the purging process while O_2 was introduced immediately after the CH_4 purging and subsequent seal of the photoreactors. The 2.0 mM NaCl (0.012 g, Synth) and 1 mM $FeCl_3$ [43] (0.016 g, Vetec) were used with the concentrations usually reported on the literature for partial CH_4 photooxidation. The experiments with 6.0 mM Cl^- were performed using the salts $CuCl_2$ (0.051 g, Vetec), $CoCl_2$ (0.071 g, Dinâmica), $CrCl_3$ (0.053 g, Vetec), $InCl_3$ (0.044 g, Aldrich), and $SnCl_2$ (0.068 g, Synth). The photoreactions were carried out for 4 h in the presence of visible light using six Philips 18 W lamps with a total power of 108 W and light intensity of approximately 5 mW cm^{-2} (or 2.54 x 10^{-5} Einsten min^{-1}). The system was kept at ambient temperature, atmospheric pressure, and constant stirring.

The products in the gaseous aliquots (400 μL) were identified and measured using gas chromatography (GC Thermo CP-3800). The equipment operated with a methanizer at 350 °C, a thermal conductivity detector (TCD) at 200 °C, and a flame ionization detector (FID) at 150 °C. Argon was used as the carrier gas, along with a Carboxen column and a molecular sieve 13X. The liquid products were detected and quantified using ^{1}H nuclear magnetic resonance (NMR), 600 MHz, Ascend^{TM} 600 Brucker at 25 °C. 60 μL of a D_2O solution containing 0.21 mM of the reference 3-(trimethylsilyl)propionic-2,2,3,3-d_4 acid sodium salt (TSPd_4, 60 of D_2O solution) was added to 540 μL of the sample aliquots. A WET method was used to suppress the water peak and the MestReNova software was used to process the NMR data.

On a Varian E109 Model running at X-band (9.5 GHz) and room temperature, electron spin resonance (ESR) measurements were made. A quartz cell was utilized to contain the tested aqueous solutions and the spin trap consisting of 5,5-dimethyl-1-pyrroline N-oxide (DMPO, 177 mM in deionized water). After adding 5 mg as-synthesized BiOCl to 1 mL DMPO solution, 1 mL of the standard gas (20%mol CH_4 in argon) was introduced into the system. The addition of (i) xx 500 μL O_2; (ii) 500 uL 2mM $NaClO_2$ solution; and (iii) 500 μL 2mM $NaClO_2$ + HCl solution were also evaluated in independent experiments. A 100 W halogen lamp with an incident light intensity of approximately 100 mW cm^2 was used to illuminate the setup. The chili function of the EasySpin package was used to carry out the spectrum simulation and support the experimental data.

4.4. Results and discussion

4.4.1. Photocatalytic performance for partial CH_4 reforming

To compare the new achievements with our previous results [14], Bi_2O_3 was used for the preliminary test regarding the methanol production using a cycle-system based on chloride-intermediates. As seen in Table 1, chloride ion improved product formation in almost all cases. The reaction seems to be affected by the cation probably due to a co-catalyst effect (homogeneous) in photooxidation of CH_4 – this assumption is supported by the differences in C2 and C3 products' formation, which depend on subsequent carbon oxidation steps. A short analysis of these products indicate that methyl radicals are interacting with overoxidized C=O groups leading to ethanol (final interaction with H^+), acetic acid (with OH^-) or acetone (another methyl group), possibly

stochastically. However, a correlation with cation electronegativity is also possible since the cation with the least electronegativity (Na^+) lead to the poorest production rates due to its lowest electron affinity that interferes with the separation of the photogenerated charges. In other words, chloride ions can both participate in the methane halogenation (Eq. 4.1) and decrease the concentration of •OH species (Eq. 4.2) while simultaneously the cation ions can improve the separation of the photoinduced charges (Eq. 4.3), consequently, increasing the •OH generation. *M* represents the metal cation and *x* is its oxidation state. The chloromethane formation was confirmed by the detection of trace amounts of CH_3Cl through ^1H NMR (Fig. A4.1-A4.6), proving that chloromethane is an important intermediate in the formation of methanol and other chemicals from CH_4 oxidation.

$$x\mathrm{CH_4}_{(g)} + \mathrm{MCl}_{x(aq)} \rightarrow x\mathrm{CH_3Cl}_{(aq)} + \mathrm{M}^{x+}{}_{(aq)} + x\mathrm{H}^+{}_{(aq)} \quad (4.1)$$

$$\mathrm{Cl}^-{}_{(aq)} + \bullet\mathrm{OH}_{(aq)} \rightarrow \mathrm{HOCl}^-\bullet_{(aq)} \quad (4.2)$$

$$\mathrm{M}^{x+}{}_{(aq)} + \mathrm{e}^- \rightarrow \mathrm{M}^0{}_{(s)} \quad (4.3)$$

TABLE 4.1 - Production rate of liquid chemicals from the partial photooxidation of CH_4*.

Sample	Cation Electronegativity	Production rate (μmol g^{-1} h^{-1})			
		Methanol	Ethanol	Acetic acid	Acetone
Bi_2O_3 [14]	--	208	10	77	4
Bi_2O_3/NaCl	0.93	142	6	0	4
$Bi_2O_3/FeCl_3$**	1.83	231	13	2	4
$Bi_2O_3/CuCl_2$	1.90	580	67	406	124
$Bi_2O_3/CoCl_2$	2.55	621	134	151	109
$Bi_2O_3/SnCl_2$	1.96	581	24	211	117
$Bi_2O_3/ZnCl_2$	1.65	559	48	516	137

*Reaction conditions: 1 g L^{-1} Bi_2O_3 in 100 mL under visible-light illumination (108 W and ~5 mW cm^{-2}). The productions rates were determined after 4 h of reaction using a mixture of CH_4 in argon (20%mol CH_4).
**This condition was chosen to perform GC analyses as complementary analytical technique to confirm the product concentration (Fig. A4.7).

To understand how a structural chloride could participate in the reaction, photocatalytic performance was studied using BiOCl, which synthesis has been confirmed by XRD patterns (Fig. A4.8). The CH_4 oxidation reaction was analyzed in

aqueous solutions with no foreign ions, with O_2 bubbling, and addition of $NaClO_2$ or $NaClO_2$/HCl. As shown in Fig. 4.2, the main products obtained were methanol, ethanol, and acetic acid in all conditions except for the condition with HCl.

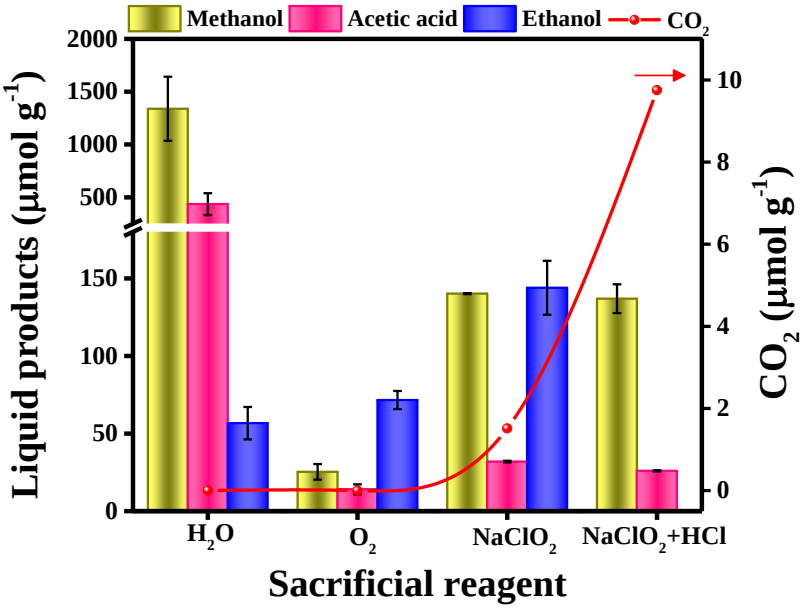

FIGURE 4.2 - Chemicals produced from methane photooxidation using different sacrificial reagents. The assays were performed using 100 mg BiOCl in 100 mL of the aqueous solution under visible-light. The reaction was carried out for 4 h using a mixture of CH_4 in argon (20%mol CH_4)

In general, the water condition had the highest conversion rate, producing around 1300 µmol g^{-1} of methanol, 57 µmol g^{-1} of ethanol, 435 µmol g^{-1} of acetic acid, and produced traces amounts of acetone. However, when oxygen was added as a sacrificial agent, BiOCl activity drastically decreased the production of methanol (25.3 µmol g^{-1}), ethanol (71.6 µmol g^{-1}), and acetic acid (14 µmol g^{-1}) compared to the water condition. Regarding the reduced production of liquid products, it could be associated with the interaction of the adsorbed O_2 with possible oxygen vacancies (OVs) present on the catalyst surface, and/or acting as a trapping agent for the chlorine ions, preventing the chloromethane reaction from proceeding [83]. Moreover, no CO and CO_2 were detected in all these conditions.

The addition of $NaClO_2$, a stable and non-toxic oxidizing agent, was expected to improve the methane activation and enhance the selectivity towards methanol production through chlorination catalytic reaction, avoiding CH_4 overoxidation. The

conversion to liquid products decreased when compared with H_2O conditions, but still was better than the oxygen condition. About 140 μmol g^{-1} of methanol, 32 μmol g^{-1} of acetic acid, and 144 μmol g^{-1} of ethanol have been observed. It should be noted that among all the conditions, $NaClO_2$ condition was the best for ethanol production. In addition, traces of CO and CO_2 (1.52 μmol g^{-1}) were observed. When HCl was added, the tendency continued with an increase in CO_2 production (9.75 μmol g^{-1}) and methanol and acetic acid production remained effective, while ethanol was not observed.

No changes were observed in the XRD patterns of the as-synthesized sample after the photocatalytic reaction (Fig. A4.8). In summary, BiOCl exhibits promising photocatalytic performance for methane conversion in the presence of sacrificial agents, but reaction conditions need to be carefully controlled to avoid the formation of CO and CO_2, which are undesired products. All the ^1H NMR are shown in the Appendix.

4.4.2. Characterization

XPS was used to investigate the chemical states of the as-synthesized BiOCl, Fig. 4.3. The high-resolution Bi 4f spectrum (Fig. 4.3a) can be deconvoluted into six peaks assigned to $Bi^{(3-x)+}$ (158.5 and 163.8 eV), Bi^{3+} (159.8 and 164.5 eV), and Bi^{5+} (159.8 and 165.7 eV) species in the sample. Additionally, the elemental composition calculated from the XPS peak areas of the Bi species on the surface was 31.33 % $Bi^{(3-x)+}$, 38.63% Bi^{3+}, and 30.04% of Bi^{5+}. The presence of other oxidation states of the metal may be beneficial in the oxidation of methane, since it would result in more empty d orbitals to accept electron donation from the C-H bond of methane, resulting in the reduction of the metal and consequently supporting in proton extraction. Then, based on the back-donation capacity of metals, the initial state of the metal is reconstituted, desorbing the intermediates formed and reconstituting the catalyst [84].

XPS spectra of O 1s (Fig. 4.3b) exhibited four peaks at 529.2, 529.7, 530.8, and 531.9 eV, corresponding to the O-Bi^{5+}, O-Bi^{3+}, oxygen vacancies (OVs), and surface adsorbed oxygen species, respectively. OVs are described in the literature as playing a crucial role in methane activation by facilitating the cleavage of C-H bonds. Moreover, these OVs could interact with metal sites in proximity, thereby promoting a metal redox cycle [21]. In addition, the Cl 2p spectra (Fig. 4.3c) could be deconvoluted into three peaks at 197.3, 198.8, and 200.1 eV, which are ascribed to the Cl $2p_{3/2}$ and Cl

$2p_{1/2}$ of interlayer Cl^-. Fig. A4.13 shows the XPS survey spectrum to confirm that the as-synthesized BiOCl presents no impurities

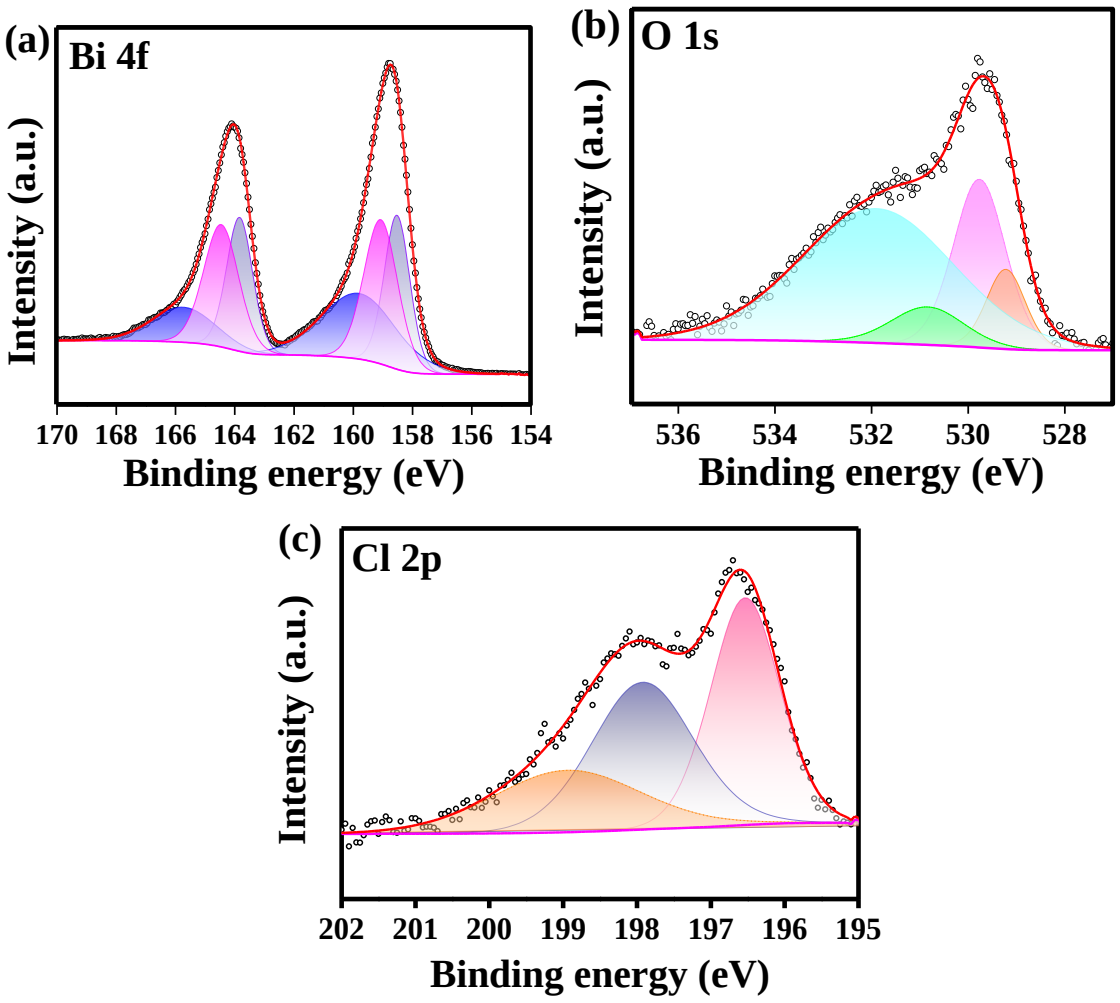

FIGURE 4.3 - XPS high-resolution spectra of (a) Bi 4f, (b) O 1s, and (c) Cl 2p of the as-synthesized BiOCl.

The STEM image, Fig. 4.4a, shows an irregular morphology shape composed by agglomerated nanometer particles of c.a. 15 nm. A *d*-spacing of 1.93 Å is seen in the HRTEM, Fig. 4.4b, which corresponds to the (2 0 0) plane of BiOCl. Additionally, the EDX measurements in Fig. 4.4c demonstrate the uniform distribution of Bi, O, and Cl, confirming once more that the sample presents no contaminations.

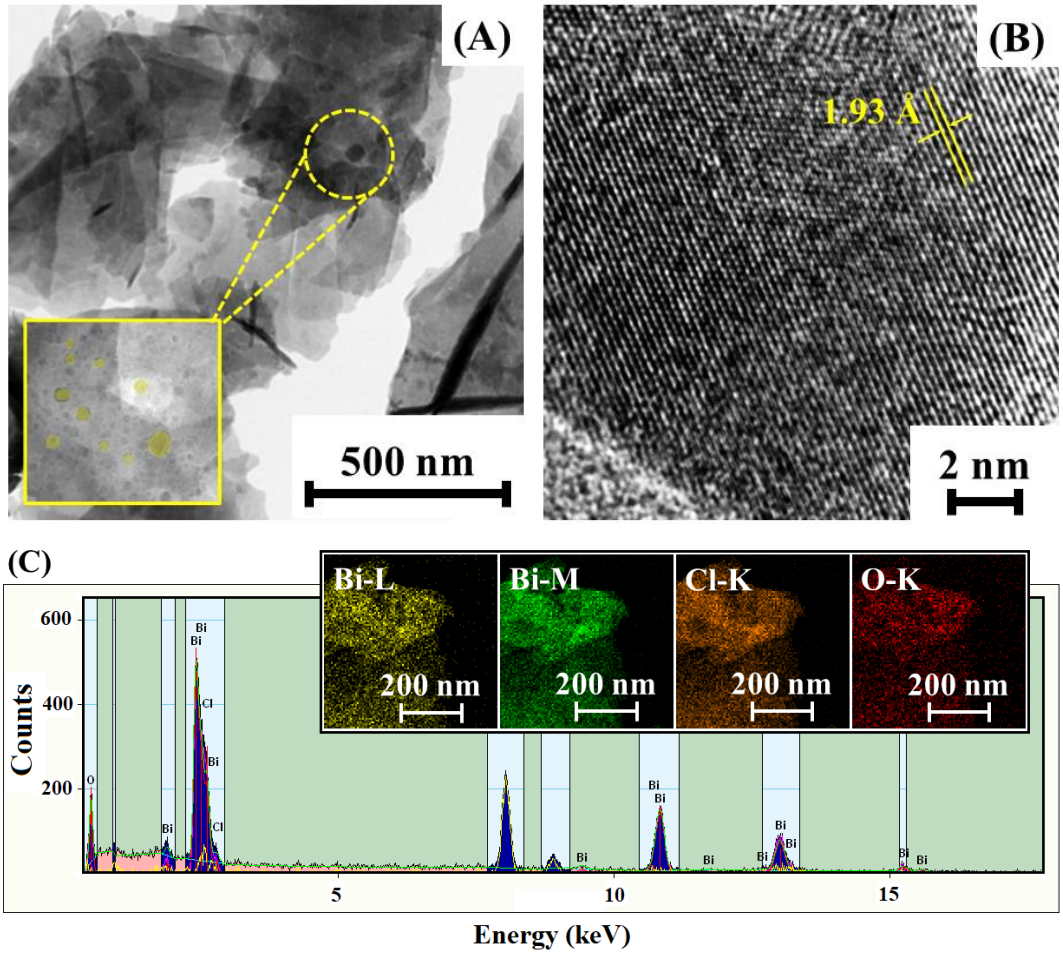

FIGURE 4.4 - (a) STEM bright-field image; (b) HRTEM micrography; and (c) EDX of the as-synthesized BiOCl. Colored regions only indicate different morphologies or element distribution.

4.4.3. Mechanism insights

To further investigate how sacrificial reagents act during photooxidation of methane, we conducted *in situ* ESR measurements with spin-trap DMPO, in the different conditions studied. Pure BiOCl, Fig. 4.5a, presents a well-controlled kinetics, producing methyl (•CH_3), hydroxyl (•OH) radicals and DMPO-$(OH)_2$ adduct in initial times. As we have shown in previous work, the DMPO-$(OH)_2$ adduct is only formed at high concentrations of •OH [14]. After 100 min under light irradiation (Fig. A4.14), there is no •CH_3 anymore, but hypochlorite radical (•OCl) was detected and all signal intensities for •OH and DMPO-$(OH)_2$ increased. The •OCl radical formation could be explained by chloride ions that are removed from the crystal structure of BiOCl, followed by the formation of the HOCl species through reaction with hydroxyl radicals (Eq. 4.4-4.6).

$$2Cl^-_{(aq)} + 2h^+ \rightarrow Cl_{2(g)} \quad (4.4)$$

$$Cl_{2(g)} + H_2O_{(l)} \rightarrow HOCl_{(aq)} + H^+_{(aq)} + Cl^-_{(aq)} \quad (4.5)$$

$$HOCl_{(aq)} + \bullet OH_{(aq)} \rightarrow \bullet OCl_{(aq)} + H_2O_{(l)} \quad (4.6)$$

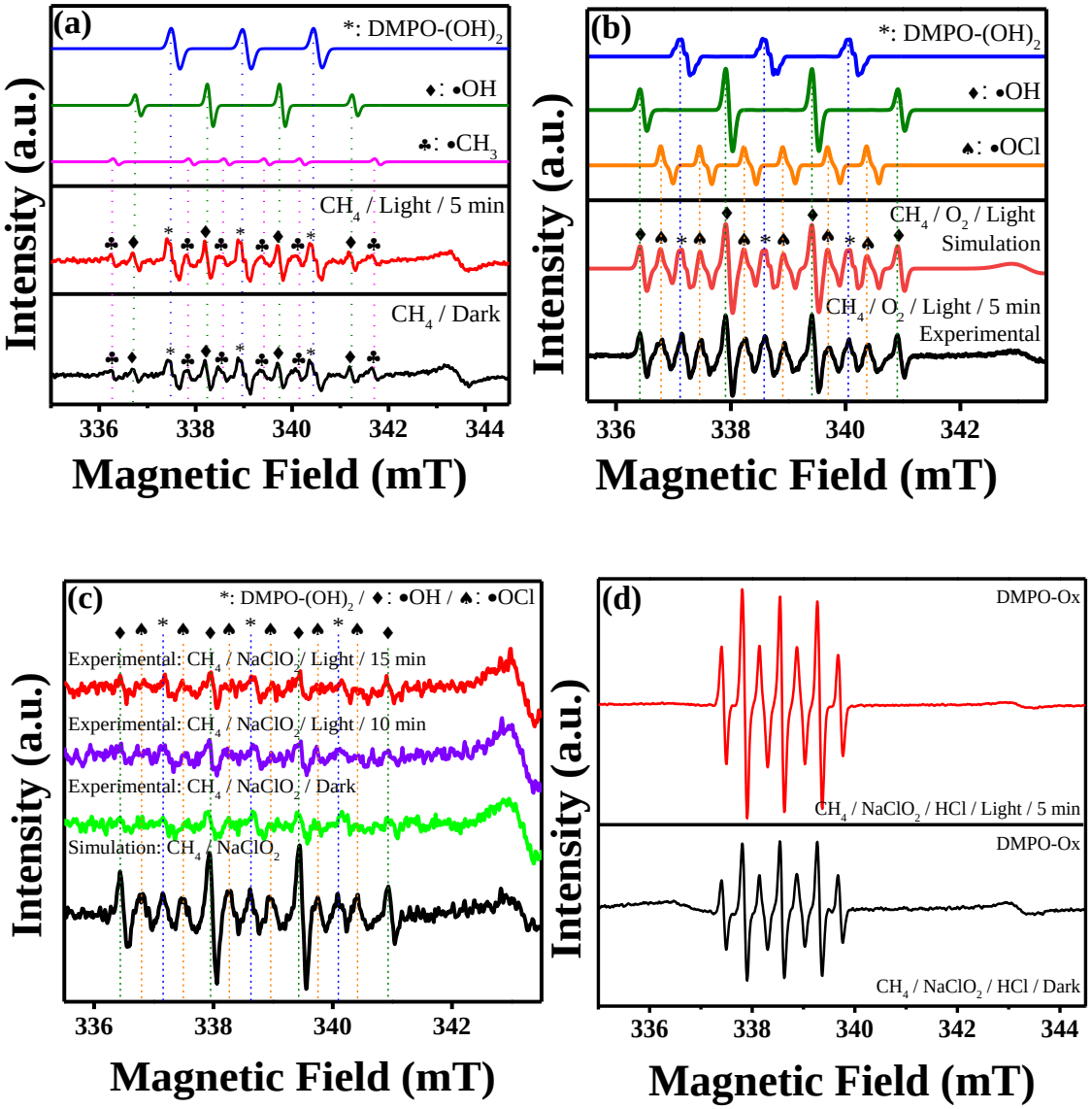

FIGURE 4.5 - ESR measurements of the DMPO solution containing: (a) pure BiOCl; (b) $BiOCl/O_2$; (c) $BiOCl/NaClO_2$; and (d) $BiOCl/NaClO_2/HCl$.

The Cl^- oxidation (E^0 (Cl^-/Cl_2) = +1.4 V *vs.* RHE), (Eq. 4.7-4.9) is more favorable than water oxidation (E^0 ($H_2O/\bullet OH$) = +2.3 V *vs.* RHE), being the oxidation process of the interlayer Cl^- (Eq. 4.9) even more likely since the density states close to

the maximum valence band of BiOCl is composed by Cl 3p orbitals as Cl has a lower electronegativity than O. Thus, the chloride ions can prevent the CH_4 overoxidation through hindering the formation of hydroxyl radical [73,81].

$$2Cl^-_{(aq)} + 2h^+ \rightarrow Cl_{2(g)} \qquad E^0 = +1.4 \text{ V } \textit{vs.} \text{ RHE} \qquad (4.7)$$

$$Cl^-_{(aq)} + h^+ \rightarrow \bullet Cl_{(aq)} \qquad E^0 = +2.5 \text{ V } \textit{vs.} \text{ RHE} \qquad (4.8)$$

$$2Cl^-_{(interlayer)} + 2h^+ \rightarrow Cl_{2(g)} \qquad E^0 = +0.5 \text{ V } \textit{vs.} \text{ RHE} \qquad (4.9)$$

Again, in the conditions with O_2 and $NaClO_2$ (Fig. 4.5b-c), •OH, •OCl radicals, and DMPO-$(OH)_2$ adduct were detected. However, the kinetics of radical formation with molecular oxygen was more intense since the radical signals were observed in the dark and increased throughout the reaction under light-irradiation. Surprisingly, in this condition, oxygen inhibited the photocatalytic efficiency of product formation. This inhibition is probably due to the reaction between oxygen and chloride ions released from the catalyst, leading to the formation of •OCl radicals in the early stages and hindering the involvement of oxygen in the methane photo-oxidation steps through the methyl radical scavenging to form CH_3O_2•. Moreover, oxygen can also react with oxygen vacancies present on the catalyst surface, preventing the activation of the methane molecule. It is widely known that oxygen species play a pivotal role not only in facilitating the metal's re-oxidation process but also in catalyzing the generation of diverse oxidation states.

On the other hand, $NaClO_2$ condition presents slower kinetics of radical formation. This slower kinetics is likely attributed to the higher chloride concentration in the medium before the reaction, which delays the leaching of chloride ions from the BiOCl layers and hinders the re-oxidation cycle of the catalyst's metallic center. Furthermore, this slower kinetics allows the formation of C_{2+} products as there is sufficient time for C-C coupling, leading to increased production of ethanol (Fig. 4.2). Finally, the $NaClO_2$/HCl condition leads to DMPO totally oxidized (DPMO-Ox) even in initial times, indicating that the medium was extremely oxidative, so methane is partially converted to CO_2. The oxidation kinetics of DMPO was very fast, preventing the detection of the radicals. However, possibly the mechanism may be similar to the condition with $NaClO_2$, since methane oxidation products were observed after the

reaction (Fig. 4.2). Meanwhile, as expected, superoxide radical ($O_2^{\bullet -}$) was not detected in any condition, because BiOCl does not exhibit sufficient band edge position to reduce O_2.

Based on the above results, the reaction control is promoted by the equilibrium reaction between the reduced Cl or •OCl radicals in solution and the regeneration of BiOCl structure, i.e., the reaction is limited by the interaction BiOCl – water. No foreign radicals are necessary, which shows that the reaction is sustainable in longer periods. Furthermore, the redox process of the center metal also plays an important role, as depicted in the Fig. 4.6.

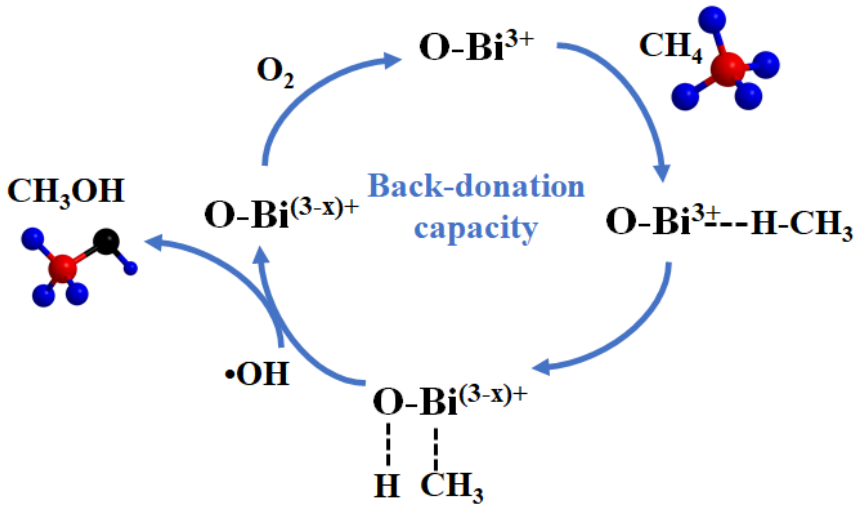

FIGURE 4.6 - Schematic illustration of role of self-oxidation/reduction of the center metal for the efficiency of the photocatalytic CH_4 oxidation.

4.5. Conclusion

We demonstrate that the chloromethane pathway for controlled methane oxidation is a feasible alternative to produce methanol. Cl-species quickly react with CH_4 to form CH_3Cl under light-illumination that by a simple substitution reaction with hydroxyl ions generate CH_3OH. Structural Cl^- in a perovskite layered material can be used in a cycle-based system to continuously oxidize methane to methanol without foreign radicals and keeping the stability of the photocatalyst. The self-redox process of the metal center also plays an important role for the CH_4 activation since the excess of electron in the metallic sites – resulted from the chlorine vacancies –, alter the charge distribution of each of the four closest neighbor bismuth atoms. The outcome is the self-

reduction of the lattice Bi, consequently supporting proton extraction. The initial state of the metal is reconstructed based on the back-donation capacity of metals.

5. CHAPTER V: GENERAL CONCLUSIONS

In this thesis, it was possibly understanding the key factors influencing photocatalysts' activities on controlled oxidation of methane to methanol, avoiding its complete oxidation to CO_2.

Bi_2O_3 demonstrated to be an efficient photocatalyst for the controlled oxidation of methane to methanol under visible-light and ambient conditions. The appropriate band edge position in Bi_2O_3 allowed the formation of hydroxyl radicals (•OH) in the valence band (VB), and prevented the formation of superoxide radicals ($O_2^{\bullet -}$) in the conduction band (CB). In this context, the availability of molecular oxygen (O_2) in the reaction medium is critical for the control of methane oxidation, as oxygen can capture methyl radicals ($\bullet CH_3$) that will in the future react with •OH to form methanol, avoiding the CH_4 overoxidation to CO_2. In addition, O_2 could also be reduced to hydrogen peroxide (H_2O_2). The presence of H_2O_2 in the reaction improved the photocatalytic activity due to the higher concentration of •OH, as well as increasing the dissolved oxygen in the medium.

An alternative pathway for the controlled oxidation of methane *via* chloromethane was also shown to be efficient for methanol production using BiOCl as photocatalyst. In this case, the reaction pathway proceeded by the formation of CH_3Cl as intermediate from the available Cl ions in the solution or by the controlled availability of the chloride ions present in the crystalline structure of the material, e.g., BiOCl. Evidences were provided *via* ESR analysis that Bi_2O_3 and BiOCl easily produce hydroxyl radicals and have a high interaction with the methane molecule, facilitating its activation even under the light-free conditions.

Therefore, in this thesis, two distinct pathways were successfully applied to promote the controlled oxidation of CH_4 to CH_3OH, rather than the complete, uncontrolled oxidation to CO_2: (i) using semiconductors that have an unfavorable conduction band for the formation of superoxide radicals, thus allowing oxygen to be viable in the reaction, and (ii) in the presence of chloride intermediates, which in both cases subsequently react with hydroxyl radicals to form methanol.

6. REFERENCES

[1] J. Xie, R. Jin, A. Li, Y. Bi, Q. Ruan, Y. Deng, Y. Zhang, S. Yao, Highly selective oxidation of methane to methanol at ambient conditions by titanium dioxide supported iron species, Nat. Catal. 1 (2018) 889–896. https://doi.org/10.1038/s41929-018-0170-x.

[2] J. Yang, J.Y. Hao, J.P. Wei, J. Dai, Y. Li, Visible-light-driven selective oxidation of methane to methanol on amorphous FeOOH coupled m-WO_3, Fuel. 266 (2020). https://doi.org/10.1016/j.fuel.2020.117104.

[3] L. Arnarson, P.S. Schmidt, M. Pandey, A. Bagger, K.S. Thygesen, I.E.L. Stephens, J. Rossmeisl, Fundamental limitation of electrocatalytic methane conversion to methanol, Phys. Chem. Chem. Phys. 20 (2018) 11152–11159. https://doi.org/10.1039/c8cp01476k.

[4] C. Williams, J.H. Carter, N.F. Dummer, Y.K. Chow, D.J. Morgan, S. Yacob, P. Serna, D.J. Willock, R.J. Meyer, S.H. Taylor, G.J. Hutchings, Selective Oxidation of Methane to Methanol Using Supported AuPd Catalysts Prepared by Stabilizer-Free Sol-Immobilization, Acs Catal. 8 (2018) 2567–2576. https://doi.org/10.1021/acscatal.7b04417.

[5] M. Ma, B.J. Jin, P. Li, M.S. Jung, J.I. Kim, Y. Cho, S. Kim, J.H. Moon, J.H. Park, Ultrahigh Electrocatalytic Conversion of Methane at Room Temperature, Adv. Sci. 4 (2017). https://doi.org/10.1002/advs.201700379.

[6] W. Li, D. He, G. Hu, X. Li, G. Banerjee, J. Li, S.H. Lee, Q. Dong, T. Gao, G.W. Brudvig, M.M. Waegele, D.E. Jiang, D. Wang, Selective CO Production by Photoelectrochemical Methane Oxidation on TiO_2, ACS Cent. Sci. 4 (2018) 631–637. https://doi.org/10.1021/acscentsci.8b00130.

[7] Y. Kadosh, E. Korin, A. Bettelheim, Room-temperature conversion of the photoelectrochemical oxidation of methane into electricity at nanostructured TiO_2, Sustain. Energy Fuels. 5 (2021) 127–134. https://doi.org/10.1039/d0se00984a.

[8] J. Liu, J.H. Ji, Y.H. Zhang, Z.M. Bai, Z.A. Huang, Y.K. Gao, X.T. Wang, Photoelectrocatalytic Oxidation of Methane Into Methanol Over $BiVO_4$/AU/FeCo-LDH Catalysts, Nano. 17 (2022). https://doi.org/10.1142/s179329202250028x.

[9] J. Liu, Y.H. Zhang, Z.M. Bai, Z.A. Huang, Y.K. Gao, Photoelectrocatalytic oxidation of methane into methanol and formic acid over ZnO/graphene/polyaniline catalyst, Chinese Phys. B. 28 (2019). https://doi.org/10.1088/1674-1056/28/4/048101.

[10] F. Arnano, A. Shintani, K. Tsurui, H. Mukohara, T. Ohno, S. Takenaka, Photoelectrochemical Homocoupling of Methane under Blue Light Irradiation, Acs Energy Lett. 4 (2019) 502–507. https://doi.org/10.1021/acsenergylett.8b02436.

[11] J. Ma, K.K. Mao, J.X. Low, Z.H. Wang, D.W. Xi, W.Q. Zhang, H.X. Ju, Z.M. Qi, R. Long, X.J. Wu, L. Song, Y.J. Xiong, Efficient Photoelectrochemical Conversion of Methane into Ethylene Glycol by WO_3 Nanobar Arrays, Angew.

Chemie-International Ed. 60 (2021) 9357–9361. https://doi.org/10.1002/anie.202101701.

[12] P. Kumar, T.A. Al-Attas, J.G. Hu, M.G. Kibria, Single Atom Catalysts for Selective Methane Oxidation to Oxygenates, ACS Nano. 16 (2022) 8557–8618. https://doi.org/10.1021/acsnano.2c02464.

[13] S. Murcia-Lopez, K. Villa, T. Andreu, J.R. Morante, Improved selectivity for partial oxidation of methane to methanol in the presence of nitrite ions and $BiVO_4$ photocatalyst, Chem. Commun. 51 (2015) 7249–7252. https://doi.org/10.1039/c5cc00978b.

[14] J.A. de Oliveira, J.C. da Cruz, O.R. Nascimento, C. Ribeiro, Selective CH_4 reform to methanol through partial oxidation over Bi_2O_3 at room temperature and pressure, Appl. Catal. B-Environmental. 318 (2022). https://doi.org/10.1016/j.apcatb.2022.121827.

[15] N. Agarwal, S.J. Freakley, R.U. McVicker, S.M. Althahban, N. Dimitratos, Q. He, D.J. Morgan, R.L. Jenkins, D.J. Willock, S.H. Taylor, C.J. Kiely, G.J. Hutchings, Aqueous Au-Pd colloids catalyze selective CH_4 oxidation to CH_3OH with O_2 under mild conditions, Science (80-.). 358 (2017) 223–226. https://doi.org/10.1126/science.aan6515.

[16] K.W. Frese, PARTIAL ELECTROCHEMICAL OXIDATION OF METHANE UNDER MILD CONDITIONS, Langmuir. 7 (1991) 13–15. https://doi.org/10.1021/la00049a004.

[17] H. Song, X. Meng, S. Wang, W. Zhou, X. Wang, T. Kako, J. Ye, Direct and Selective Photocatalytic Oxidation of CH_4 to Oxygenates with O_2 on Cocatalysts/ZnO at Room Temperature in Water, J. Am. Chem. Soc. 141 (2019) 20507–20515. https://doi.org/10.1021/jacs.9b11440.

[18] M.D. Krcha, A.D. Mayernick, M.J. Janik, Periodic trends of oxygen vacancy formation and C-H bond activation over transition metal-doped CeO_2 (111) surfaces, J. Catal. 293 (2012) 103–115. https://doi.org/10.1016/j.jcat.2012.06.010.

[19] Y. Chen, F. Wang, Z. Huang, J. Chen, C. Han, Q. Li, Y. Cao, Y. Zhou, Dual-Function Reaction Center for Simultaneous Activation of CH_4 and O_2 via Oxygen Vacancies during Direct Selective Oxidation of CH_4 into CH_3OH, ACS Appl. Mater. Interfaces. 13 (2021) 46694–46702. https://doi.org/10.1021/acsami.1c13661.

[20] Z. Cheng, L. Qin, M.Q. Guo, J.A. Fan, D.K. Xu, L.S. Fan, Methane adsorption and dissociation on iron oxide oxygen carriers: the role of oxygen vacancies, Phys. Chem. Chem. Phys. 18 (2016) 16423–16435. https://doi.org/10.1039/c6cp01287f.

[21] Y.B. Jin, J.T. Long, X. Ma, T.H. Zhou, Z.Z. Zhang, H.X. Lin, J.L. Long, X.X. Wang, Synthesis of caged iodine-modified ZnO nanomaterials and study on their visible light photocatalytic antibacterial properties, Appl. Catal. B-Environmental. 256 (2019). https://doi.org/10.1016/j.apcatb.2019.117873.

[22] Z.X. Yang, J.Q. Wang, J.T. Wang, M. Li, Q. Cheng, Z.Z. Wang, X.T. Wang, J.M. Li, Y. Li, G.K. Zhang, 2D WO_{3-x} Nanosheet with Rich Oxygen Vacancies

for Efficient Visible-Light-Driven Photocatalytic Nitrogen Fixation, Langmuir. 38 (2022) 1178–1187. https://doi.org/10.1021/acs.langmuir.1c02862.

[23] H.W. Zhang, Q.Y. Liu, Y.F. Chen, L. Pei, L. Bao, Y.J. Yuan, Mixed-Valent Cobalt-Modulated Tungsten Trioxide Nanorod Arrays for Improved Photocatalytic N_2 Fixation, J. Phys. Chem. C. 125 (2021) 21997–22005. https://doi.org/10.1021/acs.jpcc.1c06832.

[24] Y.X. Zhao, Y.F. Zhao, R. Shi, B. Wang, G.I.N. Waterhouse, L.Z. Wu, C.H. Tung, T.R. Zhang, Tuning Oxygen Vacancies in Ultrathin TiO_2 Nanosheets to Boost Photocatalytic Nitrogen Fixation up to 700 nm, Adv. Mater. 31 (2019). https://doi.org/10.1002/adma.201806482.

[25] X. Yu, V. De Waele, A. Lofberg, V. Ordomsky, A.Y. Khodakov, Selective photocatalytic conversion of methane into carbon monoxide over zinc-heteropolyacid-titania nanocomposites, Nat. Commun. 10 (2019). https://doi.org/10.1038/s41467-019-08525-2.

[26] N. Zhang, X.Y. Li, H.C. Ye, S.M. Chen, H.X. Ju, D.B. Liu, Y. Lin, W. Ye, C.M. Wang, Q. Xu, J.F. Zhu, L. Song, J. Jiang, Y.J. Xiong, Oxide Defect Engineering Enables to Couple Solar Energy into Oxygen Activation, J. Am. Chem. Soc. 138 (2016) 8928–8935. https://doi.org/10.1021/jacs.6b04629.

[27] A. Mehmood, S.Y. Chae, E.D. Park, Photoelectrochemical Conversion of Methane into Value-Added Products, Catalysts. 11 (2021). https://doi.org/10.3390/catal11111387.

[28] S.L. Wei, X.L. Zhu, P.Y. Zhang, Y.Y. Fan, Z.H. Sun, X. Zhao, D.X. Han, L. Niu, Aerobic oxidation of methane to formaldehyde mediated by crystal-O over gold modified tungsten trioxide via photocatalysis, Appl. Catal. B-Environmental. 283 (2021). https://doi.org/10.1016/j.apcatb.2020.119661.

[29] Y. Kadosh, E. Korin, A. Bettelheim, Room-temperature conversion of the photoelectrochemical oxidation of methane into electricity at nanostructured TiO_2, Sustain. Energy Fuels. 5 (2021) 127–134. https://doi.org/10.1039/d0se00984a.

[30] S. Shoji, X.B. Peng, A. Yamaguchi, R. Watanabe, C. Fukuhara, Y. Cho, T. Yamamoto, S. Matsumura, M.W. Yu, S. Ishii, T. Fujita, H. Abe, M. Miyauchi, Photocatalytic uphill conversion of natural gas beyond the limitation of thermal reaction systems, Nat. Catal. 3 (2020) 148–153. https://doi.org/10.1038/s41929-019-0419-z.

[31] X. Meng, X. Cui, N.P. Rajan, L. Yu, D. Deng, X. Bao, Direct Methane Conversion under Mild Condition by Thermo-, Electro-, or Photocatalysis, Chem. (2019) 1–30. https://doi.org/10.1016/j.chempr.2019.05.008.

[32] A. Heller, Chemistry and Applications of Photocatalytic Oxidation of Thin Organic Films, Acc. Chem. Res. 28 (1995) 503–508. https://doi.org/10.1021/ar00060a006.

[33] Y. Fan, W. Zhou, X. Qiu, H. Li, Y. Jiang, Z. Sun, D. Han, L. Niu, Z. Tang, Selective photocatalytic oxidation of methane by quantum-sized bismuth vanadate, Nat. Sustain. (2021). https://doi.org/10.1038/s41893-021-00682-x.

[34] W. Zhou, X. Qiu, Y. Jiang, Y. Fan, S. Wei, D. Han, L. Niu, Z. Tang, Highly selective aerobic oxidation of methane to methanol over gold decorated zinc oxide: Via photocatalysis, J. Mater. Chem. A. 8 (2020) 13277–13284. https://doi.org/10.1039/d0ta02793f.

[35] W.L. Zhu, M.K. Shen, G.Z. Fan, A. Yang, J.R. Meyer, Y.N. Ou, B. Yin, J. Fortner, M. Foston, Z.S. Li, Z.G. Zou, B. Sadtler, Facet-Dependent Enhancement in the Activity of Bismuth Vanadate Microcrystals for the Photocatalytic Conversion of Methane to Methanol, Acs Appl. Nano Mater. 1 (2018) 6683–6691. https://doi.org/10.1021/acsanm.8b01490.

[36] L. Zhou, W.Z. Wang, H.L. Xu, S.M. Sun, M. Shang, Bi_2O_3 Hierarchical Nanostructures: Controllable Synthesis, Growth Mechanism, and their Application in Photocatalysis, Chem. Eur. J. 15 (2009) 1776–1782. https://doi.org/10.1002/chem.200801234.

[37] D.L. Wood, J. Tauc, WEAK ABSORPTION TAILS IN AMORPHOUS SEMICONDUCTORS, Phys. Rev. B. 5 (1972) 3144-. https://doi.org/10.1103/PhysRevB.5.3144.

[38] J.A. Oliveira, R.M.R. Silva, T.S.T. da Silva Gelson, J.A. Torres, A. Vali, C. Ribeiro, K. Rajeshwar, A.M.R. Lu$\blacklozenge$s, Copper Vanadates: Targeted Synthesis of Two Pure Phases and Use in a Photoanode/Cathode Setup for Selective Photoelectrochemical Conversion of Carbon Dioxide to Liquid Fuel, Mater. Res. Bull. (2021) 111716.

[39] X.Y. Yang, A. Wolcott, G.M. Wang, A. Sobo, R.C. Fitzmorris, F. Qian, J.Z. Zhang, Y. Li, Nitrogen-Doped ZnO Nanowire Arrays for Photoelectrochemical Water Splitting, Nano Lett. 9 (2009) 2331–2336. https://doi.org/10.1021/nl900772q.

[40] K. Gelderman, L. Lee, S.W. Donne, Flat-band potential of a semiconductor: using the Mott-Schottky equation, J. Chem. Educ. 84 (2007) 685–688. https://doi.org/10.1021/ed084p685.

[41] Z. Grubac, J. Katic, M. Metikos-Hukovic, Energy-Band Structure as Basis for Semiconductor n-Bi_2S_3/n-Bi_2O_3 Photocatalyst Design, J. Electrochem. Soc. 166 (2019) H433–H437. https://doi.org/10.1149/2.0481910jes.

[42] K. Rajeshwar, Fundamentals of semiconductor electrochemistry and photoelectrochemistry, Encycl. Electrochem. 6 (2007) 1–53.

[43] K. Villa, S. Murcia-Lopez, T. Andreu, J.R. Morante, Mesoporous WO_3 photocatalyst for the partial oxidation of methane to methanol using electron scavengers, Appl. Catal. B-Environmental. 163 (2015) 150–155. https://doi.org/10.1016/j.apcatb.2014.07.055.

[44] C.G. Hatchard, C.A. Parker, A new sensitive chemical actinometer - II. Potassium ferrioxalate as a standard chemical actinometer, Proc. R. Soc. London. Ser. A. Math. Phys. Sci. 235 (1956) 518–536. https://doi.org/10.1098/rspa.1956.0102.

[45] O.F. Lopes, E.C. Paris, C. Ribeiro, Synthesis of Nb_2O_5 nanoparticles through the oxidant peroxide method applied to organic pollutant photodegradation: A mechanistic study, Appl. Catal. B-Environmental. 144 (2014) 800–808.

https://doi.org/10.1016/j.apcatb.2013.08.031.

[46] S. Stoll, A. Schweiger, EasySpin, a comprehensive software package for spectral simulation and analysis in EPR, J. Magn. Reson. 178 (2006) 42–55. https://doi.org/10.1016/j.jmr.2005.08.013.

[47] M.Y. Wang, S.Y. Qiu, H.Y. Yang, Y.X. Huang, L. Dai, B.L. Zhang, J. Zou, Spectrophotometric determination of hydrogen peroxide in water with peroxidase-catalyzed oxidation of potassium iodide and its applications to hydroxylamine-involved Fenton and Fenton-like systems, Chemosphere. 270 (2021). https://doi.org/10.1016/j.chemosphere.2020.129448.

[48] N.I. Medvedeva, V.P. Zhukov, V.A. Gubanov, D.L. Novikov, B.M. Klein, Electronic structure and chemical bonding in delta-Bi_2O_3, J. Phys. Chem. Solids. 57 (1996) 1243–1250. https://doi.org/10.1016/0022-3697(95)00311-8.

[49] Q.Y. Li, Z.Y. Zhao, Interfacial properties of alpha/beta-Bi_2O_3 homo-junction from first-principles calculations, Phys. Lett. A. 379 (2015) 2766–2771. https://doi.org/10.1016/j.physleta.2015.08.002.

[50] J.G. Hou, C. Yang, Z. Wang, W.L. Zhou, S.Q. Jiao, H.M. Zhu, In situ synthesis of alpha-beta phase heterojunction on Bi_2O_3 nanowires with exceptional visible-light photocatalytic performance, Appl. Catal. B-Environmental. 142 (2013) 504–511. https://doi.org/10.1016/j.apcatb.2013.05.050.

[51] J. Zhang, Q. Xu, Z. Feng, M. Li, C. Li, Importance of the relationship between surface phases and photocatalytic activity of TiO_2, Angew. Chemie-International Ed. 47 (2008) 1766–1769. https://doi.org/10.1002/anie.200704788.

[52] Y.C. Wan, H.J. Zhou, M.Y. Zheng, Z.H. Huang, F.Y. Kang, J. Li, R.T. Lv, Oxidation State Modulation of Bismuth for Efficient Electrocatalytic Nitrogen Reduction to Ammonia, Adv. Funct. Mater. 31 (2021). https://doi.org/10.1002/adfm.202100300.

[53] S.W. Gong, G.Q. Zhu, R. Wang, F. Rao, X.J. Shi, J.Z. Gao, Y. Huang, C.Z. He, M. Hojamberdiev, Synergistically boosting highly selective CO_2-to-CO photoreduction over BiOCl nanosheets via in-situ formation of surface defects and non-precious metal nanoparticles, Appl. Catal. B-Environmental. 297 (2021). https://doi.org/10.1016/j.apcatb.2021.120413.

[54] Y. Shi, J. Li, C. Mao, S. Liu, X. Wang, X. Liu, S. Zhao, X. Liu, Y. Huang, L. Zhang, Van Der Waals gap-rich BiOCl atomic layers realizing efficient, pure-water CO_2-to-CO photocatalysis, Nat. Commun. 12 (2021) 1–10. https://doi.org/10.1038/s41467-021-26219-6.

[55] L.X. Yang, J.W. Guo, J. Zhang, S.Q. Zhang, W.L. Dai, X. Xiao, X.B. Luo, S.L. Luo, Utter degradation of toluene with inhibiting the generation of benzene by self-supporting Bi_2MoO_6 nanoflakes featuring OV-enriched interface, Chem. Eng. J. 427 (2022). https://doi.org/10.1016/j.cej.2021.131550.

[56] Y. Huang, W. Wang, Q. Zhang, J.J. Cao, R.J. Huang, W.K. Ho, S.C. Lee, In situ Fabrication of alpha-Bi_2O_3/$(BiO)_{(2)}CO_3$ Nanoplate Heterojunctions with Tunable Optical Property and Photocatalytic Activity, Sci. Rep. 6 (2016). https://doi.org/10.1038/srep23435.

[57] Y.C. Wu, Y.T. Huang, H.Y. Yang, Crystallization mechanism and photocatalytic performance of vanadium-modified bismuth oxide through precipitation processes at room temperature, Crystengcomm. 18 (2016) 6881–6888. https://doi.org/10.1039/c6ce00954a.

[58] C.M. Jiang, G. Segev, L.H. Hess, G.J. Liu, G. Zaborski, F.M. Toma, J.K. Cooper, I.D. Sharp, Composition-Dependent Functionality of Copper Vanadate Photoanodes, ACS Appl. Mater. Interfaces. 10 (2018) 10627–10633. https://doi.org/10.1021/acsami.8b02977.

[59] J. Cheng, M. Zhang, G. Wu, X. Wang, J. Zhou, K. Cen, Optimizing CO_2 reduction conditions to increase carbon atom conversion using a Pt-RGO|| Pt-TNT photoelectrochemical cell, Sol. Energy Mater. Sol. Cells. 132 (2015) 606–614.

[60] A.G. Song, A. Chemseddine, I.Y. Ahmet, P. Bogdanoff, D. Friedrich, F.F. Abdi, S.P. Berglund, R. van de Krol, Evaluation of copper vanadate (beta-$Cu_2V_2O_7$) as a photoanode material for photoelectrochemical water oxidation, Chem. Mater. 32 (2020) 2408–2419. https://doi.org/10.1021/acs.chemmater.9b04909.

[61] Y. Li, X.Y. Wu, J. Li, K. Wang, G.K. Zhang, Z-scheme g-C_3N_4@CsxWO$_3$ heterostructure as smart window coating for UV isolating, Vis penetrating, NIR shielding and full spectrum photocatalytic decomposing VOCs, Appl. Catal. B-Environmental. 229 (2018) 218–226. https://doi.org/10.1016/j.apcatb.2018.02.024.

[62] M. Gilbert, B. Albinsson, Photoinduced charge and energy transfer in molecular wires, Chem. Soc. Rev. 44 (2015) 845–862. https://doi.org/10.1039/c4cs00221k.

[63] S.L. Liu, J.L. Chen, D.F. Xu, X.C. Zhang, M.Y. Shen, Enhanced photocatalytic activity of direct Z-scheme Bi_2O_3/g-C_3N_4 composites via facile one-step fabrication, J. Mater. Res. 33 (2018) 1391–1400. https://doi.org/10.1557/jmr.2018.67.

[64] M.L. Sun, Q.H. Zhao, C.F. Du, Z.L. Liu, Enhanced visible light photocatalytic activity in BiOCl/SnO_2: heterojunction of two wide band-gap semiconductors, Rsc Adv. 5 (2015) 22740–22752. https://doi.org/10.1039/c4ra14187c.

[65] P.S. Li, Z. Zhou, Q. Wang, M. Guo, S.W. Chen, J.X. Low, R. Long, W. Liu, P.R. Ding, Y.Y. Wu, Y.J. Xiong, Visible-Light-Driven Nitrogen Fixation Catalyzed by Bi_5O_7Br Nanostructures: Enhanced Performance by Oxygen Vacancies, J. Am. Chem. Soc. 142 (2020) 12430–12439. https://doi.org/10.1021/jacs.0c05097.

[66] P.P. Luo, X.K. Zhou, Y. Li, T.B. Lu, Simultaneously Accelerating Carrier Transfer and Enhancing O-$_2$/CH_4 Activation via Tailoring the Oxygen-Vacancy-Rich Surface Layer for Cocatalyst-Free Selective Photocatalytic CH_4 Conversion, ACS Appl. Mater. Interfaces. 14 (2022) 21069–21078. https://doi.org/10.1021/acsami.2c03671.

[67] M. Shah, C. Oh, H. Park, Y.J. Hwang, M. Ma, J.H. Park, Catalytic Oxidation of Methane to Oxygenated Products: Recent Advancements and Prospects for Electrocatalytic and Photocatalytic Conversion at Low Temperatures, Adv. Sci. 7 (2020). https://doi.org/10.1002/advs.202001946.

[68] K. Ogura, M. Kataoka, Photochemical conversion of methane, J. Mol. Catal. 43

(1988) 371–379. https://doi.org/10.1016/0304-5102(88)85148-4.

[69] W.C. Zhou, X.Y. Qiu, Y.H. Jiang, Y.Y. Fan, S.L. Wei, D.X. Han, L. Niu, Z.Y. Tang, Highly selective aerobic oxidation of methane to methanol over gold decorated zinc oxide via photocatalysis, J. Mater. Chem. A. 8 (2020) 13277–13284. https://doi.org/10.1039/d0ta02793f.

[70] J. Shan, M. Li, L.F. Allard, S. Lee, M. Flytzani-Stephanopoulos, Mild oxidation of methane to methanol or acetic acid on supported isolated rhodium catalysts, Nature. 551 (2017) 605–608. https://doi.org/10.1038/nature24640.

[71] X. Yu, V.L. Zholobenko, S. Moldovan, D. Hu, D. Wu, V. V Ordomsky, A.Y. Khodakov, Stoichiometric methane conversion to ethane using photochemical looping at ambient temperature, Nat. Energy. 5 (2020) 511–519. https://doi.org/10.1038/s41560-020-0616-7.

[72] I. Grcic, J. Marcec, L. Radetic, A.M. Radovan, I. Melnjak, I. Jajcinovic, I. Brnardic, Ammonia and methane oxidation on $TiO_{(2)}$supported on glass fiber mesh under artificial solar irradiation, Environ. Sci. Pollut. Res. 28 (2021) 18354–18367. https://doi.org/10.1007/s11356-020-09561-y.

[73] D.M. Li, J.N. Shen, J.J. Zhang, Y. Chai, Y.Y. Xie, C.W. Qiu, M.M. Ni, Y.H. Zheng, X.X. Wang, Z.Z. Zhang, Photocatalytic Chlorination of Methane Using Alkali Chloride Solution, Acs Catal. 12 (2022) 7004–7013. https://doi.org/10.1021/acscatal.2c01228.

[74] J.M. Dumas, C. Geron, A.R. Kribii, M. Lakraimi, Etude structurale et thermodynamique des interactions entre des d�riv�s chlor�s et brom�s du m�thane et des amides tertiaires, Can. J. Chem. 62 (1984) 2634–2640.

[75] V. Paunovic, J. Perez-Ramirez, Catalytic halogenation of methane: a dream reaction with practical scope?, Catal. Sci. Technol. 9 (2019) 4515–4530. https://doi.org/10.1039/c9cy00625g.

[76] K. Ogura, K. Takamagari, DIRECT CONVERSION OF METHANE TO METHANOL, CHLOROMETHANE AND DICHLOROMETHANE AT ROOM-TEMPERATURE, Nature. 319 (1986) 308. https://doi.org/10.1038/319308a0.

[77] A. Prajapati, R. Sartape, N.C. Kani, J.A. Gauthier, M.R. Singh, Chloride-Promoted High-Rate Ambient Electrooxidation of Methane to Methanol on Patterned Cu-Ti Bimetallic Oxides, Acs Catal. 12 (2022) 14321–14329. https://doi.org/10.1021/acscatal.2c03619.

[78] J. Ma, C. Zhu, K. Mao, W. Jiang, J. Low, D. Duan, H. Ju, D. Liu, K. Wang, Y. Zang, Sustainable methane utilization technology via photocatalytic halogenation with alkali halides, Nat. Commun. 14 (2023) 1410.

[79] G.A. Olah, B. Gupta, M. Farina, J.D. Felberg, W.M. Ip, A. Husain, R. Karpeles, K. Lammertsma, A.K. Melhotra, N.J. Trivedi, ELECTROPHILIC REACTIONS AT SINGLE BONDS .20. SELECTIVE MONOHALOGENATION OF METHANE OVER SUPPORTED ACID OR PLATINUM METAL-CATALYSTS AND HYDROLYSIS OF METHYL HALIDES OVER GAMMA-ALUMINA-SUPPORTED METAL-OXIDE HYDROXIDE CATALYSTS - A FEASIBLE PATH FOR THE OXID, J. Am. Chem. Soc. 107 (1985) 7097–7105.

https://doi.org/10.1021/ja00310a057.

[80] H.P. Wang, Z.K. Han, Y.Y. Zhou, X.C. Liu, D. Zeng, W.M. Wang, D. Sarker, L. Zhang, W.Z. Wang, Efficient photocatalytic chlorine production on bismuth oxychloride in chloride solution, Appl. Catal. B-Environmental. 297 (2021). https://doi.org/10.1016/j.apcatb.2021.120436.

[81] Y. Shiraishi, M. Hashimoto, K. Chishiro, K. Moriyama, S. Tanaka, T. Hirai, Photocatalytic Dinitrogen Fixation with Water on Bismuth Oxychloride in Chloride Solutions for Solar-to-Chemical Energy Conversion, J. Am. Chem. Soc. 142 (2020) 7574–7583. https://doi.org/10.1021/jacs.0c01683.

[82] K. Xu, L. Wang, H.F. Feng, Z.F. Xu, J.C. Zhuang, Y. Du, F. Pan, W.C. Hao, Theoretical insights into nitrogen oxide activation on halogen defect-rich {001} facets of bismuth oxyhalide, J. Mater. Sci. Technol. 77 (2021) 217–222. https://doi.org/10.1016/j.jmst.2020.10.008.

[83] Q.H. Xie, H.M. Zhang, J.C. Kang, J. Cheng, Q.H. Zhang, Y. Wang, Oxidative Dehydrogenation of Propane to Propylene in the Presence of HCI Catalyzed by CeO_2 and NiO-Modified CeO_2 Nanocrystals, Acs Catal. 8 (2018) 4902–4916. https://doi.org/10.1021/acscatal.8b00650.

[84] V. Fung, G.X. Hu, F. Tao, D.E. Jiang, Methane Chemisorption on Oxide-Supported Pt Single Atom, Chemphyschem. 20 (2019) 2217–2220. https://doi.org/10.1002/cphc.201900497.

[85] M. Wise, A. Chapoy, R. Burgass, Solubility Measurement and Modeling of Methane in Methanol and Ethanol Aqueous Solutions, J. Chem. Eng. Data. 61 (2016) 3200–3207. https://doi.org/10.1021/acs.jced.6b00296.

[86] X.H. Chen, S.B. Li, Photooxidation of methane to methanol by molecular oxygen on water-preadsorbed porous TiO_2-based catalysts, Chem. Lett. (2000) 314–315. https://doi.org/10.1246/cl.2000.314.

[87] M.A. Gondal, A. Hameed, Z.H. Yamani, A. Arfaj, Photocatalytic transformation of methane into methanol under UV laser irradiation over WO_3, TiO_2 and NiO catalysts, Chem. Phys. Lett. 392 (2004) 372–377. https://doi.org/10.1016/j.cplett.2004.05.092.

[88] Y. Hu, S. Higashimoto, S. Takahashi, Y. Nagai, M. Anpo, Selective photooxidation of methane into methanol by nitric oxide over V-MCM-41 mesoporous molecular sieves, Catal. Letters. 100 (2005) 35–37. https://doi.org/10.1007/s10562-004-3082-0.

[89] Y. Hu, Y. Nagai, D. Rahmawaty, C.H. Wei, M. Anpo, Characteristics of the photocatalytic oxidation of methane into methanol on V-containing MCM-41 catalysts, Catal. Letters. 124 (2008) 80–84. https://doi.org/10.1007/s10562-008-9491-8.

[90] Y. Hu, M. Anpo, C.H. Wei, Effect of the local structures of V-oxides in MCM-41 on the photocatalytic properties for the partial oxidation of methane to methanol, J. Photochem. Photobiol. a-Chemistry. 264 (2013) 48–55. https://doi.org/10.1016/j.jphotochem.2013.05.005.

[91] A. Hameed, I.M.I. Ismail, M. Aslam, M.A. Gondal, Photocatalytic conversion of

methane into methanol: Performance of silver impregnated WO_3, Appl. Catal. a-General. 470 (2014) 327–335. https://doi.org/10.1016/j.apcata.2013.10.045.

[92] K. Villa, S. Murcia-Lopez, T. Andreu, J.R. Morante, On the role of WO_3 surface hydroxyl groups for the photocatalytic partial oxidation of methane to methanol, Catal. Commun. 58 (2015) 200–203. https://doi.org/10.1016/j.catcom.2014.09.025.

[93] K. Villa, S. Murcia-Lopez, J.R. Morante, T. Andreu, An insight on the role of La in mesoporous WO_3 for the photocatalytic conversion of methane into methanol, Appl. Catal. B-Environmental. 187 (2016) 30–36. https://doi.org/10.1016/j.apcatb.2016.01.032.

[94] S. Murcia-Lopez, M.C. Bacariza, K. Villa, J.M. Lopes, C. Henriques, J.R. Morante, T. Andreu, Controlled Photocatalytic Oxidation of Methane to Methanol through Surface Modification of Beta Zeolites, Acs Catal. 7 (2017) 2878–2885. https://doi.org/10.1021/acscatal.6b03535.

[95] S.L. Shi, Z.X. Sun, C.Y. Bao, T.S. Gao, Y.H. Hu, The special route toward conversion of methane to methanol on a fluffy metal-free carbon nitride photocatalyst in the presence of H_2O_2, Int. J. Energy Res. 44 (2020) 2740–2753. https://doi.org/10.1002/er.5088.

[96] Y. Zeng, H.C. Liu, J.S. Wang, X.Y. Wu, S.L. Wang, Synergistic photocatalysis-Fenton reaction for selective conversion of methane to methanol at room temperature, Catal. Sci. Technol. 10 (2020) 2329–2332. https://doi.org/10.1039/d0cy00028k.

[97] H. Song, X.G. Meng, S.Y. Wang, W. Zhou, S. Song, T. Kako, J.H. Ye, Selective Photo-oxidation of Methane to Methanol with Oxygen over Dual-Cocatalyst-Modified Titanium Dioxide, Acs Catal. 10 (2020) 14318–14326. https://doi.org/10.1021/acscatal.0c04329.

[98] X.J. Cai, S.Y. Fang, Y.H. Hu, Unprecedentedly high efficiency for photocatalytic conversion of methane to methanol over Au-Pd/TiO_2 - what is the role of each component in the system?, J. Mater. Chem. A. 9 (2021) 10796–10802. https://doi.org/10.1039/d1ta00420d.

7. ACADEMIC PRODUCTION

[1] J.A. de Oliveira, **J.C. da Cruz**, O.R. Nascimento, C. Ribeiro, Selective CH_4 reform to methanol through partial oxidation over Bi_2O_3 at room temperature and pressure, ***Appl. Catal. B Environ***. 318 (2022) 1–10. https://doi.org/10.1016/j.apcatb.2022.121827.

[2] E.H. Dias, G.T.S.T. Da Silva, **J.C. Da Cruz**, C. Ribeiro, One-Pot Solvothermal Synthesis of Carbon Black-Supported CuO for Catalysis of CO_2 Electroreduction, ***ChemElectroChem*.** 9 (2022) 1–7. https://doi.org/10.1002/celc.202200206.

[3] L.V. Dutra, C.R. de Oliveira Fontoura, **J.C. da Cruz**, M.A. Nascimento, A.F. de Oliveira, R.P. Lopes, Green synthesis optimization of graphene quantum dots by Doehlert design for dye photodegradation application, ***Colloids Surfaces A Physicochem. Eng. Asp*.** 651 (2022). https://doi.org/10.1016/j.colsurfa.2022.129442.

[4] J.C. Peixoto, A.E. Nogueira, A. Dias, J.A. Torres, **J.C. da Cruz**, C. Ribeiro, K.P.F. Siqueira, Experimental evaluation of the activity and selectivity of pure $MnWO_4$ and doped with rare earth ions in the CO_2 photoreduction process, ***Mater. Res. Bull.*** 153 (2022). https://doi.org/10.1016/j.materresbull.2022.111912.

[5] M. Santos Anholeti, A. Rocha Honorio de Oliveira, **J. Castro da Cruz**, V. Andrade Luciano, M. Aparecida Nascimento, G. Alves Puiatti, A.P. de Carvalho Teixeira, R. Pereira Lopes, Zn/ZnO heterostructures photocatalyst obtained by sustainable processes from alkaline batteries waste: Synthesis, characterization and application, ***Mater. Chem. Phys***. 284 (2022) 126058. https://doi.org/10.1016/j.matchemphys.2022.126058.

[6] J.A. Torres, **J.C. da Cruz**, A.E. Nogueira, G.T.S.T. da Silva, J.A. de Oliveira, C. Ribeiro, Role of Cu^0-TiO_2 interaction in catalyst stability in CO_2 photoreduction process, ***J. Environ. Chem. Eng.*** 10 (2022). https://doi.org/10.1016/j.jece.2022.107291.

[7] A.L.A. Faria, H.A. Centurion, J.A. Torres, R. V. Gonçalves, L.S. Ribeiro, C. Riberio, **J.C. da Cruz**, F.G.E. Nogueira, Enhancing Nb_2O_5 activity for CO_2 photoreduction through Cu nanoparticles cocatalyst deposited by DC-magnetron sputtering, ***J. CO_2 Util***. 53 (2021) 101739. https://doi.org/10.1016/j.jcou.2021.101739.

[8] D.S.D. Lima, **J.C. Cruz**, V.A. Luciano, M.A. Nascimento, A.P.C. Teixeira, R.P. Lopes, Enhanced photocatalytic activity of cobalt-doped titanate nanotube heterostructures decorated with Cu_2O-CuO nanoparticles for organic pollutant degradation under UV and visible irradiation, ***Appl. Surf. Sci***. 563 (2021) 150313. https://doi.org/10.1016/j.apsusc.2021.150313.

8. APPENDIX

1. Partial photooxidation of CH_4 to CH_3OH: rate of transferred electrons

The mols of electrons involved in the partial photooxidation of CH_4 into CH_3OH was calculated considering the number of electrons transferred per mol of produced methyl hydroperoxide and methanol, according to reactions showed in Eqs. A3.1-A3.2 [17].

$$CH_3O_2^{\bullet}{}_{(aq)} + H^+{}_{(aq)} + e^- \rightarrow CH_3OOH_{(aq)} \qquad 1\ mol\ e^-/mol_{CH_3OOH} \qquad (A3.1)$$

$$CH_3OOH_{(aq)} + 2e^- + 2H^+{}_{(aq)} \rightarrow CH_3OH_{(aq)} + H_2O_{(l)} \qquad 2\ mol\ e^-/mol_{CH_3OH} \qquad (A3.2)$$

As observed from Eq. A3.1, formation of methyl hydroperoxide needs one electron, while two more electrons need to be transferred to reduce one mol of CH_3OOH into one mol of CH_3OH (Eq. A3.2).

2. Calculations for CH_4 feedstock

We proceed to a very detailed investigation of the total CH_4 available for reaction. We purged 100 mL deionized water with CH_4 standard gas during 30 min, injecting 1 μL of the liquid aliquots on a gas chromatography (GC). The CH_4 peak areas were:

For the aqueous medium purged with the standard gas containing 20%mol CH_4: 10,196
For the aqueous medium purged with the standard gas containing 99%mol CH_4: 98,763

We also injected on the GC 1 μL aliquots of the standard gases, and the CH_4 peak areas results were:

For the standard gas containing 20%mol CH_4: 272,220

$$n_{CH_4} = x_{CH_4} \frac{P\,V}{R\,T} \rightarrow n_{CH_4} = (0.2) \frac{(101325\ Pa)\left(10^{-9}\ m^3\right)}{\left(8.314462\ \frac{J}{K\ mol}\right)(298.15\ K)} \rightarrow n_{CH_4} = 8.17\ x\ 10^{-9}\ mol$$

For the standard gas containing 99%mol CH_4: 1,017,631

$$n_{CH_4} = x_{CH_4} \frac{P\,V}{R\,T} \rightarrow n_{CH_4} = (0.99) \frac{(101325\ Pa)\left(10^{-9}\ m^3\right)}{\left(8.314462\ \frac{J}{K\ mol}\right)(298.15\ K)} \rightarrow n_{CH_4} = 4.05\ x\ 10^{-8}\ mol$$

We can compare these results of moles of CH_4 contained in 1 μL of the standard gases with the peak areas of CH_4 for the aqueous medium purged with the standard gases.

For the aqueous medium purged with the standard gas containing 20%mol CH_4:

272,220 -------- 8.17×10^{-9} mol

10,196 -------- x ⟶ 3.06×10^{-10} mol CH_4 in 1 μL

1 μL = 0.001 mL ------ 3.06×10^{-10} mol CH_4

100 mL ------ x ⟶ 3.06×10^{-5} = **31 μmol CH_4 dissolved in 100 mL**

For the aqueous medium purged with the standard gas containing 99%mol CH_4:

1,017,631 -------- 4.05×10^{-8} mol

98,763 -------- x ⟶ 3.93×10^{-9} mol CH_4 in 1 μL

1 μL = 0.001 mL ------ 3.93×10^{-9} mol CH_4

100 mL ------ x ⟶ 3.93×10^{-4} = **393 μmol CH_4 dissolved in 100 mL**

These measurements evidenced that the total available CH_4 is much higher than the simple estimation of gas phase. We emphasize that, due the limitation of equipment access, we opted to analyze a single condition (i.e., CH_4 bubbling in water, with no catalyst), which can vary depending on the catalyst (higher/lower adsorption capacity), presence of peroxide, and medium conductivity.

Moreover, our ESR investigations demonstrated that the interaction with Bi_2O_3 and CH_4 in dark can promote some oxidation to methanol and other C1+ products. This also has another source of interference regarding the CH_4 feedstock for reaction, that is, the increased CH_4 solubility in organic medium. It is known that the methane solubility can rise in organic medium or with organic contaminations [85]. Thus, the methane feedstock needs to be further investigated but do not change the final conclusions of our paper.

3. Calculations for CH_3OH production rate by gas chromatography

We proceed to comparative measurements with gas chromatography (GC) to confirm the reliability of NMR measurements. We insist that the advantage of NMR is to probe not only methanol, but any other liquid hydrocarbon produced by oxidation, giving a qualitative appreciation. In that sense, the technique is more powerful, and can give more information about our catalytic system. Thus, analyzing a selected condition suitable for both techniques, we choose to double-check the sample $Bi_2O_3/AgNO_3$, which produced c.a. 135 μmol g^{-1} h^{-1} according to the ^1H NMR analysis. We injected on the GC 1 μL aliquot of the sample, and the methanol GC peak area was 14,865 (please, see the raw chromatogram and the methanol calibration curve in Fig. S14-S15):

$$(CH_3OH \text{ concentration}) = \frac{(\text{peak area}) - 383}{17{,}906} \rightarrow (CH_3OH \text{ concentration}) = \frac{(14{,}865) - 383}{17{,}906}$$

$$(CH_3OH \text{ concentration}) = 0.81 \text{ mM}$$

$$0.81 \frac{\text{mmol}}{\text{L}} \text{ x } 0.1 \text{ L x } \frac{1000}{1} \frac{\mu\text{mol}}{\text{mmol}} \text{ x } \frac{1}{0.1 \text{ g}} \text{ x } \frac{1}{4 \text{ h}} = 202 \frac{\mu\text{mol}}{\text{g h}}$$

Thus, for the condition $Bi_2O_3/AgNO_3$, the methanol concentration calculated by ^1H NMR and GC is similar, indicating that our results of production rates are accurate. The difference among the values is explained by the statistical variation of the experiments (the determination in GC was done in a replica) but it is still in the confidence value.

4. <u>Reaction steps to produce the chemicals from the CH_4 photooxidation</u>

We emphasize that these reactions can be further optimized, but in this manuscript, we were dedicated to understanding how they can happen. Then, the initial reactions sequence can be summarized as follows [17,68,85]:

$$Bi_2O_{3(s)} \xrightarrow{h\nu\ (\text{visible-light})} h^+ + e^- \quad \text{(A3.3)}$$

$$H_2O_{(l)} + h^+ \rightarrow \bullet OH_{(aq)} + H^+_{(aq)} \quad \text{(A3.4)}$$

$$H_2O_{2(aq)} \rightarrow H_2O_{(l)} + 1/2\, O_{2(g)} \quad \text{(A3.5)}$$

$$H_2O_{2(aq)} \rightarrow \bullet OH_{(aq)} + OH^-_{(aq)} \quad \text{(A3.6)}$$

With the formation of these initial radicals, and taking in account the O_2 dissolved in the medium, one has the sequence for C1 products:

$$CH_{4(aq)} + \bullet OH_{(aq)} \rightarrow \bullet CH_{3(aq)} + H_2O_{(l)} \quad \text{(A3.7)}$$

$$\bullet CH_{3(aq)} + \bullet OH_{(aq)} \rightarrow CH_3OH_{(aq)} \quad \text{(A3.8)}$$

$$\bullet CH_{3(aq)} + O_{2(g)} \rightarrow CH_3O_2\bullet_{(aq)} \quad \text{(A3.9)}$$

$$CH_3O_2\bullet_{(aq)} + H^+_{(aq)} + e^- \rightarrow CH_3OOH_{(aq)} \quad \text{(A3.10)}$$

$$CH_3OOH_{(aq)} + 2e^- + 2H^+_{(aq)} \rightarrow CH_3OH_{(aq)} + H_2O_{(l)} \quad \text{(A3.11)}$$

For C2+ products, the interactions of the as-formed methanol and the radicals will play a role – indeed, since there is no separation of as-formed methanol from the reaction medium, its oxidation is totally possible, as well as its interaction with other radicals:

$$CH_3OH_{(l)} + \bullet OH_{(aq)} \rightarrow \bullet CH_2OH_{(aq)} + H_2O_{(l)} \quad \text{(A3.12)}$$

$$\bullet CH_2OH_{(aq)} + \bullet CH_{3(aq)} \rightarrow CH_3CH_2OH_{(l)} \quad \text{(A3.13)}$$

$$CH_3CH_2OH_{(aq)} + \bullet OH_{(aq)} \rightarrow CH_3\bullet CHOH_{(aq)} + H_2O_{(l)} \quad \text{(A3.14)}$$

$$CH_3\bullet CHOH_{(aq)} + \bullet CH_{3(aq)} \rightarrow (CH_3)_2CHOH_{(aq)} \quad \text{(A3.15)}$$

$$(CH_3)_2CHOH_{(aq)} + \bullet OH_{(aq)} \rightarrow (CH_3)_2\bullet COH_{(aq)} + H_2O_{(l)} \quad \text{(A3.16)}$$

$$(CH_3)_2CHOH_{(aq)} + \bullet OH_{(aq)} \rightarrow (CH_3)_2CO_{(aq)} + H_2O_{(l)} \quad \text{(A3.17)}$$

As we previously discussed, this sequence can follow to higher C2+ products, although it is less probable by the reduced interaction with the radicals. One can take in account that, in longer C2+ products, the cleavage for smaller groups is still possible, leading that the products are observed by an equilibrium of dimerization/cleavage that deserves to be investigated in the future.

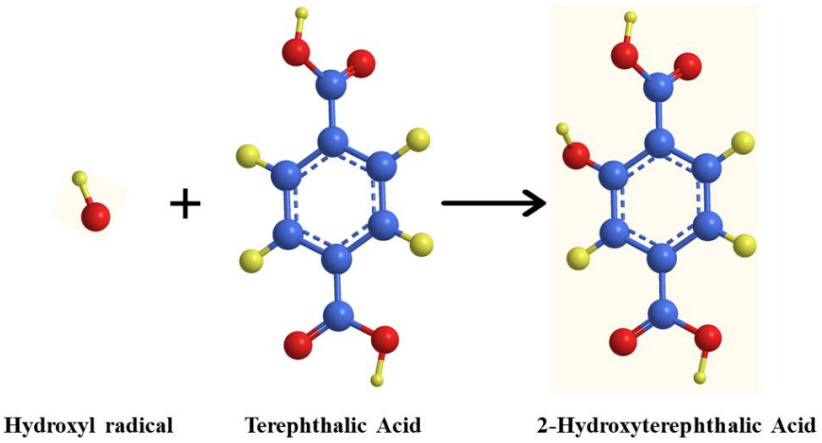

FIGURE A3.1 - Formation of 2-hydroxyterephthalic acid from hydroxyl radical and terephthalic acid. The blue, red and yellow colors represent the carbon, oxygen, and hydrogen atoms, respectively.

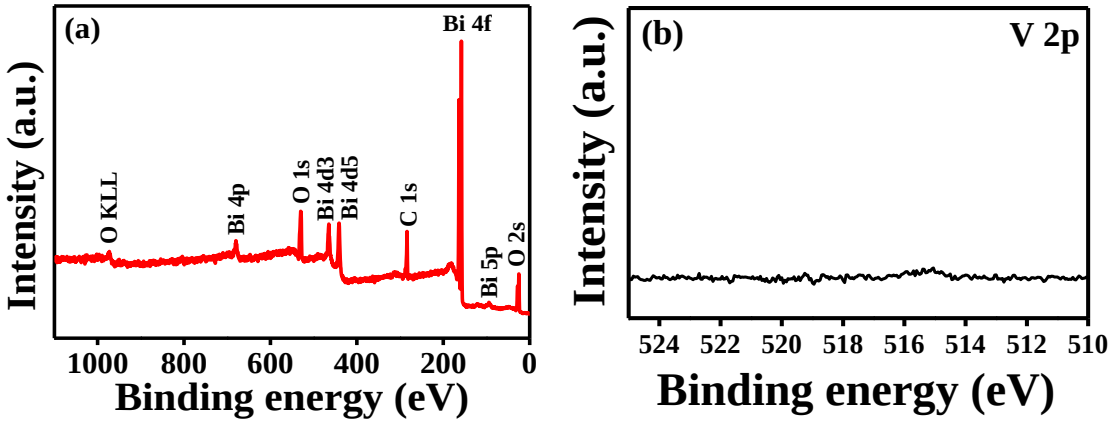

FIGURE A3.2 - (a) XPS survey spectrum and (b) high-resolution V 2p spectrum of the as-synthesized Bi_2O_3.

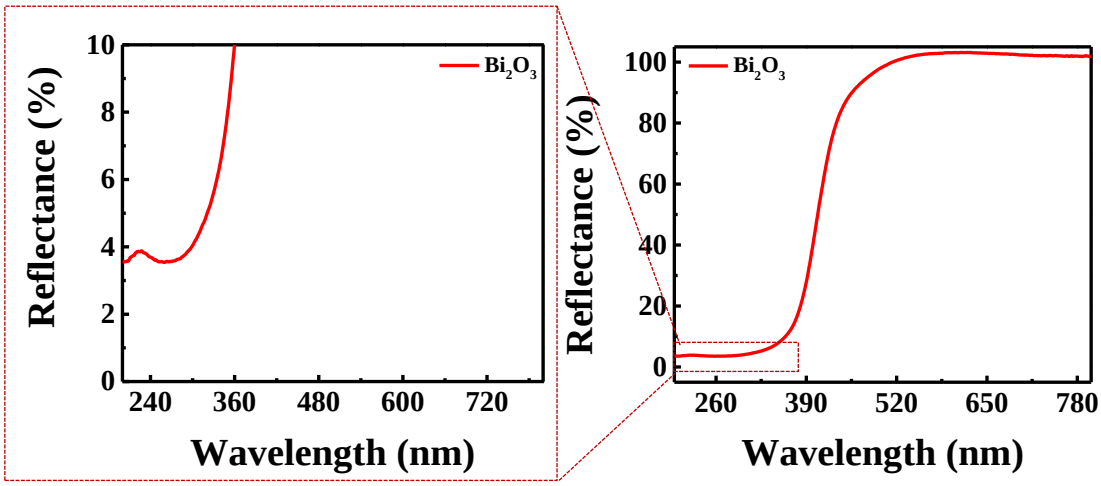

FIGURE A3.3 - Diffusive reflectance spectrum of the as-synthesized Bi_2O_3.

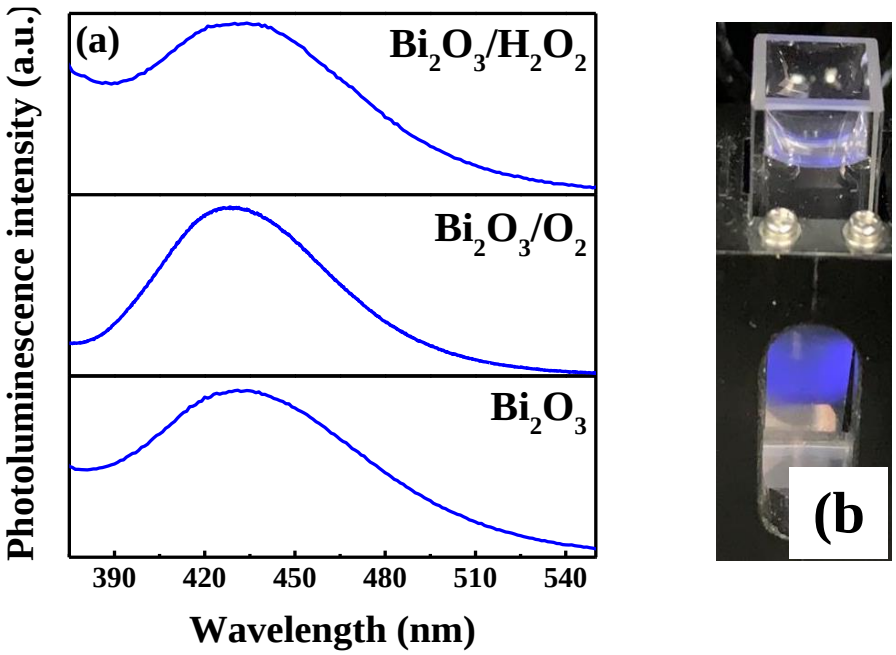

FIGURE A3.4 - (a) Determination of hydroxyl radical formation by photoluminescence spectra; and (b) photography of the fluorescence emission of •OH species with 315 nm excitation.

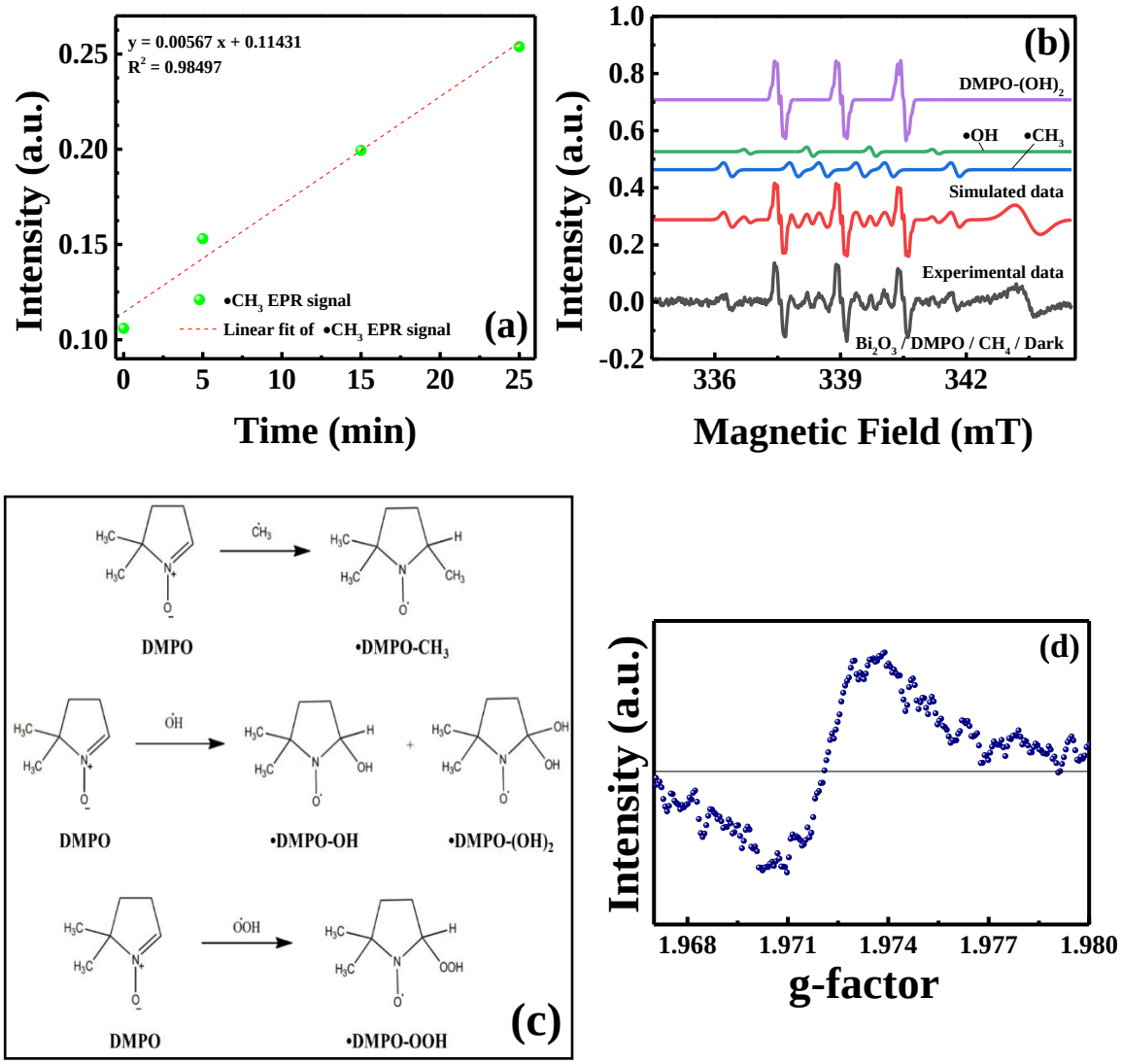

FIGURE A3.5 - (a) Linear fit of the ESR signal intensity of the methyl radicals generated using a DMPO solution containing the as-synthesized Bi_2O_3 and the methane standard gas under dark. (b) Simulated ESR spectra of the DMPO solution containing the as-synthesized Bi_2O_3 and the methane standard gas. (c) Formation of stable radical adducts between the DMPO and the reactive radical species. (d) g-factor of Cr(III):MgO used to calibrate magnetic field and relative signal intensities.

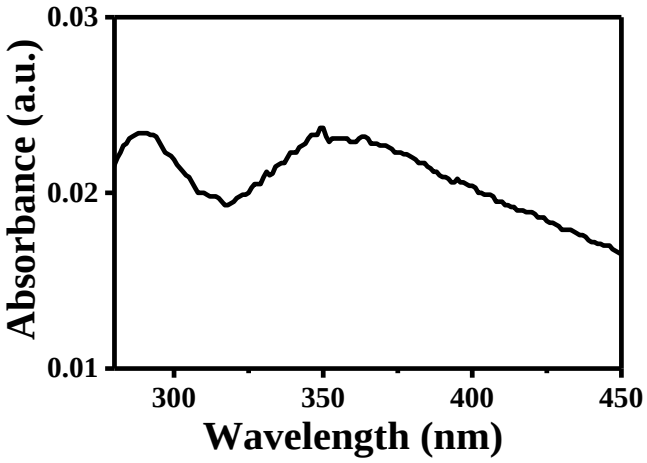

FIGURE A3.6 - In situ hydrogen peroxide generation. Reaction conditions: 1 g L^{-1} Bi_2O_3 + 1 mL pure O_2 in 100 mL deionized water under visible-light illumination (108 W and ~5 mW cm^{-2}).

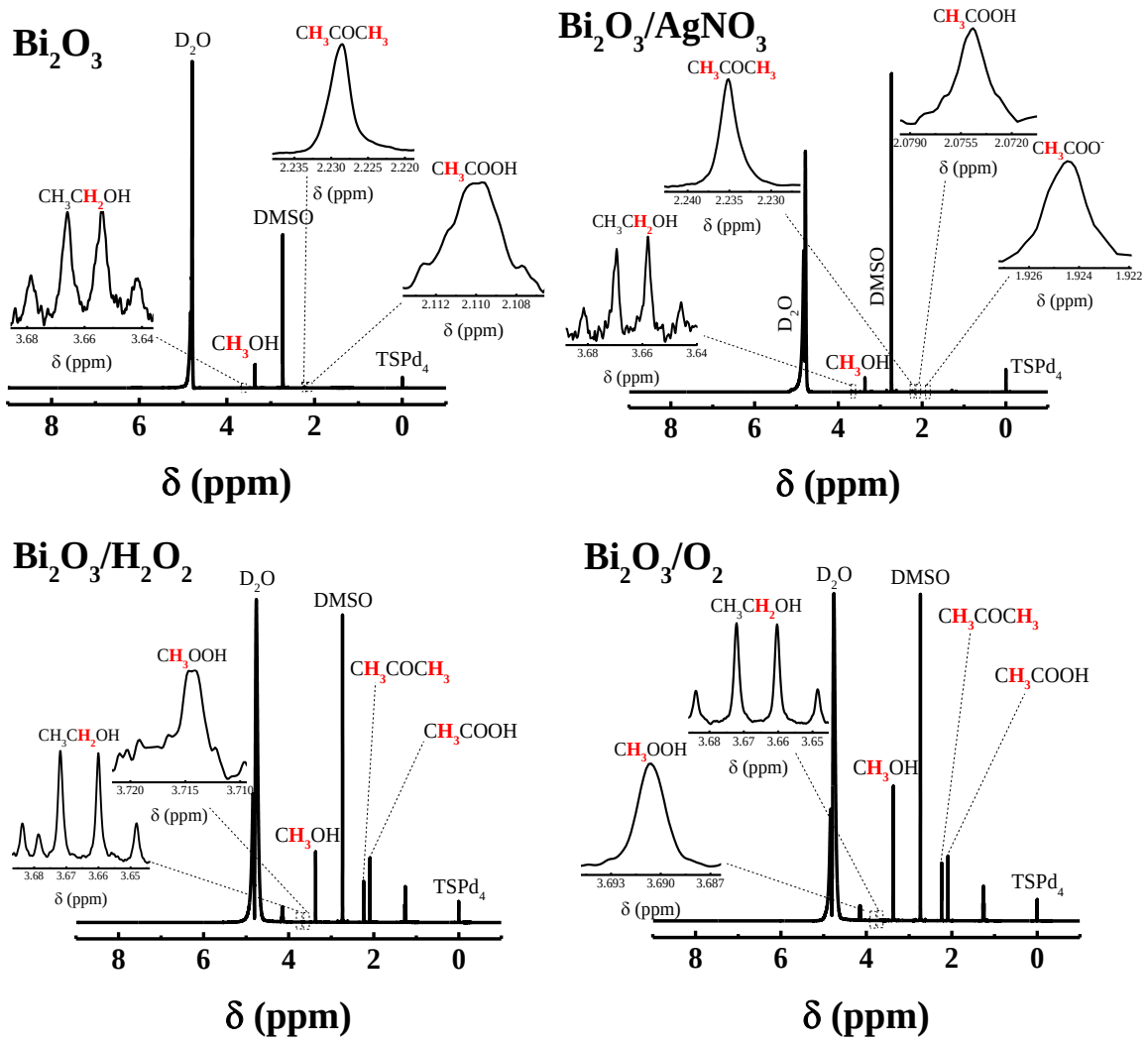

FIGURE A3.7 - ^{1}H NMR spectra of the liquid aliquots collected from the partial photooxidation of CH_4 using Bi_2O_3 as photocatalyst in the presence of $AgNO_3$, H_2O_2, and O_2. * Other signals were observed by ^{1}H NMR, but no confirmation by other analytical techniques (e. g. GC and HPLC) was achieved. Since these signals are unreliable, they were not identified and quantified.

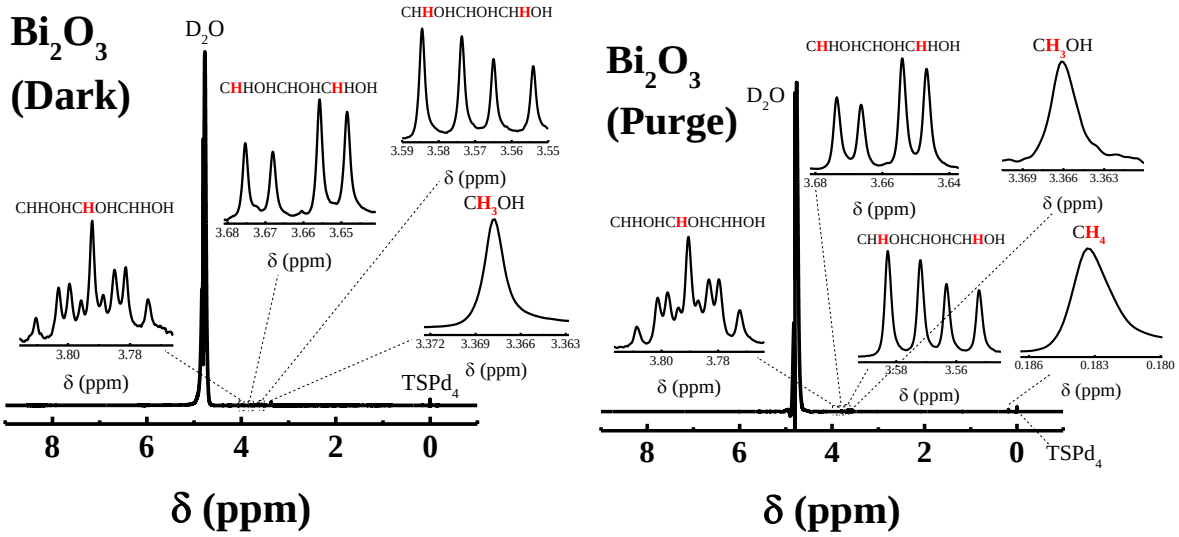

FIGURE A3.8 - ^{1}H NMR spectra of the liquid aliquots collected from the partial photooxidation of CH_4 using Bi_2O_3 as photocatalyst before the light-illumination and after 30 min purge of the standard gas containing 20%mol CH_4 in argon (before the photocatalytic reaction).

24/06/2022 11:29:52 Page 1 / 1

SHIMADZU LabSolutions **Analysis Report**

<Sample Information>

Sample Name	: 20%CH4_líquido_		
Sample ID	: 20%CH4_líquido_		
Data Filename	: 20%CH4_líquido_1.gcd		
Method Filename	: Injecao-Seringa.gcm		
Batch Filename	:		
Vial #	: 1	Sample Type	: Unknown
Injection Volume	: 1 uL		
Date Acquired	: 24/02/2022 14:33:03	Acquired by	: System Administrator
Date Processed	: 24/02/2022 14:42:26	Processed by	: System Administrator

<Chromatogram>

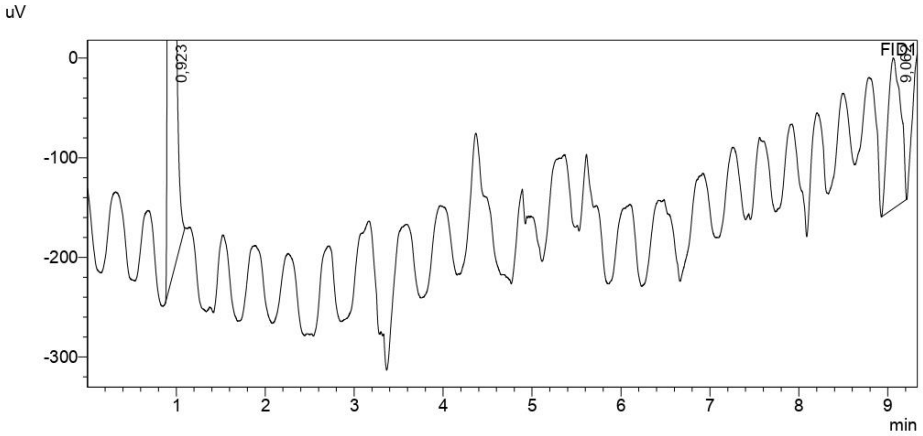

<Peak Table>

FID1

Peak#	Ret. Time	Area	Height	Conc.	Unit	Mark	Name
1	0,923	10196	3165	0,005	%		DME
2	9,062	1514	151	0,000			
Total		11710	3316				

TCD1

Peak#	Ret. Time	Area	Height	Conc.	Unit	Mark	Name
Total							

TCD2

Peak#	Ret. Time	Area	Height	Conc.	Unit	Mark	Name
Total							

C:\LabSolutions\Data\Project1\Isa\Março - 2022\20%CH4_líquido_1.gcd

FIGURE A3.9 - Raw GC data of the aqueous medium purged with the standard gas containing 20%mol CH_4 in argon. It was obtained a total of c.a. 31 μmol CH_4 dissolved in 100 mL.

24/06/2022 11:30:23 Page 1 / 1

SHIMADZU LabSolutions **Analysis Report**

<Sample Information>

Sample Name	: CH4_líquido_		
Sample ID	: CH4_líquido_		
Data Filename	: CH4_líquido_1.gcd		
Method Filename	: Injecao-Seringa.gcm		
Batch Filename	:		
Vial #	: 1	Sample Type	: Unknown
Injection Volume	: 1 uL		
Date Acquired	: 24/02/2022 15:08:55	Acquired by	: System Administrator
Date Processed	: 24/02/2022 15:18:17	Processed by	: System Administrator

<Chromatogram>

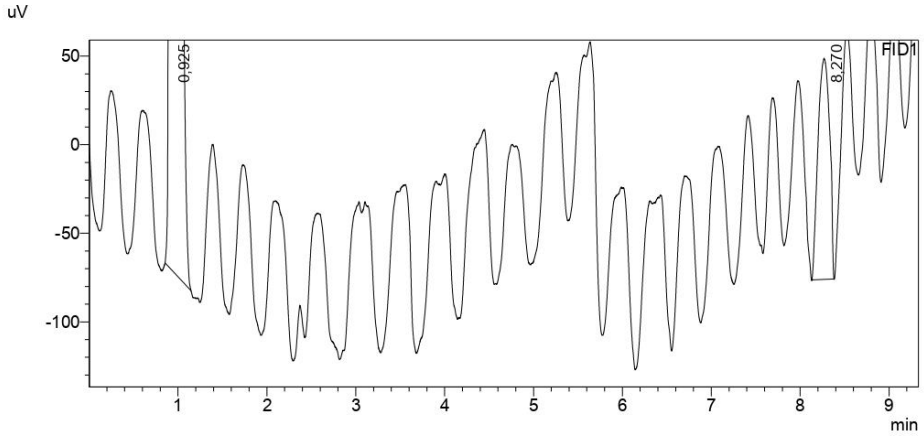

<Peak Table>

FID1

Peak#	Ret. Time	Area	Height	Conc.	Unit	Mark	Name
1	0,925	98763	31883	0,049	%		DME
2	8,270	1133	125	0,000			
Total		99895	32008				

TCD1

Peak#	Ret. Time	Area	Height	Conc.	Unit	Mark	Name
Total							

TCD2

Peak#	Ret. Time	Area	Height	Conc.	Unit	Mark	Name
Total							

C:\LabSolutions\Data\Project1\Isa\Março - 2022\CH4_líquido_1.gcd

FIGURE A3.10 - Raw GC data of the aqueous medium purged with the standard gas containing 99%mol CH_4. It was obtained a total of c.a. 393 μmol CH_4 dissolved in 100 mL.

SHIMADZU LabSolutions **Analysis Report**

<Sample Information>

Sample Name	: CH4_20%_		
Sample ID	: CH4_20%_		
Data Filename	: CH4_20%_1.gcd		
Method Filename	: Injecao-Seringa.gcm		
Batch Filename	:		
Vial #	: 1	Sample Type	: Unknown
Injection Volume	: 1 uL		
Date Acquired	: 10/03/2022 14:09:03	Acquired by	: System Administrator
Date Processed	: 10/03/2022 14:18:26	Processed by	: System Administrator

<Chromatogram>

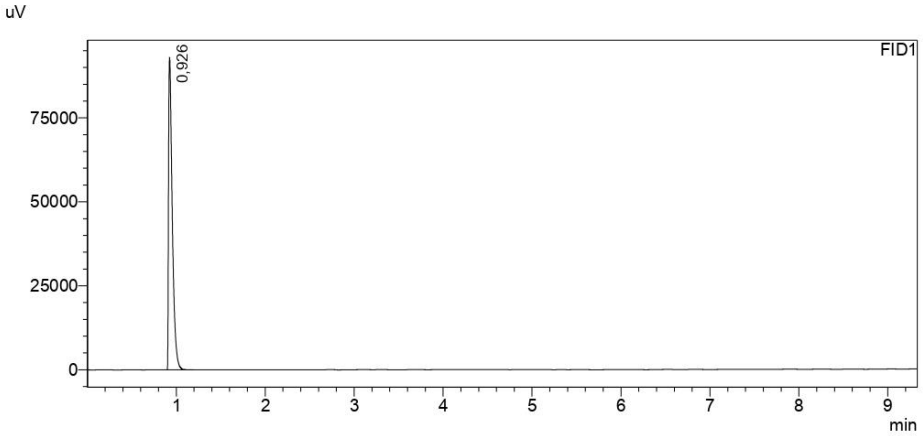

<Peak Table>

FID1

Peak#	Ret. Time	Area	Height	Conc.	Unit	Mark	Name
1	0,926	272220	92258	0,135	%		DME
Total		272220	92258				

TCD1

Peak#	Ret. Time	Area	Height	Conc.	Unit	Mark	Name
Total							

TCD2

Peak#	Ret. Time	Area	Height	Conc.	Unit	Mark	Name
Total							

FIGURE A3.11 - Raw GC data of the standard gas containing 20%mol CH_4 in argon.

SHIMADZU LabSolutions **Analysis Report**

<Sample Information>

Sample Name	: CH4_		
Sample ID	: CH4_		
Data Filename	: CH4_1.gcd		
Method Filename	: Injecao-Seringa.gcm		
Batch Filename	:		
Vial #	: 1	Sample Type	: Unknown
Injection Volume	: 1 uL		
Date Acquired	: 10/03/2022 16:07:52	Acquired by	: System Administrator
Date Processed	: 10/03/2022 16:18:34	Processed by	: System Administrator

<Chromatogram>

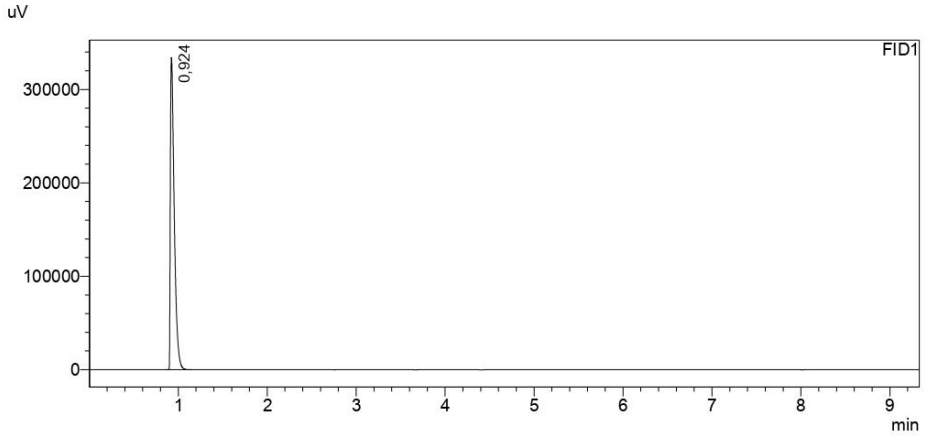

<Peak Table>

FID1

Peak#	Ret. Time	Area	Height	Conc.	Unit	Mark	Name
1	0,924	1017631	332514	0,504	%		DME
Total		1017631	332514				

TCD1

Peak#	Ret. Time	Area	Height	Conc.	Unit	Mark	Name
Total							

TCD2

Peak#	Ret. Time	Area	Height	Conc.	Unit	Mark	Name
Total							

C:\LabSolutions\Data\Project1\Isa\Março - 2022\10-03-2022\CH4_1.gcd

FIGURE A3.12 - Raw GC data of the standard gas containing 99%mol CH_4.

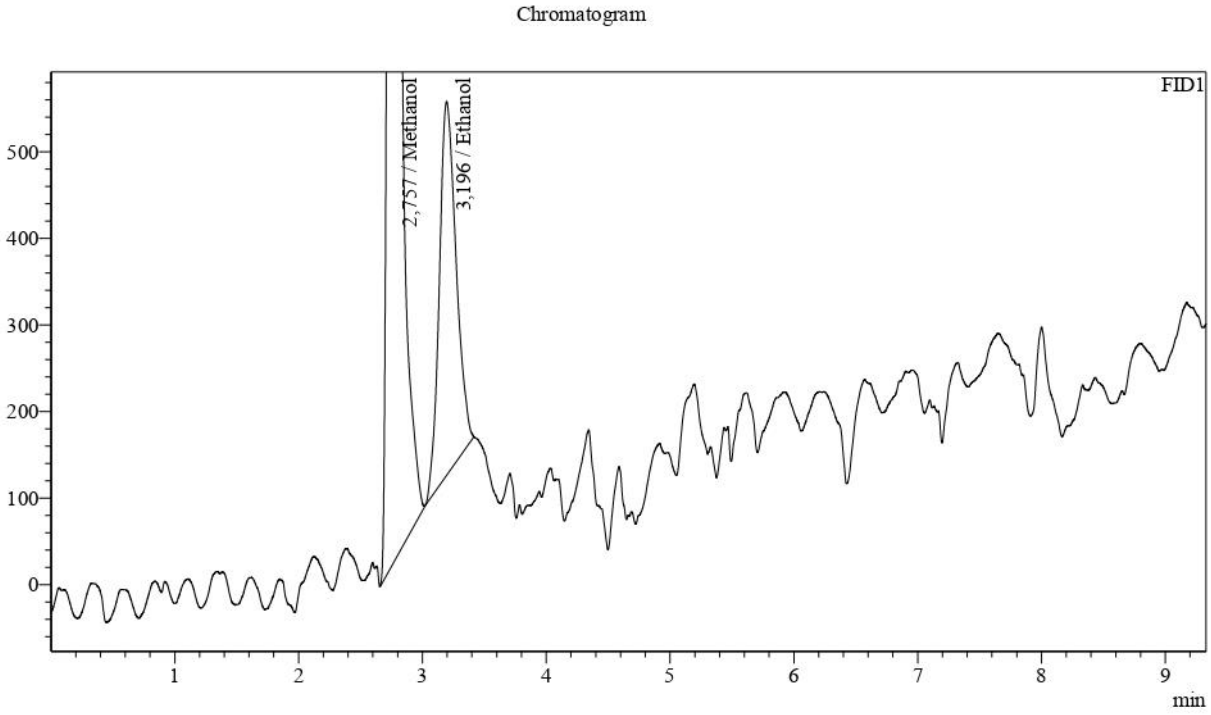

QuantitativeResult

FID1

ID#	Name	Ret. Time	Area	Height	Conc.	Unit
1	DME	--	--	--	--	%
2	Methanol	2,757	14865	2543	0,015	%
3	Ethanol	3,196	4074	432	0,002	%
4	Propanol	--	--	--	--	%
Total			18939	2974		

FIGURE A3.13 - Raw GC data of the liquid sample from CH_4 photooxidation. Reaction conditions: 1 g L^{-1} Bi_2O_3 in 100 mL of 1.0 mM $AgNO_3$ under visible-light. The reaction was carried out for 4 h using a mixture of CH_4 in argon (20%mol CH_4). $Bi_2O_3/AgNO_3$ produced c.a. 202 μmol g^{-1} h^{-1} CH_3OH. The methanol determination by ^1H NMR analysis led to 135 μmol g^{-1} h^{-1}, a similar value.

* The difference among the values is explained by the statistical variation of the experiments (the determination in GC was done in a replica) but it is still in the confidence value.

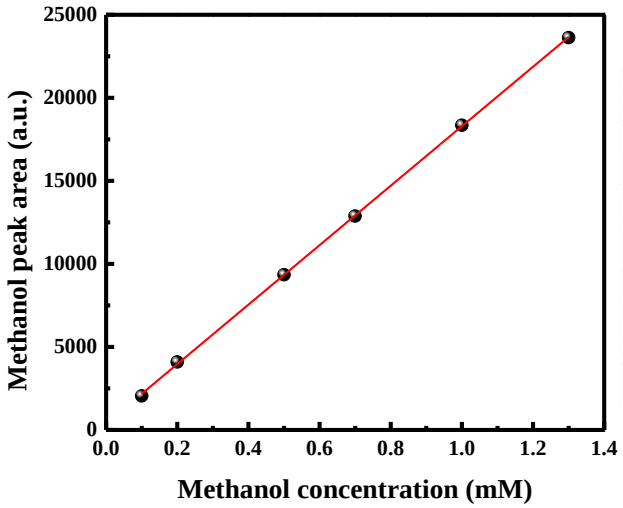

	A	B	C	D
1	Equation	y = a + b*x		
2	Weight	No Weighting		
3	Residual Sum of Squares	39949.84092		
4	Pearson's r	0.99994		
5	Adj. R-Square	0.99985		
6			Value	Standard Error
7	Área	Intercept	382.69669	73.46394
8		Slope	17906.35611	96.46288

FIGURE A3.14 - Methanol calibration curve.

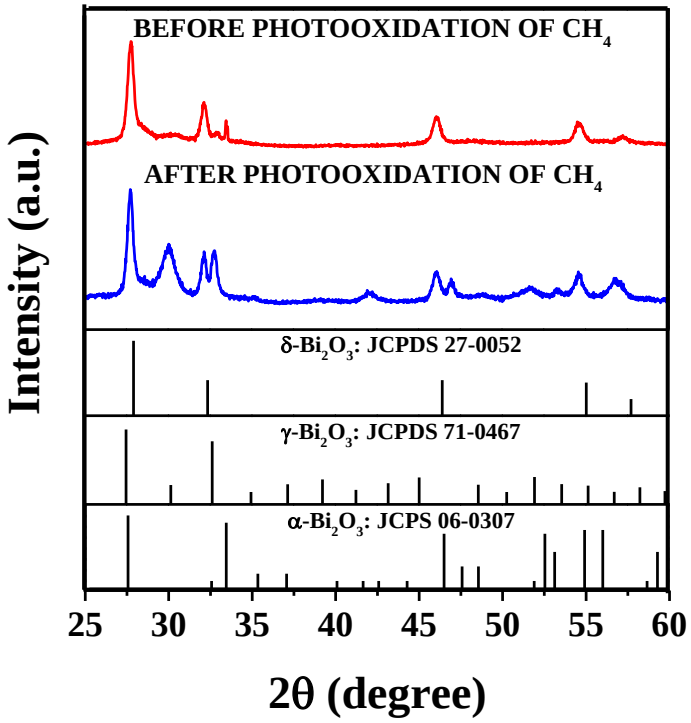

FIGURE A3.15 - XRD of the as-synthesized Bi_2O_3 before and after the CH_4 photooxidation.

TABLE A2.1 - Production rates of methanol and their reaction conditions.

Entry	Photocatalyst	Reaction conditions						Production rate of CH_3OH ($\mu mol\ g^{-1}\ h^{-1}$)	Ref.
		Light source	Light intensity ($mW\ cm^{-2}$)	Power (W)	Temp. (°C)	Pres. (kPa)*	Sacrificial reagent		
a	Mo/TiO_2	UV	-	250	60	0.1	-	13	[86]
b	TiO_2	UV	-	-	25	0.1	-	333	[87]
c	V/MCM-41	UV	-	100	22	0.1	NO	2	[88]
d	V/MCM-41	UV	-	100	22	<0.1	NO/O_2	3	[89]
e	V/MCM-41	UV	-	100	22	<0.1	NO	3	[90]
f	$10wt\%Ag_2O/WO_3$	Vis	-	-	90	0.1	-	4	[91]
g	$BiVO_4$	UV/Vis	-	450	55	0.1	NO_2^-	13	[13]
h	WO_3	UV/Vis	-	-	55	0.1	-	17	[92]
i	WO_3	UV/Vis	-	-	55	0.1	Fe^{3+}	68	[43]
j	La/WO_3	UV/Vis	-	-	55	0.1	-	5	[93]
k	$Zeolite/BiVO_4/V_2O_5$	Vis	-	450	70	0.1	-	11	[94]
l	$BiVO_4$	Vis	-	350	65	0.1	-	152	[35]
m	$0.33wt\%FeO_x/TiO_2$	Vis	100	300	25	0.1	H_2O_2	352	[1]
n	0.10wt%Pd/ZnO	UV	100	300	25	2.1	O_2	3035	[17]
o	*g*-C_3N_4	Vis	-	300	35	3.0	H_2O_2	140	[95]
p	$1.98wt\%FeOOH/WO_3$	Vis	82	300	25	0.1	H_2O_2	211	[2]
q	TiO_2	UV	-	300	30	3.0	Fe^{2+}/H_2O_2	471	[96]
r	0.30wt%Au/ZnO	UV	100	-	30	2.0	O_2	1000	[69]
s	$Au\text{-}CoO_x/TiO_2$	Vis	450	300	25	2.1	O_2	1500	[97]
t	$1wt\%Au\text{-}Pd/TiO_2$	UV/Vis	250	-	52.3	4000	H_2O/O_2	12600	[98]
u	$BiVO_4$	Vis	170	-	25	2000	O_2	2270	[33]

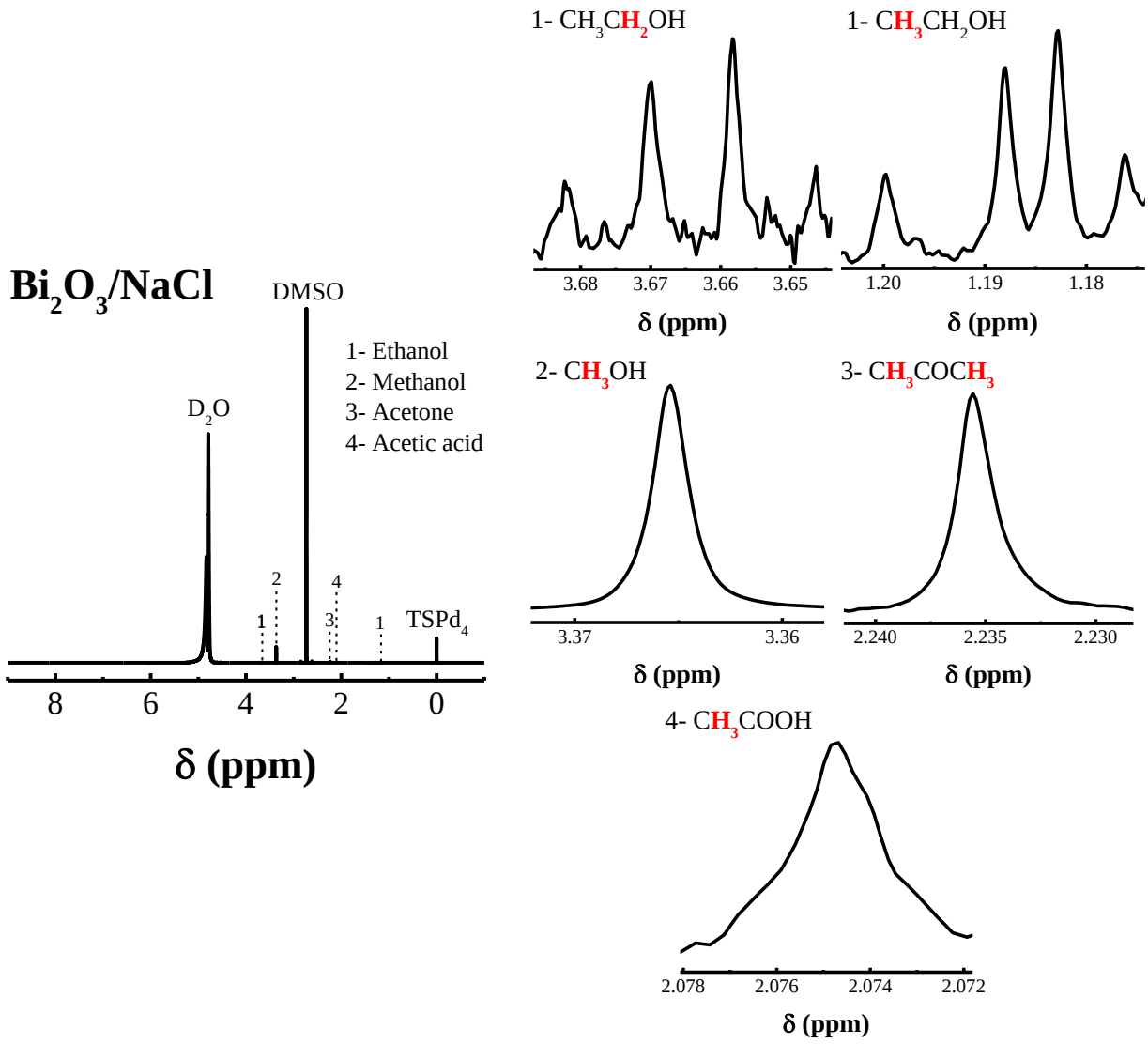

Figura A4.1 - ^{1}H NMR spectrum of the liquid aliquot collected from the partial photooxidation of CH_4 using Bi_2O_3 as photocatalyst in the presence of NaCl. This analysis used 60 µL of D_2O solution containing 50 mM of the standard dimethyl sulfoxide (DMSO) and 0.21 mM of the reference 3-(trimethylsilyl) propionic-2,2,3,3-d_4 acid sodium salt ($TSPd_4$).

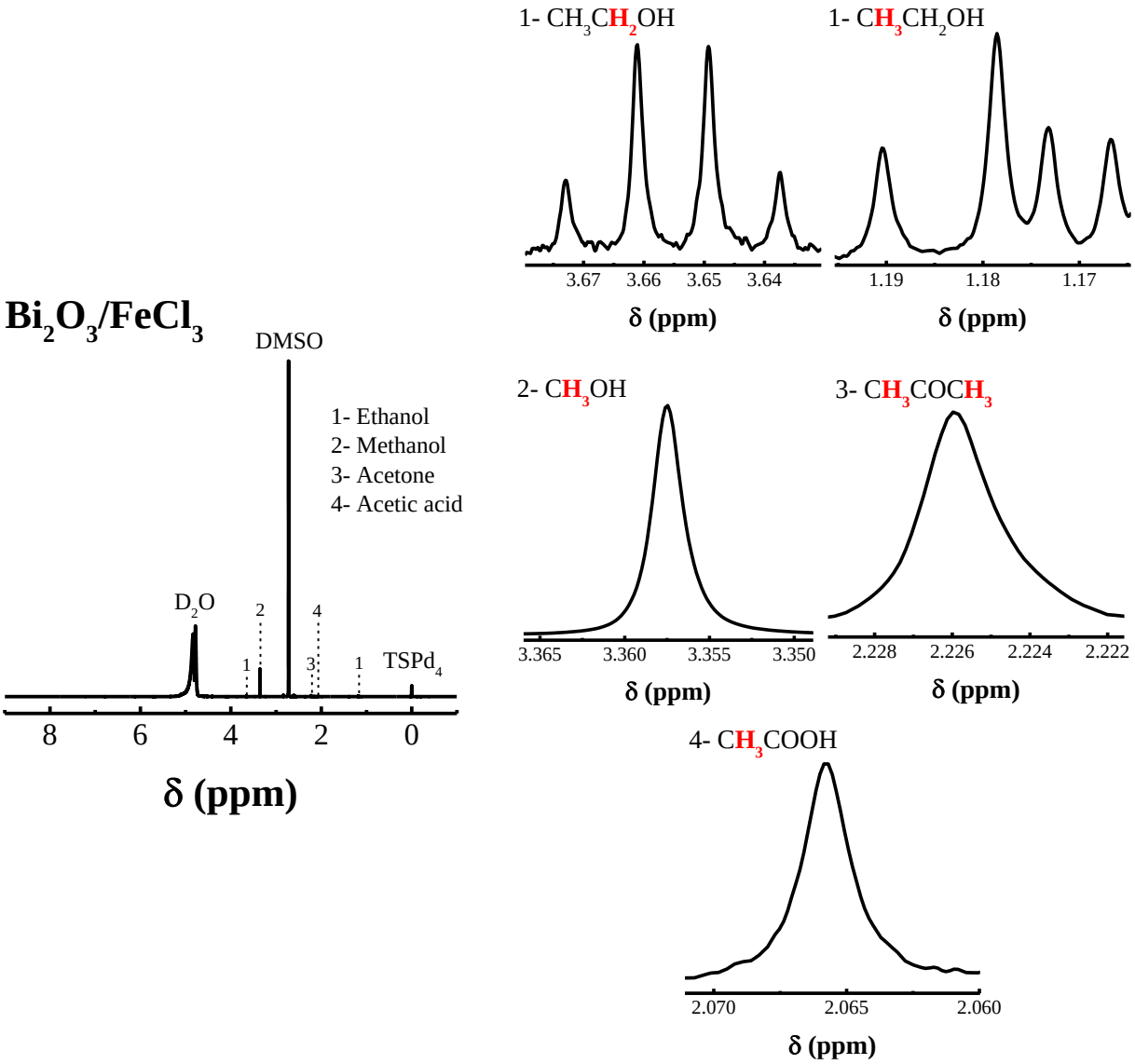

FIGURE A4.2 - ^{1}H NMR spectrum of the liquid aliquot collected from the partial photooxidation of CH_4 using Bi_2O_3 as photocatalyst in the presence of $FeCl_3$. This analysis used 60 µL of D_2O solution containing 50 mM of the standard dimethyl sulfoxide (DMSO) and 0.21 mM of the reference 3-(trimethylsilyl) propionic-2,2,3,3-d_4 acid sodium salt ($TSPd_4$).

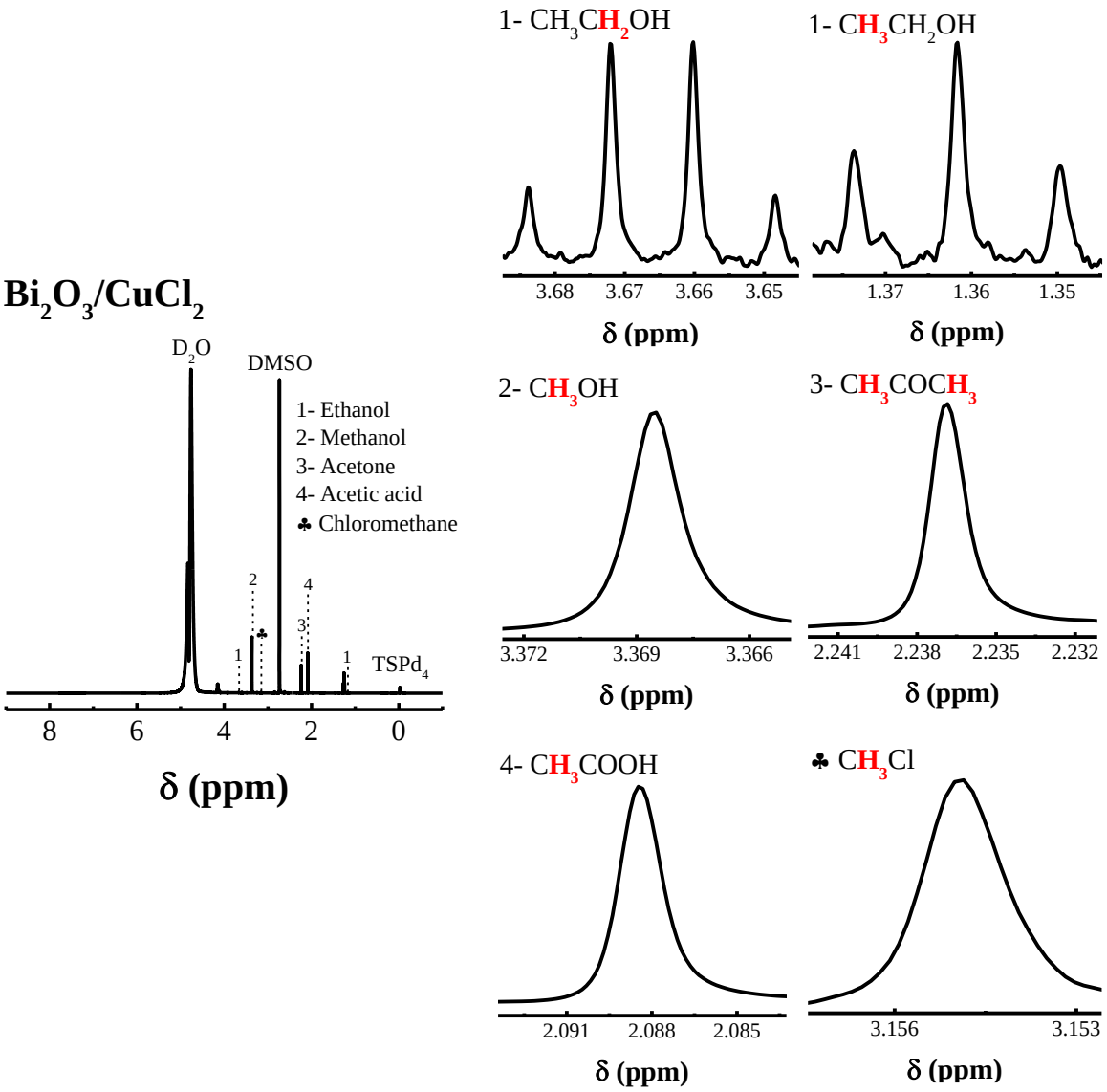

FIGURE A4.3 - ^{1}H NMR spectrum of the liquid aliquot collected from the partial photooxidation of CH_4 using Bi_2O_3 as photocatalyst in the presence of $CuCl_2$. This analysis used 60 µL of D_2O solution containing 50 mM of the standard dimethyl sulfoxide (DMSO) and 0.21 mM of the reference 3-(trimethylsilyl) propionic-2,2,3,3-d_4 acid sodium salt ($TSPd_4$).

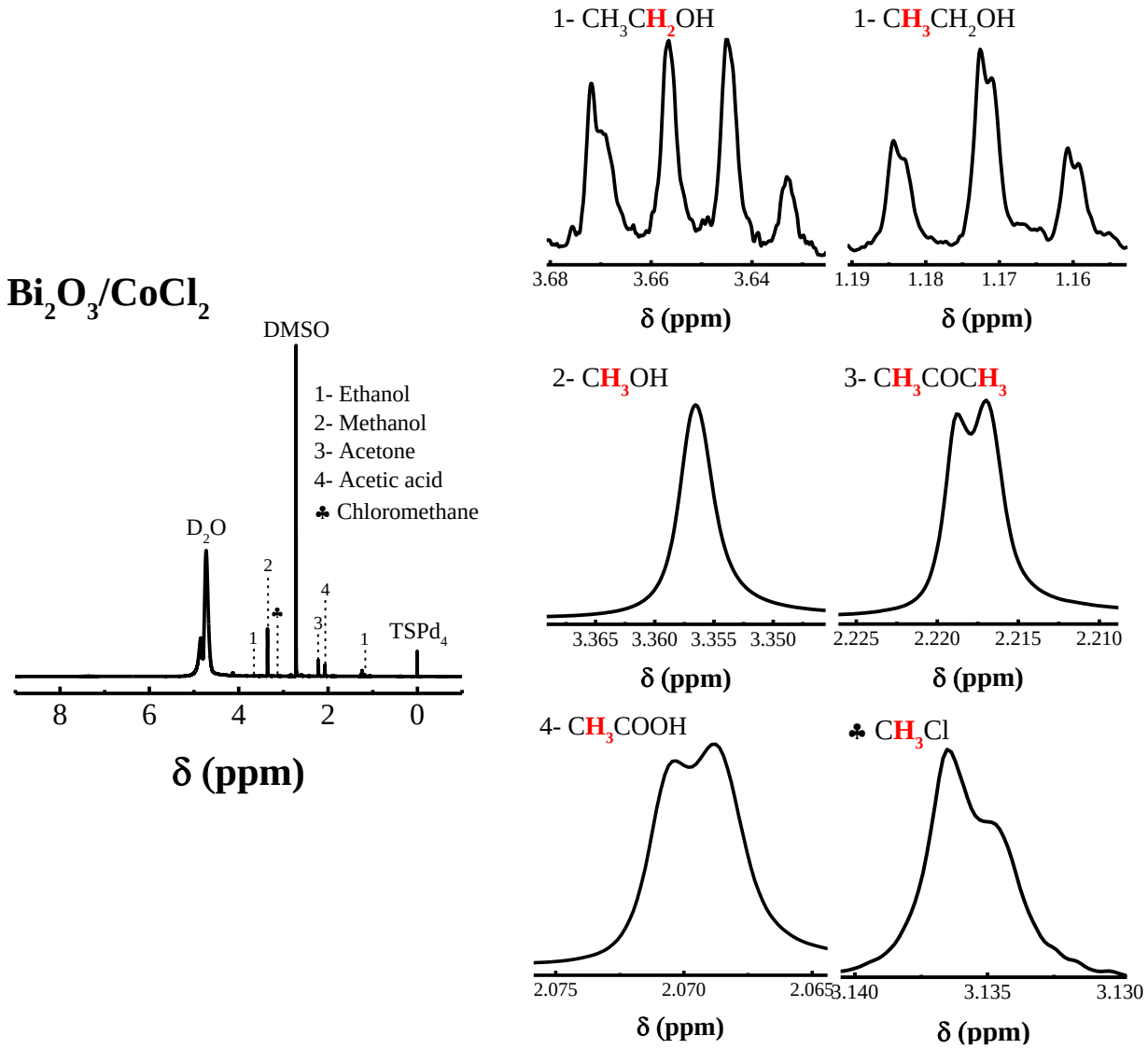

FIGURE A4.4 - ^{1}H NMR spectrum of the liquid aliquot collected from the partial photooxidation of CH_4 using Bi_2O_3 as photocatalyst in the presence of $CoCl_2$. This analysis used 60 µL of D_2O solution containing 50 mM of the standard dimethyl sulfoxide (DMSO) and 0.21 mM of the reference 3-(trimethylsilyl) propionic-2,2,3,3-d_4 acid sodium salt ($TSPd_4$).

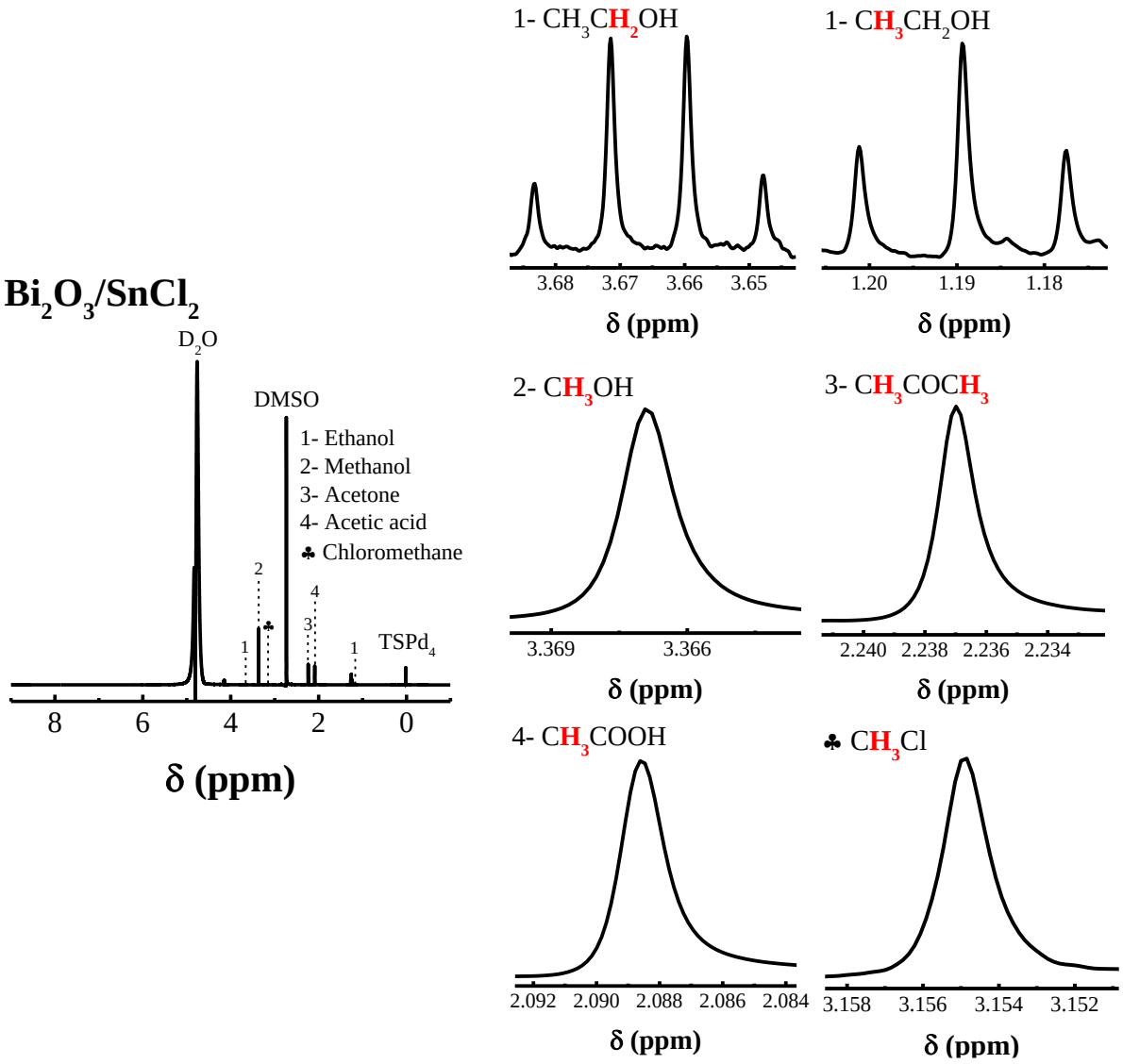

FIGURE A4.5 - ^{1}H NMR spectrum of the liquid aliquot collected from the partial photooxidation of CH_4 using Bi_2O_3 as photocatalyst in the presence of $SnCl_2$. This analysis used 60 µL of D_2O solution containing 50 mM of the standard dimethyl sulfoxide (DMSO) and 0.21 mM of the reference 3-(trimethylsilyl) propionic-2,2,3,3-d_4 acid sodium salt ($TSPd_4$).

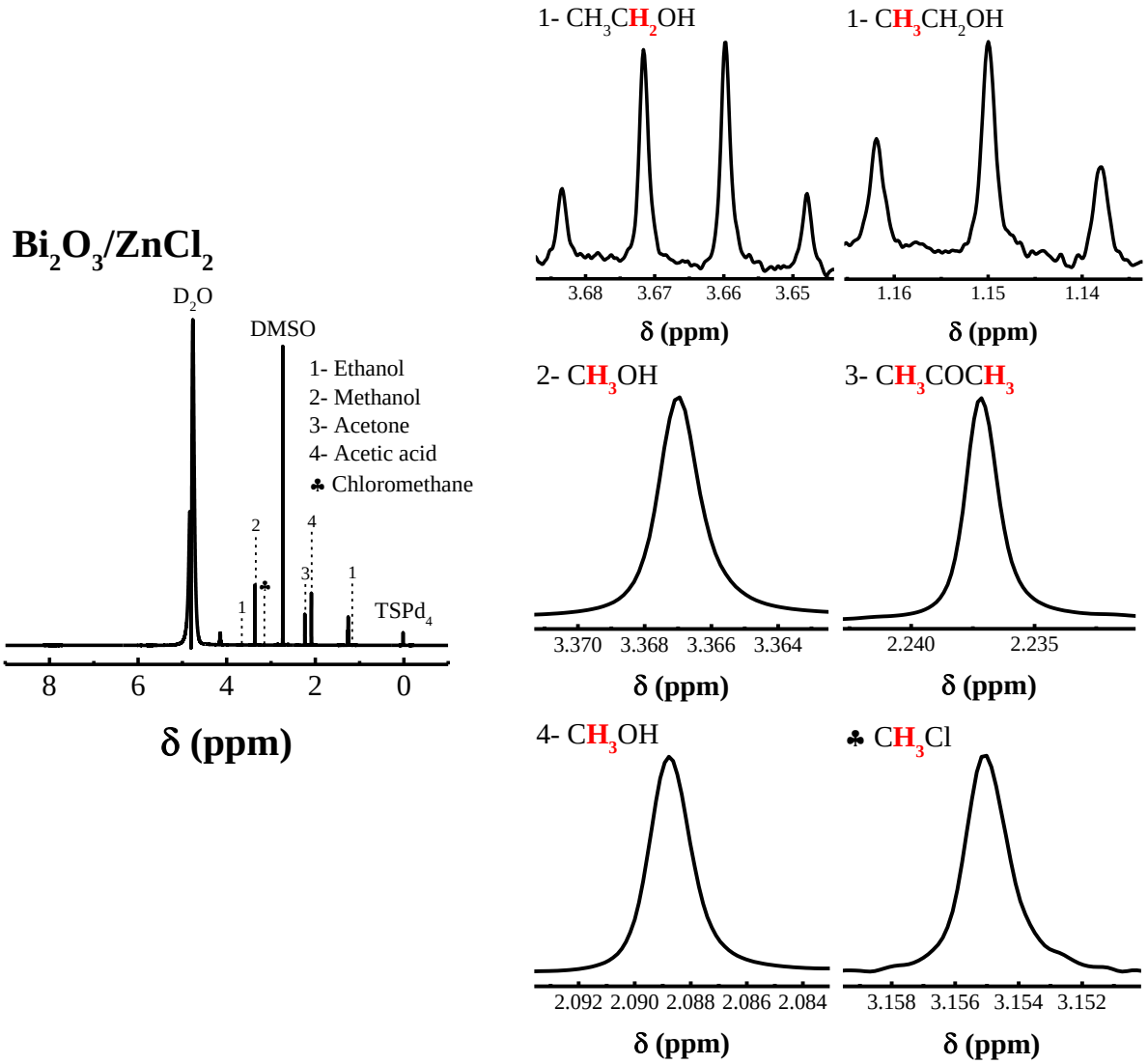

FIGURE A4.6 - ^{1}H NMR spectrum of the liquid aliquot collected from the partial photooxidation of CH_4 using Bi_2O_3 as photocatalyst in the presence of $ZnCl_2$. This analysis used 60 µL of D_2O solution containing 50 mM of the standard dimethyl sulfoxide (DMSO) and 0.21 mM of the reference 3-(trimethylsilyl) propionic-2,2,3,3-d_4 acid sodium salt ($TSPd_4$).

Complementary analysis of CH_3OH concentration by gas chromatography

To verify the accuracy of ^1H NMR measurements, we also performed gas chromatography (GC) analysis for the sample $Bi_2O_3/FeCl_3$. The benefit of NMR is its ability to investigate not only methanol but any other liquid oxygenates created, providing a qualitative understanding of our catalytic system. The raw chromatogram and methanol calibration curve are shown in Fig. S7. The methanol GC peak area was 23,492:

$$(CH_3OH \text{ concentration}) = \frac{(\text{peak area}) - 383}{17{,}906} \rightarrow (CH_3OH \text{ concentration}) = \frac{(23{,}492) - 383}{17{,}906}$$

$$(CH_3OH \text{ concentration}) = 1.29 \text{ mM}$$

$$1.29 \frac{\text{mmol}}{\text{L}} \text{ x } 0.1 \text{ L x } \frac{1000}{1} \frac{\mu\text{mol}}{\text{mmol}} \text{ x } \frac{1}{0.1 \text{ g}} \text{ x } \frac{1}{4 \text{ h}} = 322 \frac{\mu\text{mol}}{\text{g h}}$$

According to the ^1H NMR, the sample $Bi_2O_3/FeCl_3$ produced c.a. 231 $\mu mol\ g^{-1}\ h^{-1}$, demonstrating that the methanol concentration determined by ^1H NMR and GC is comparable. The statistical variance of the experiments can explain the different numbers that still are in the confidence value, indicating the accuracy of our results for production rates.

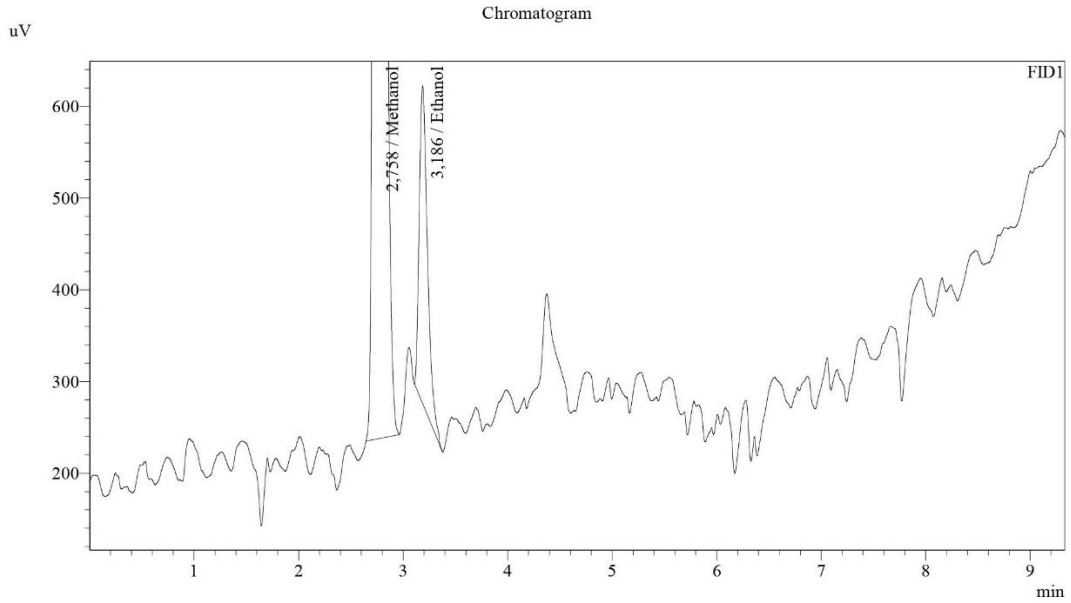

QuantitativeResult

FID1

ID#	Name	Ret. Time	Area	Height	Conc.	Unit
1	DME	--	--	--	--	%
2	Methanol	2,758	23492	4446	0,023	%
3	Ethanol	3,186	1900	346	0,001	%
4	Propanol	--	--	--	--	%
Total			25392	4792		

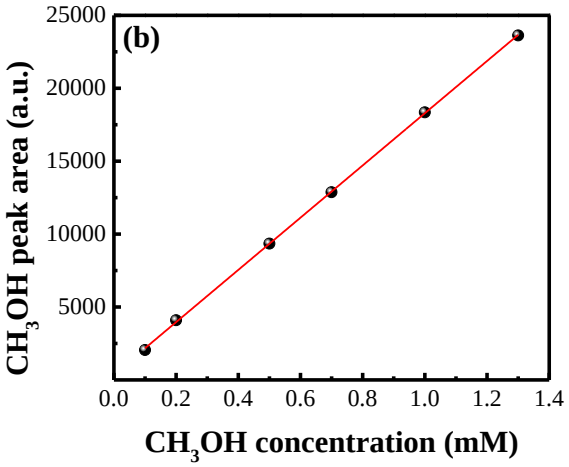

	A	B	C	D
1	**Equation**	**y = a + b*x**		
2	Weight	No Weighting		
3	Residual Sum of Squares	39949.84092		
4	Pearson's r	0.99994		
5	**Adj. R-Square**	**0.99985**		
6			**Value**	**Standard Error**
7	Área	**Intercept**	**382.69669**	**73.46394**
8		**Slope**	**17906.35611**	**96.46288**

FIGURE A4.7 - (a) Raw GC data of the liquid aliquot from the sample $Bi_2O_3/FeCl_3$; (b) methanol calibration curve; and (c) linear equation for the determination of CH_3OH concentration.

Reaction conditions: 1 g L^{-1} Bi_2O_3 in 100 mL of 1.0 mM $FeCl_3$ under visible-light. The reaction was carried out for 4 h using a mixture of CH_4 in argon (20%mol CH_4). $Bi_2O_3/FeCl_3$ produced c.a. 322 µmol g^{-1} h^{-1} CH_3OH by GC and 231 µmol g^{-1} h^{-1} CH_3OH by ^1H NMR.

*The values are similar and the small difference between them is related to the statistical variation of the experiments.

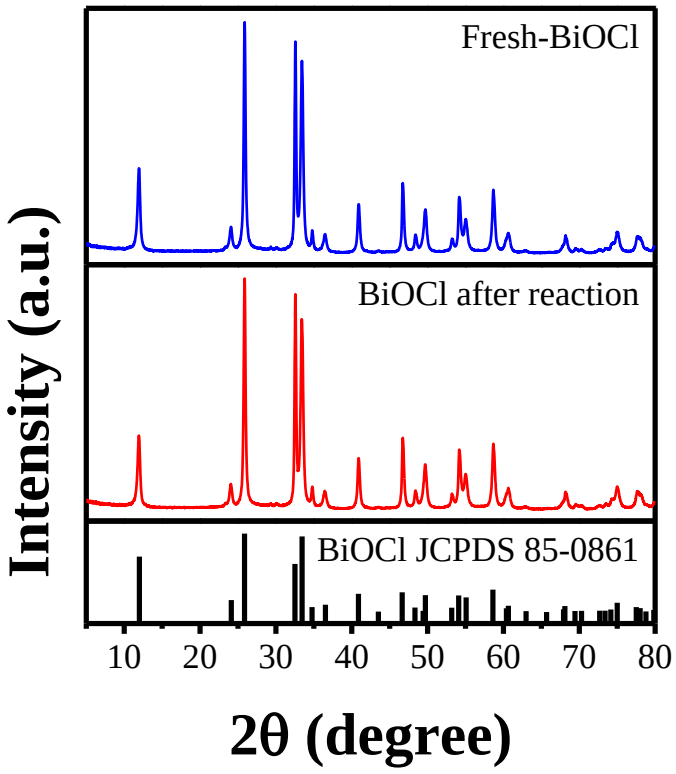

FIGURE A4.8 - XRD pattern of the as-synthesized BiOCl before and after the photocatalytic tests. *The XRD peaks are related to pure BiOCl according to the JCPDS #85-0861.

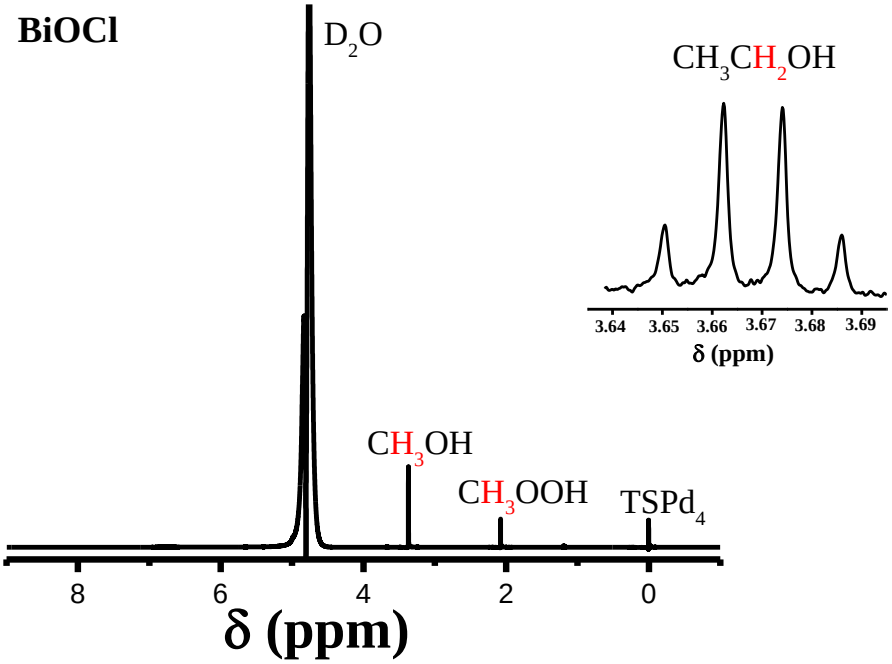

FIGURE A4.9 - ^{1}H NMR spectrum of the liquid aliquots collected from the partial photooxidation of CH_4 using BiOCl as photocatalyst. This analysis used 60 µL of D_2O solution containing 0.21 mM of the reference 3-(trimethylsilyl) propionic-2,2,3,3-d_4 acid sodium salt ($TSPd_4$).

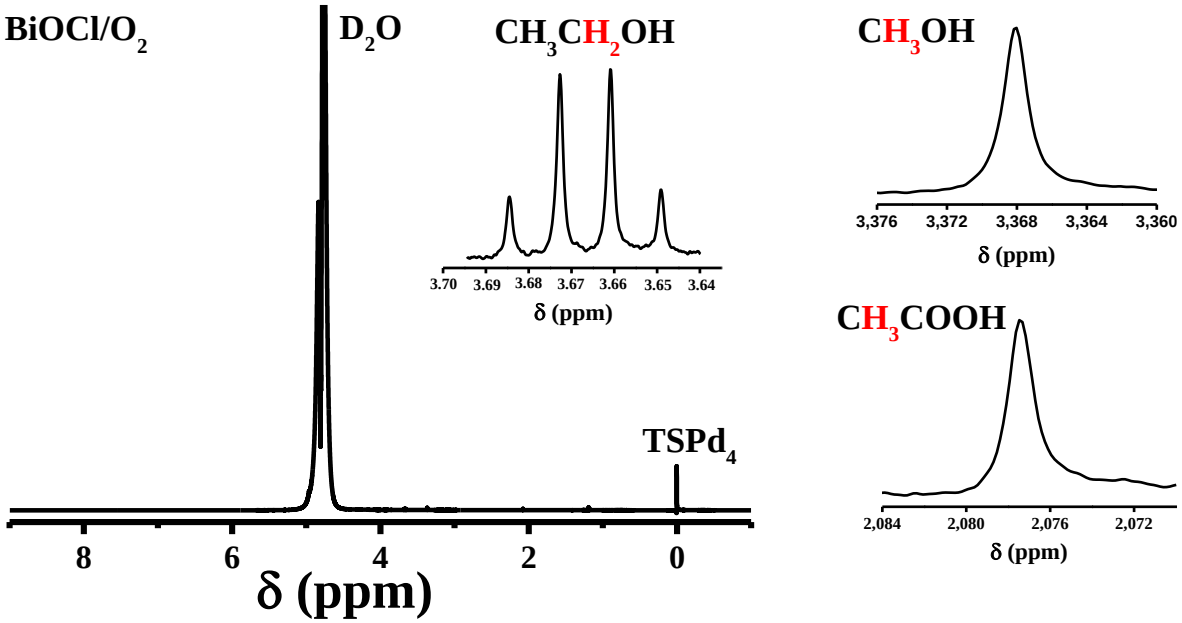

FIGURE A4.10 - ^{1}H NMR spectrum of the liquid aliquot collected from the partial photooxidation of CH_4 using BiOCl as photocatalyst in the presence of O_2. This analysis used 60 µL of D_2O solution containing 0.21 mM of the reference 3-(trimethylsilyl) propionic-2,2,3,3-d_4 acid sodium salt ($TSPd_4$).

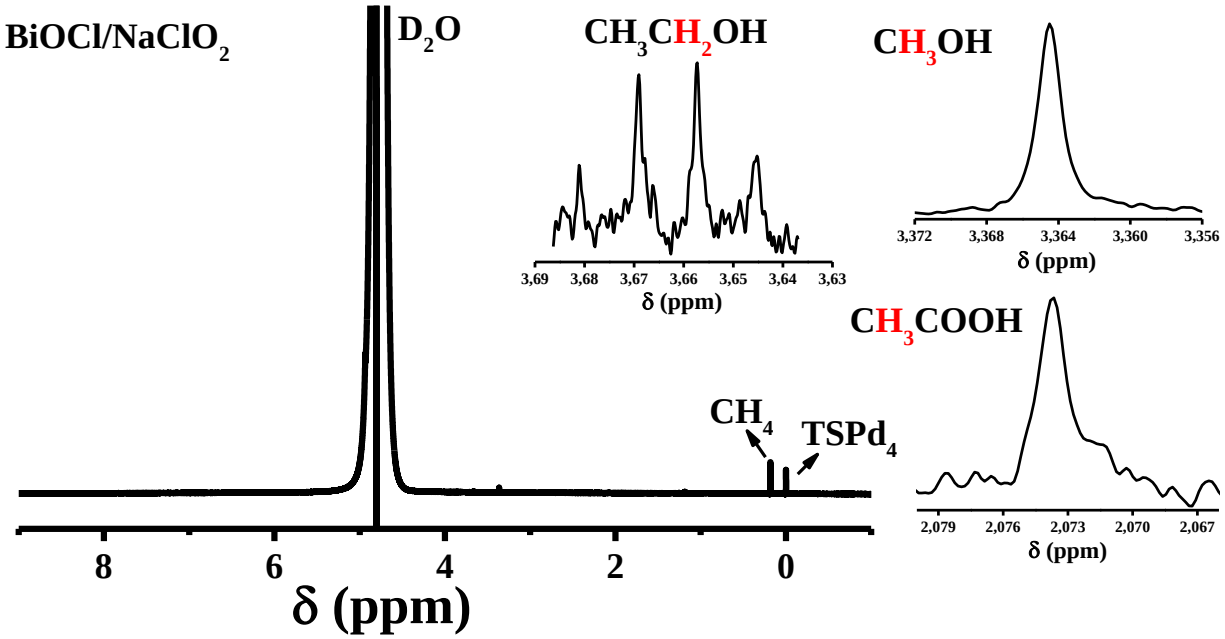

Figura A4.11 - ^{1}H NMR spectrum of the liquid aliquot collected from the partial photooxidation of CH_4 using BiOCl as photocatalyst in the presence of $NaClO_2$. This analysis used 60 µL of D_2O solution containing 0.21 mM of the reference 3-(trimethylsilyl) propionic-2,2,3,3-d_4 acid sodium salt ($TSPd_4$).

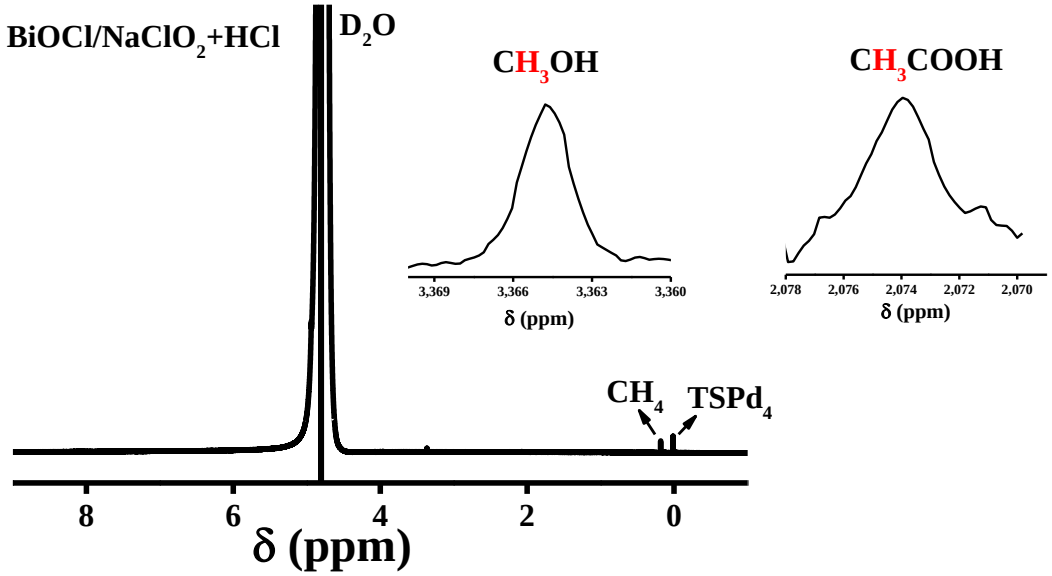

FIGURE A4.12 - ^{1}H NMR spectrum of the liquid aliquot collected from the partial photooxidation of CH_4 using BiOCl as photocatalyst in the presence of $NaClO_2$ and HCl. This analysis used 60 µL of D_2O solution containing 0.21 mM of the reference 3-(trimethylsilyl) propionic-2,2,3,3-d_4 acid sodium salt ($TSPd_4$).

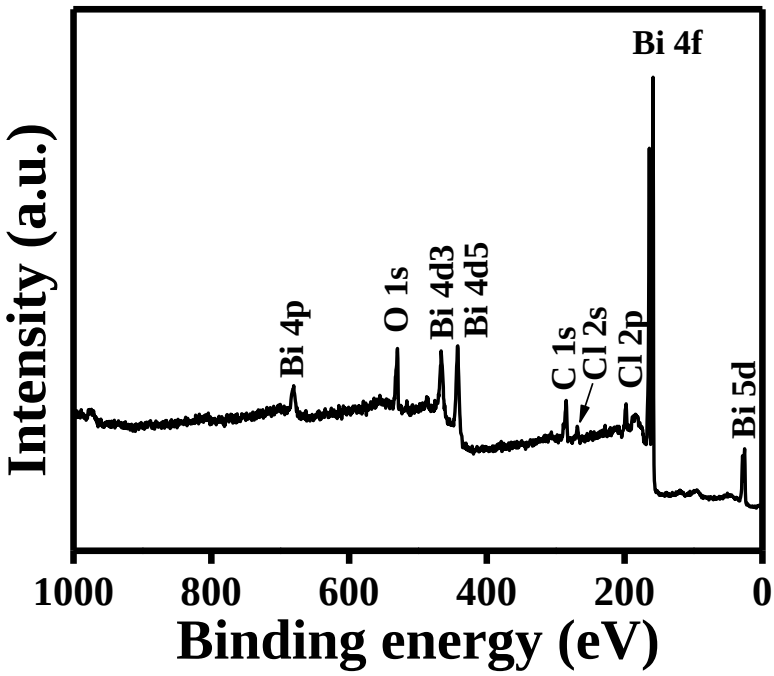

FIGURE A4.13 - (a) XPS survey spectrum and (b) high-resolution V 2p spectrum of the as-synthesized BiOCl.

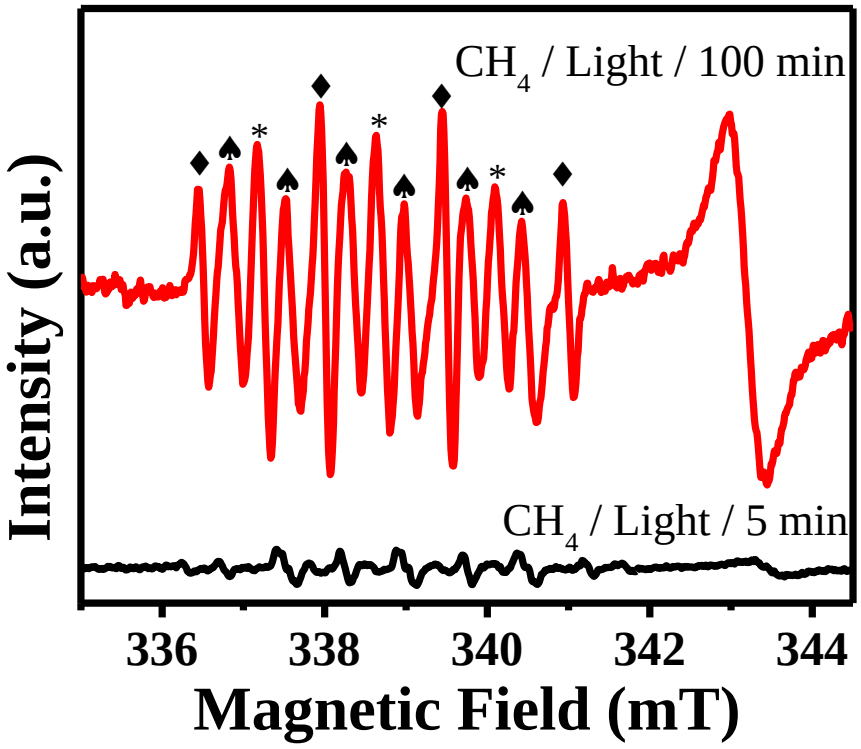

FIGURE A4.14 - ESR measurements of the DMPO solution containing pure BiOCl after 100 min of light irradiation in the presence of a mixture of CH_4 in argon (20%mol CH_4). (⁕) DMPO-$(OH)_2$, (♦) •OH, (♠) •OCl.